PHOTON FACTORY ACTIVITY REPORT

1983/84

NATIONAL LABORATORY FOR HIGH ENERGY PHYSICS, KEK

PHOTON FACTORY
ACTIVITY REPORT
1983/84

KEK Progress Report *84-3*

KEK Reports are available from

Technical Information Office
National Laboratory for High Energy Physics
Oho-machi, Tsukuba-gun
Ibaraki-Ken, 305
JAPAN

Phone: 0298-64-1171
Telex: 3652-534 (Domestic)
(0) 3652-534 (International)
Cable: KEKOHO

You can jump to the article by clicking its title.

Table of Contents

I. PREFACE

The Photon Factory ran steadily throughout the year 1984 providing abundant photons from ultraviolet through hard X-rays for users from universities, research laboratories and industries. They enjoyed stable operation of the light source for most of the beam-time and a lot of excitement was experienced both in scientific achievements and technical advances, thus making people more and more convinced that the capabilities of synchrotron radiation research are really remarkable.

Although the fiscal year (FY) 1984 is the second year of users' activity as it has been made open to the public since June 1983, the number of registered users already exceeded eight hundred as of June 1984, and the Program Advisory Committee (PAC) worked hard to admit about two hundred experimental proposals to be carried out by the end FY84. The progress achieved both in quality and quantity of the reports presented in this volume of Activity Report reflects the fact that the growing scientific activity was supported by the fantastic improvements in accelerator operation.

The total budget-limited time approved for operation during FY 1984 was 2200 hrs. The entire accelerator complex of the Photon Factory is currently operated in weekly mode, i.e., the storage ring used to work 96 hrs per week from Tuesday morning to Saturday morning without intermission, and two thirds is usually assigned to users' time.

Electrons are injected from the 2.5 GeV LINAC with a current of 50 mA by one pulse per second to the 2.5 GeV storage ring and its operation was nearly perfect throughout the year. It is providing electron beams regularly not only for the Photon Factory, but also to the 6 GeV Accumulator Ring of the TRISTAN Project. The LINAC staff is now busy in constructing a positron injector for TRISTAN.

The light source, the 2.5 GeV electron storage ring has also been running nicely through the year, except an accident which took place during the last week of operation for FY 1983, towards an end March 1984. Due to an operation failure happened in BL-1, the vacuum was broken along the entire ring and it took several weeks to recover. However, the recovering work was carried out mostly during the scheduled shut-down period, the net loss in the user's time was altogether two weeks.

The light source is normally operated with the maximum filling of 150 mA and the life time at 100 mA is typically 15 to 20 hrs. Thanks to a continued effort of machine studies the major sources of beam instabilities have been identified and consequently removed effectively. Accordingly the quality of the beam has been greatly improved during the last year both in temporal and spatial stability, which in turn resulted in significant improvements in users experiments.

Especially noteworthy in this connection is the commissioning of wiggler for general users which took place during the fall run 1984. A superconducting vertical wiggler inserted in a straight section along BL-14 was first operated successfully in February 1983, but it took some time to establish the mode of operation which is compatible with experiments at the rest of beam-lines. Now that the beam diagnosis both with and without the wiggler insertion as well as the path in between is nearly over, the wiggler beam time is regularly assigned in the former half of the weekly users' beam time at the field of 5 Tesla, the maximum value being currently limited not by the wiggler itself, but the RF power supply and the thermal load on the beam line. BL-14 is now equipped with stations for X-ray topography, protein crystallograph, X-ray precision optics, and/or occasionally experiments on angiography, etc., and its exciting capability is being demonstrated.

The undulator beam line (BL-2) has been divided into two, one of which is slightly deflecting the beam for keeping away from the inherent Γ-ray background generated from the long straight section of the ring. Experiments for neutrino mass determination, trace element analysis of light elements, X-ray microscope, atomic and molecular photoionization, etc., have been pursued at this beam line.

All these experiments demonstrated fantastic extension of the technical capability associated with these insertion devices.

As for the beam-line extention, we stayed on the same level as the previous year, namely, nine main beam lines with twenty five branch lines with experimental stations. However, now three new beam lines are under construction and will be completed by the end FY84. They are (1) Hitachi beam-line for lithography, EXAFS, and photochemical reactions (BL-8), (2) the surface science beam line prepared by Research Center for Spectro-chemistry, University of Tokyo (BL-7) and (3) the KEK/HITACHI beam line for development and evaluation of optical elements for synchrotron radiation research (BL-27).

We expect to be able to construct additional four beam lines within FY85, two of them being funded by the government (BL-6, BL-16) and the rest by the research laboratories of industrial companies, i.e., NEC (BL-9) and Fujitsu (BL-17). Reflecting the rapidly growing interest in the synchrotron radiation research in industries, further proposals to set up beam lines for industrial research are being discussed, and plans submitted by the following governmental research laboratories; Institute for Solid State Physics, University of Tokyo; institute of Plasma Physics, Nagoya University, to be joined by the Institute of Space and Astronautical Science, are also to be considered. The Photon Factory ring has twenty eight bending magnets and twenty four of them are ready for extracting radiation including the insertions. Now that sixteen beam lines will be occupied within FY85, a problem arises how to divide the remaining eight beam lines among the demanding users. The Advisory Council of the Photon Factory recently decided to have a sub-

committee for assessment of these concurrent proposals of new beam lines.

Utilization of the synchrotron radiation at the Photon Factory by the private industries has been encouraged since its initial stage of activity. Of course, the Photon Factory is the national research institution so that the authorized primary users are researchers from universities, and the proprietary research activities are admitted under a certain limitations. Nevertheless, their participation increased in a remarkable rate during the year 1984. Besides the joint effort by KEK and companies such as NTT, Hitachi, etc. to set up beam lines for limited usage described above, the proprietary uses of the radiation supplied by existing stations have been active. As of the end January 85, 36 applications have been accepted since April 84, the total time being 1125 hrs. Another type of collaboration between KEK and the private company is to organize a joint research project for a particular subject. Five such collaborations have been contracted between KEK as one partner and Hitachi, Toshiba, NEC, Fujitsu, and Hitachi/Mitsubishi Electric, as another, respectively.

Communication between users and PF is getting more and more important because of the increasing number of users, namely the increased participation of inexperienced users. Photon Factory News born in 1983 as soon as the public utilization of PF started, has been regularly published to fulfill these growing demands. The annual user's meeting of the Photon Factory, the 2nd Photon Factory Symposium held on 1-2 November, at Tsukuba University, also played a significant role in this respect.

International collaboration is also developing. Exchange of personnels with the active overseas research laboratories has been intensively organized, and we enjoyed collaborations with worldwide visitors, Prof. Chen from Changchun, Prof. B. Sonntag from Hamburg, Dr. J. West from Daresbury, and Dr. W. Gudat from Julich.

The last but not the least, Professor Kazutake Kohra, the founder and the first director of the Photon Factory, retired from his duty on the 1st April, 1984. The establishment and every success of the Photon Factory owes greatly to his outstanding leadership and enthusiasm and I would like to extend our sincere gratitude and congratulations to his endeavour and achievements on behalf of all the PF in-house staff and users.

Taizo Sasaki
Director

II. ORGANIZATION AND OPERATION

The organization and the staff members are shown in Table 2.1. The total number of the staff members has slightly increased but is not sufficient to support the whole system including accelerators and the experimental equipment accepting more then 800 visiting users.

The officially alloted time for operating accelerators has also increased year by year in such a way that it was 1900 hrs for FY 1983, 2200 hrs for FY 1984 and will be 2600 hrs for FY 1985. The time is still too short to meet the demands of users.

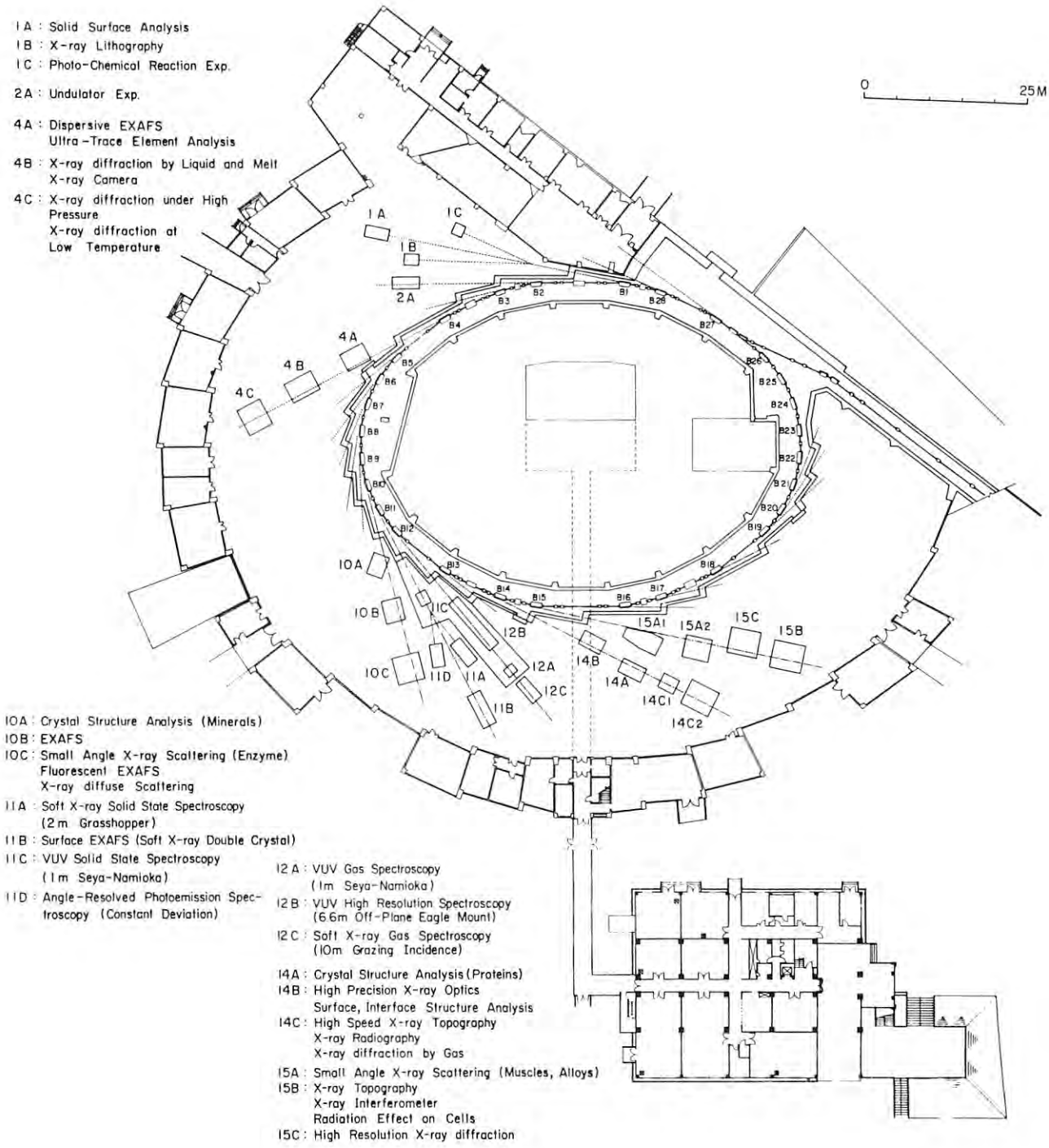

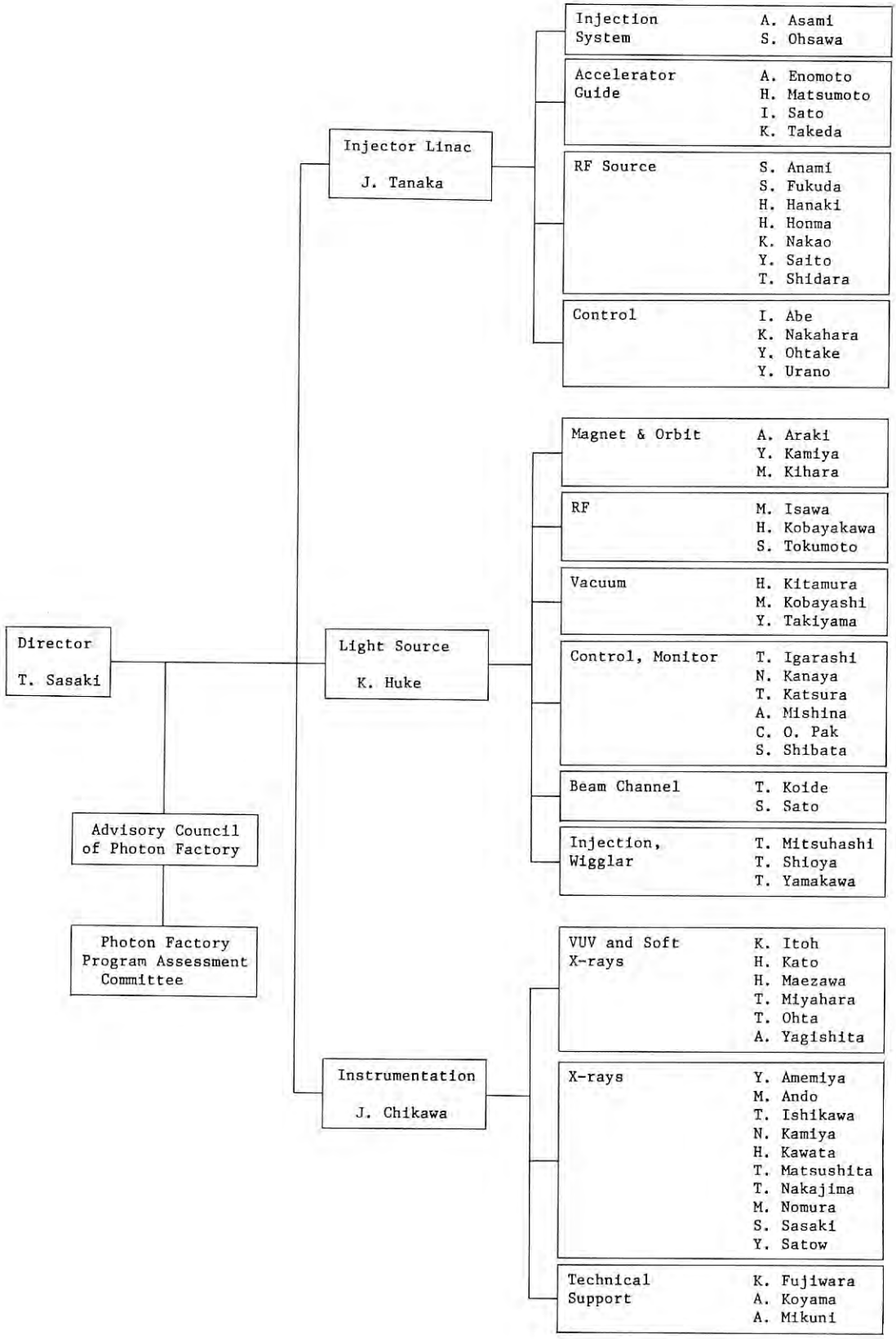
Director
T. Sasaki
Advisory Council of Photon Factory
Photon Factory Program Assessment Committee
Injector Linac
J. Tanaka
Injection System
A. Asami
S. Ohsawa
Accelerator Guide
A. Enomoto
H. Matsumoto
I. Sato
K. Takeda
RF Source
S. Anami
S. Fukuda
H. Hanaki
H. Honma
K. Nakao
Y. Saito
T. Shidara
Control
I. Abe
K. Nakahara
Y. Ohtake
Y. Urano
Light Source
K. Huke
Magnet & Orbit
A. Araki
Y. Kamiya
M. Kihara
RF
M. Isawa
H. Kobayakawa
S. Tokumoto
Vacuum
H. Kitamura
M. Kobayashi
Y. Takiyama
Control, Monitor
T. Igarashi
N. Kanaya
T. Katsura
A. Mishina
C. O. Pak
S. Shibata
Beam Channel
T. Koide
S. Sato
Injection, Wigglar
T. Mitsuhashi
T. Shioya
T. Yamakawa
Instrumentation
J. Chikawa
VUV and Soft X-rays
K. Itoh
H. Kato
H. Maezawa
T. Miyahara
T. Ohta
A. Yagishita
X-rays
Y. Amemiya
M. Ando
T. Ishikawa
N. Kamiya
H. Kawata
T. Matsushita
T. Nakajima
M. Nomura
S. Sasaki
Y. Satow
Technical Support
K. Fujiwara
A. Koyama
A. Mikuni

III. INJECTOR LINAC

1. INTRODUCTION

The PF injector linac has provided 2.5 GeV electron beams to the PF 2.5 GeV storage ring since February 1982 and to the TRISTAN accumulation ring since October 1983, respectively. Scheduled operation of the linac has been continued without any serious trouble and the operation time during FY 1983 was over 2,100 hours.

An electron linac is a powerful and flexible accelerator; especially in the PF 2.5 GeV electron storage ring, an electron linac is used as the full energy injector. This fact is of great advantage to the PF storage ring in comparison with other storage rings. Actually the injector linac made possible easy and prompt injection to the storage ring.

For the last two years, with the advancement of fine tuning of the injection system, beam transport system and of the rf system including 41 high power klystrons, beam quality of the linac and injection procedure to both of the rings have been remarkably improved. In addition, constant improvement in the control system and experience of the linac staff have made the routine operation of the machine more simple and more easy.

The PF ring has been operated in a multi-bunch mode (fill up all of the 312 ring rf backets). It means the beam pulse width to be injected is in a range of microsecond and the beam is not necessary to be synchronized with the ring rf (500 MHz).

On the other hand, in the TRISTAN accumulation ring, single bunch mode operation is usual. In this case, it is necessary for the injection beam to have a very short pulse width less than 2 ns corresponding to one period of the ring rf (500 MHz for the PF ring and 508 MHz for the AR) and to be synchronized with both of the ring rf and beam revolution frequency.

This nanosecond pulse beam is of course required for the single-bunch mode operation of the PF ring. Although the stored current of single bunch mode operation was limited to 30 mA because of overheat of vacuum chamber, test operation in the PF ring was successful.

Such a short pulse beam is available not only for the single bunch mode operation of the storage rings but also for picosecond range single bunch beam acceleration in the linac itself.

To provide long (μs) and/or short (ns) pulse beams efficiently for both rings, smooth and prompt switchover of beam pulse width, beam current and deflection of beam are necessary.

For this purpose, a new electron gun (two ways for microsecond and nanosecond pulse beams), a switchover system of the beam pulse width and synchronized trigger system were developed.

Usually, it takes only several minutes to finish injection into the PF ring and lifetime of stored beam in the ring is increased to more than 10 hours. However, injections for the PF ring are decided to be repeated at intervals of 8 hours, because the repetition rate corresponds to one injection per shift in the PF scheduled

operation. During the intervals of the injection into the PF ring, the linac beam is used for the AR. At present, the injection energy is fixed at 2.5 GeV and the beam currents are 30 to 50 mA for the long pulses and 100 to 120 mA for the short pulses, respectively.

Repetition rate of injection beam for the PF ring has been kept at 1 Hz; however, for the AR the rate is 10 Hz. At 1 Hz injection, beam stacking rate of the PF ring is 1 - 2 mA/pulse and this means the injection is finished in a few minutes. The rate is now limited by the tuning speed of the mechanical tuners of the ring rf cavities.

The linac beam is stable; however, long term stability of the beam is still limited by occasional arcing in the high power klystrons. The beam has been interrupted for a few minutes whenever fault of the klystrons took place. The fault owing mainly to internal arcing is being cured by improvement of the klystron cathode assembly and of the klystron production process.

2. OPERATION SUMMARY

2.1 Introduction

Scheduled operation of the linac has been satisfactorily continued on the whole, and its operation time from December 1983 to March 1984 amounted to 600 hours, and the total operation time in FY 1983 reached 2100 hours. Table 2.1 summarizes the linac operation time. From the middle of October 1983, the linac has been successfully used for the TRISTAN Accumulation Ring (AR) as well.

Requirements for the beam characteristics from the PF ring and AR are quite different as already mentioned in the previous section. Furthermore, with the advancement of beam characteristics studies in both rings new requirements were presented, e.g., a linac

Table 2.1 Summary of linac operation time

Period	Operation time
Dec. 6, 1983 - March 24, 1984	600 hours
March 25, 1984 - May 14	shut down
May 15 - July 28	880 hours
July 29 - Oct. 1	Shut down
Oct. 2 - Dec. 22	980 hours

trigger signal should be synchronized with the rf of the PF ring with a variable delay. To meet all these requirements further developments had to be made on the electron gun, trigger system, safety interlock system, etc. The computer control system has been steadily advanced. Continual efforts have been made to improve high power rf dummy loads, an rf phase detector and high power klystrons.

2.2 Operation and improvement

There occurred a doubt that one of the beam instabilities experienced in the PF ring might be caused by ions trapped in the electron beam. In order to clarify and hopefully to cure this problem, it was requested not to fill all the buckets along the circumference with electrons but to keep a part of them empty. This mode of the partially filled buckets could give ions a chance to escape from the beam. To realize this mode the linac trigger signal should be synchronized with the revolution frequency as well as with the rf frequency of the ring, and naturally the linac beam width must be much shorter than the revolution time (0.6 μs) of the beam in the ring. Furthermore, a variable delay was necessary to enable fine tailoring of the beam shape along the ring circumference.

The trigger system was improved to satisfy the above requirement, and it became possible to inject electrons so as to be stored in the ring with an arbitrary shape, and an instability due to ion-trapping was considerably suppressed.

In the middle of October 1983, test operation of the AR started. In early stage of operation, beam characteristics required are such that the pulse width is less than 20 ns and a peak current of about 100 mA. Therefore, a new electron gun was developed, which could produce a beam pulse with the 4 ns width and 200 mA peak current, and temporarily used for this stage. Fast switchover of beam pulse width between nanoseconds and microseconds is important; a system was developed to switch over not only the pulse width and trigger signal but also a safety interlock to enable selection of the PF or AR injection mode. In due course of time the electron gun was improved to produce a shorter pulse than 2 ns, and in December 1983, a single bunched beam was successfully obtained in the PF ring. The details of the short pulse beam and switchover system are described in section 3. From January 1984 the short pulse beam of a width less than 2 ns has been extensively used in the AR.

Development of the control system to ease the linac operation has been continuously made. One is on the klystron control which enables not only to display detailed status of every klystron and statistical data of all klystrons, but also to adjust the rf phase, to preset klystron high voltage and to switch on/off automatically all klystrons. Another one is on the transport system, which allows to inspect a detailed status of all transport elements.

Developments of high power rf dummy loads, an rf phase detector and high power klystrons have been intensely continued as described in later sections. Some dummy loads were installed in the linac and have been successfully operated for a high power test. The rf phase detector has been effectively in use for tuning of the linac. The high power klystrons have been steadily improved and the average fault rate decreased from the value of about 5.1 times/hour to 2.4 times/hour as described in section 5.

2.3 Troubles

There was a vacuum leak experienced in the evacuating system of the linac. This was caused by deterioration of a Viton O-ring gasket; after this trouble, it was replaced by a metal gasket. Recently pumping speed of the small ion pumps (50 ℓ/s) have been gradually slowing down, so that they should be replaced in the near future.

Troubles experienced with the rf system except the high power klystrons were a failure of the main-booster klystron and an instability of a sub-booster klystron. Other troubles were failures of some modules in the main modulators, and all these were replaced by new ones. A break down took place at a high power rf hybrid, which was caused by a use of an improper rf gasket; the electric contact at the flange was not sufficient.

A trouble was experienced with a trigger system of the short beam pulse. One of the circuits was put into misoperation due to noise.

3. SHORT PULSE BEAM ACCELERATION

3.1 Introduction

Since June 1982, the PF linac has been used to accelerate electron beams up to 2.5 GeV and to inject them into the PF storage ring. In October 1983, the construction of the TRISTAN accumulation ring (AR) was completed and its test operation started. Since then the linac has been operated as an injector of the AR as well. The beam characteristic required for the AR is considerably different from that for the PF: the beam pulse width for the PF is 0.5 - 1.0 μs, whereas that for AR is less than 2 ns. Furthermore, the peak current is 30 - 50 mA for the PF and 100 - 120 mA for the AR, the pulse repetition rate is 1 pps for the PF and 1 to 10 pps for the AR. The most significant difference is that of the pulse width. Meanwhile, a requirement has arisen that it is useful to have a single bunched beam also in the PF.

To meet these requirements a short pulse grid pulser and small jitter triggering system with an optical fiber have been developed. Another development also made is a fast switching system from a long/short to a short/long pulse operation mode. At present, the AR is used like a synchrotron and needs beams to be injected almost always. Although the lifetime of the beam in the PF storage ring is fairly long, the PF ring requires beam injection at least 2 - 3 times a day.

3.2 Electron Gun and Associated Circuits

Electron gun

Electron beam is injected from an electron gun into the linac; a cross section of the gun is shown in Fig. 3.1. Firstly, a high voltage pulse of 100 kV is applied to the gun and the

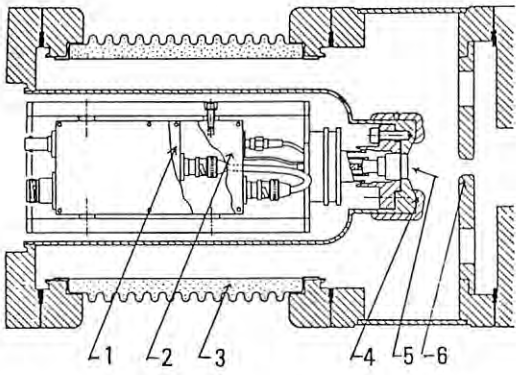

Fig. 3.1 Electron gun assembly. (1) O/E module, (2) grid pulser, (3) ceramic insulator, (4) focusing electrode, (5) cathode grid assembly and (6) anode.

grid-cathode assembly is driven to a negative high voltage, while the anode is kept at ground potential. No beams are yet drawn to the anode because the cathode is kept positive to the grid by a DC bias voltage. Secondly, applying a small negative pulse to the cathode, electrons are drawn from the cathode, and accelerated by the high potential previously applied between the anode and the grid. Thus the beam width is determined by a width of the pulse applied between the cathode and grid. A circuit to produce this pulse is usually called a grid pulser.

Grid pulser

A grid pulser was fabricated and tested to produce a short pulse beam with a width less than 2 ns. The circuit diagram is shown in Fig. 3.2; the stored charge in a 10 cm long coaxial cable is discharged by switching on three stage avalanche transistors. A fast negative signal thus produced is fed to the cathode; the pulse waveform is shown in Fig. 3.3 where the full width at half-maximum (FWHM) is 1.8 ns and the peak amplitude is 130 Volts.

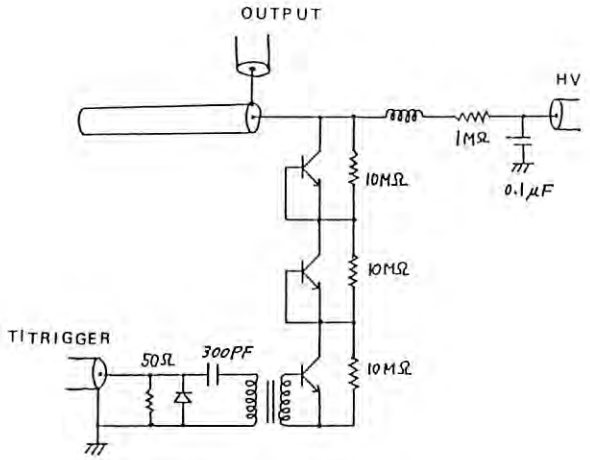

Fig. 3.2 Grid pulser.

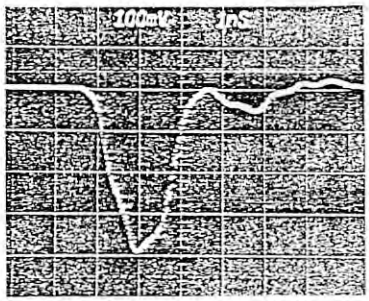

Fig. 3.3 Output voltage waveform of grid pulser.

Trigger circuits

To transmit a trigger signal from the ground potential to a high potential, an optical fiber is most suited, because there is no insulation and noise problems and it is easy to handle if special care is given to a problem of time jitter. The trigger signal transmission system fabricated consists of an electric-to-optical signal conversion circuit (E/O) with a laser diode, 20 m long optical fiber, and an optical-to-electric signal conversion circuit (O/E) with a PIN photodiode. Time jitter less than 30 ps is achieved with this system.

Switching system

Both grid pulsers for long and short beams are connected to the gun with their trigger circuits. A small inductor is inserted between the long pulser and the gun cathode, and works as a low-pass filter. The inductor has a high impedance for a short pulse but affects little a long pulse. The pulse width mode is determined by selecting one of the trigger circuits to be actuated. This selection is manually done by a push-button. The total time required for changing this operation mode is only a few minutes including the safety interlock system, the beam transport system and the energy adjustment.

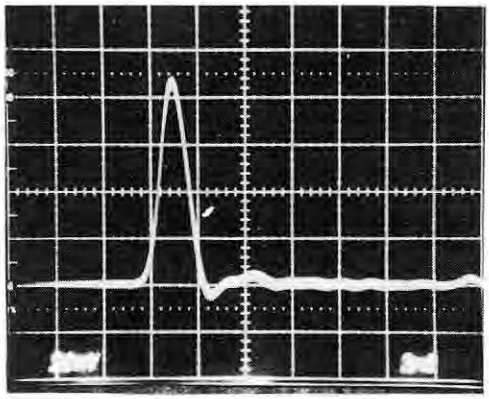

Fig. 3.4 Short pulse beam shape.

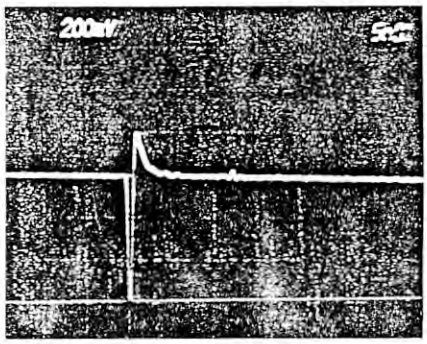

Fig. 3.5 Single bunch beam in the PF ring.

3.3 Performance

A short pulse beam is measured with beam monitors installed at the end of the injector and near the end of the accelerator. A typical example is shown in Fig. 3.4, which is measured near the end of the accelerator with an about 10 m long cable. The beam has a width less than 1.5 ns with an energy of nearly 2.5 GeV and a peak current of 110 mA. When the beam is injected into the AR or PF ring, a single bunched beam is successfully obtained. Figure 3.5 shows a single bunched beam first obtained in the PF ring in December 1983.

4. SHORT PULSE BEAM MONITOR

A nanosecond pulse beam monitor has been investigated since the last year. The positron beam handling requires a monitor which can respond to a beam with the width of 1 ns and a current less than 10 mA.

Characteristics of a simple wall current monitor and a fluorescent screen were studied at first. Figure 4.1 shows the illustration of the wall current monitor and the instruments to test it. These were located at the end of the 35 MeV injection system of the PF 2.5 GeV electron linac. To observe "wall current", ten pieces of 510 Ω resistors were distributed across a ceramic insulating beam pipe which has been used for a long pulse current transformer. Beam signals from the monitor were transmitted to the klystron gallery through an 11 m long RG-58 c/u coaxial cable and observed with an oscilloscope.

A signal picked up from the resistor is shown in Fig. 4.2 in contrast with a pulse voltage applied to the gun grid. Figure 4.3 shows a signal voltage against the beam current measured by a beam catcher. Visible light emitted from a flourescent screen (chromium-activated alumina ceramic) was able to be observed by a standard TV system for the beam intensity as low as 5 mA in the case of 10 pps beam acceleration.

The wall current monitor mentioned above gives a relatively large signal and good response, but the signal is easily affected by the electromagnetic noise because it has no shielding case. Figure 4.4 shows an improved one which has recently been made up. This

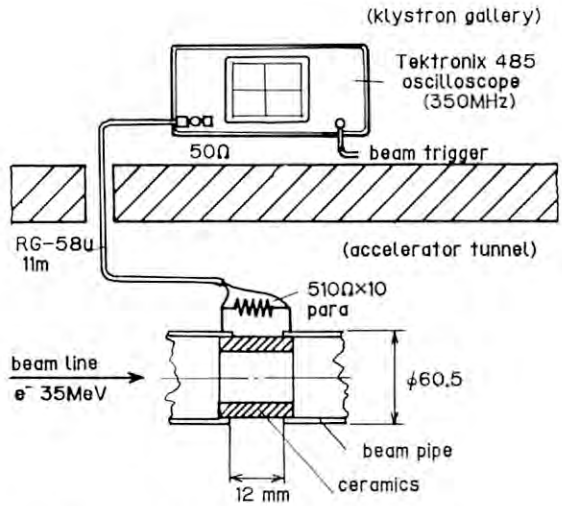

Fig. 4.1 Illustration of the wall current monitor and the instruments to test it using a linac beam.

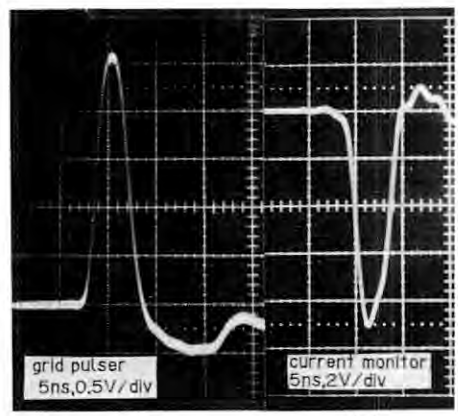

(a) (b)

Fig. 4.2 (a) Signal picked up from the simple wall current monitor shown in Fig. 4.1.
(b) Waveform of the gun high voltage.

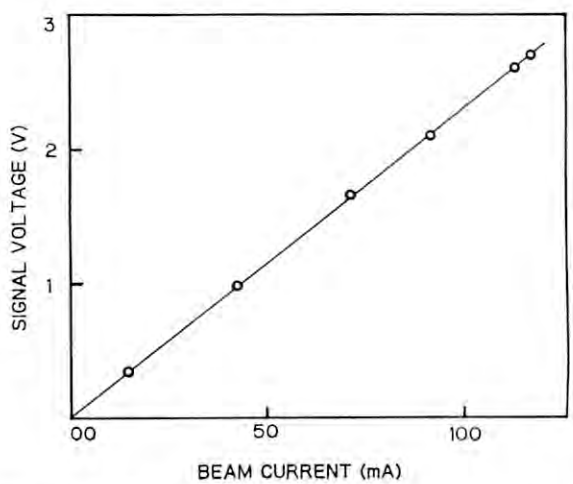

Fig. 4.3 Signal voltage from the simple wall current monitor shown in Fig. 4.1 against the beam current.

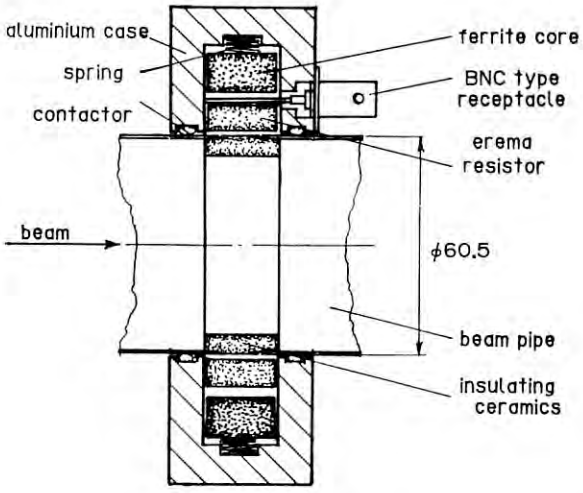

Fig. 4.4 Sketch of the improved current monitor for short pulse.

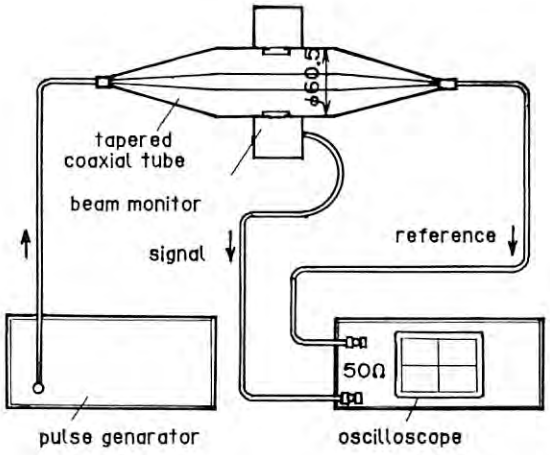

Fig. 4.5 Illustration of the bench-test for the short pulse current monitor using an impedance matched tapered coaxial line.

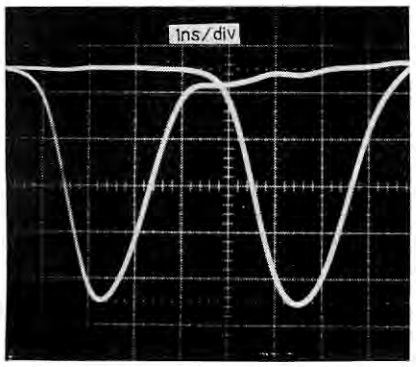

Fig. 4.6 Comparison between the pulse shapes of the pulse generator output (a) and the signal from the improved current monitor (b).

monitor consists of the following components:

(1) A ceramic solid resistor in the shape of a disk.
(2) Toroidal manganese-zinc ferrite core.
(3) Aluminum case with a BNC type receptacle.
(4) Ceramic insulating beam pipe with flanges.

The components #1 ∿ 3 can be separable into two pieces and easily set round the insulating pipe.

This monitor acts also as a one-turn ferrite core current transformer, because the aluminum case and resistor form a one-turn winding on the ferrite core. A voltage drop across the resistor is picked up with a short wire connected to a BNC type receptacle.

Characteristics of the monitor has been studied using a nanosecond pulse generator and a tapered coaxial line as shown in Fig. 4.5. Figure 4.6 shows a comparison between the pulse shapes of the pulse generator output and signal from the monitor. Figure 4.6 represents a response of the monitor. Relation between a beam current and the output voltage can also be obtained from this test.

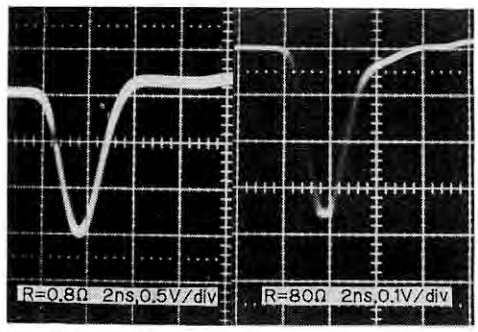

(a) (b)

Fig. 4.7 Signals from the improved current monitor due to a real electron beam, which were observed in the same way as shown in Fig. 4.1. (a) 0.8 Ω register, (b) 80 Ω register.

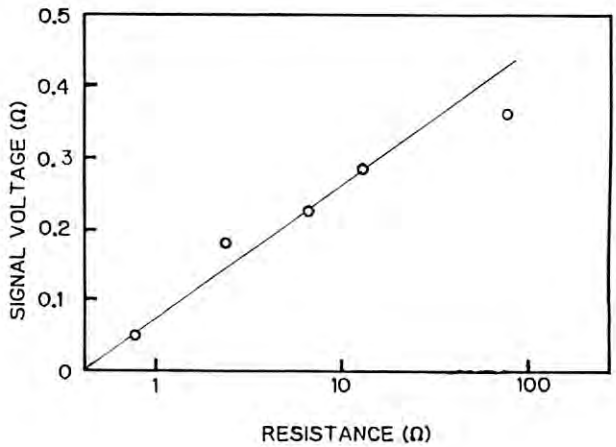

Fig. 4.8 Signal voltage from the improved current monitor against the register.

Signals due to a real electron beam are shown in Fig. 4.7. Dependence on the signal sensing resistance has been examined at a beam current of 100 mA with resistances of 0.8, 2.4, 7, 13 and 80 Ω. Figure 4.7(a) is the case of 0.8 Ω resistor and 4.7(b), 80 Ω resistor. As the resistance increases, the signal voltage also increases as shown in Fig. 4.8; however, rise time of the signal pulse becomes worse.

These current monitors have sufficient response for nanosecond beam; signals can be observed at a beam current as low as 1 mA by a simple wall current monitor. For the beam less than 1 mA the signal to noise ratio should be improved by reducing noise itself and by amplifying the signal.

5. HIGH POWER KLYSTRON STATUS

The performance of the microwave source is the most important to achieve the stable operation of the electron linac. Especially the high power klystrons are the key points to characterize the reliability of the microwave source.

In this report the operational status, several troubles, failures and improvements about the high power klystron are described in detail.

5.1 The characteristics of the klystron

Table 1 shows the specification of a klystron and a typical operating condition.

Table 5.1 Specification and operation condition

	specification	operation
Max. beam voltage	270 kV	
Max. beam current	295 A	
Pervience	2.1±0.1 $A/V^{-3/2}$	
Average beam power	30 kW	
Beam pulse width	< 4 μs	3.5 μs
RF pulse width	< 4 μs	3.5 μs
Pulse repetition rate	100 pps	10 pps
RF frequency	2,856 MHz	2,850 MHz
Peak output power	30 MW	20-30 MW
Efficiency	40 %	35-40 %
Gain	51 dB	45-52 dB
Focusing magnet	electromagnet	permanent

The manufacturer prefers to use an electromagnet for focusing electron beam in the klystron and has been testing with it. On the other hand, in the PF linac a permanent magnet was adopted, because it had the advantages of easy maintenance and minimum operating cost. On the contrary, that had large disadvantage of uneasiness of changing the magnetic field. It was found that complete matching between tubes and magnetic field produced by the permanent magnet was fairly difficult. Also the asymmetry of the transverse magnetic field of the permanent magnet has a large effect on the performance of klystrons. Almost all magnets must be adjusted in order to remove the radial asymmetry by means of the magnetic shunt (iron plate). Some of the magnets have field-shaping solenoides under the bottom yoke to vary the magnetic field across the cathode plane. Intensive study of the magnetic field has been continued; nevertheless some problem still remains because of frequent interruption due to other troubles. The magnets have not been adjusted completely; therefore output power on test in the PF linac is lower than that of specifications and the manufacturer's test results.

5.2 Klystron operating performance

Operation hour

Table 5.2(a) shows the tube performance data during the past 3 years up to July 1984. Recently the average operating time in each fiscal year reached about 2,500 hours. The 63 high-power tubes have been used since 1982. There were 20 failures during these periods giving MTBF (Mean Time Between Failures) of 13,200 hours. The mean age at failure was 2,300 hours, while the mean age of living tube was 4,960 hours. Table 5.2(b) shows the rearrangement of the mean age and MTBF corresponding to the year of production. Obviously, the MTBF increases gradually year by year because of the improvements as described below. Various age distribution histograms for the high power klystrons are shown in Fig. 5.1.

Table 5.2

(a) Cumulative usage hours of the past three years

Period	Total sockets	Failured No.	Failured Mean age	Living No.	Living Mean age	MTBF
1982/4-1983/3	53	11	1,306	42	2,933	12,505
1983/4-1984/3	63	20	2,285	43	4,169	11,247
1984/4-1984/7	63	20	2,285	43	5,075	13,195

(b) Comparison with historical lots usage

Tube	Total sockets	Failured sockets	Mean age(hours) Failured	Living	MTBF (hours)
1979	4	2	45	6,441	6,486
1980	20	9	2,282	6,313	9,998
1981	20	7	3,128	6,244	14,724
1982	9	2	1,586	4,102	15,944
1983	10	0	0	2,600	0

Fault rate

An important factor on the linac operation is the klystron fault rate. Too many faults lead to interruption of beam injection to the PF ring or TRISTAN Accumulation Ring (AR). For example, stable operation at a fault rate less than 1 fault/hour corresponds to no fault for 41 hours per one klystron.

Typical faults are due to overcurrent of an integeral ion pump (vacuum fault) and/or that of the high voltage pulse. The cause of these faults is the arcing in the tube. Sometimes beam voltage applied to the klystron must be lowered to reduce the fault rate. Also several klystrons became unstable because of the diode oscillation or other instabilities. Continuous

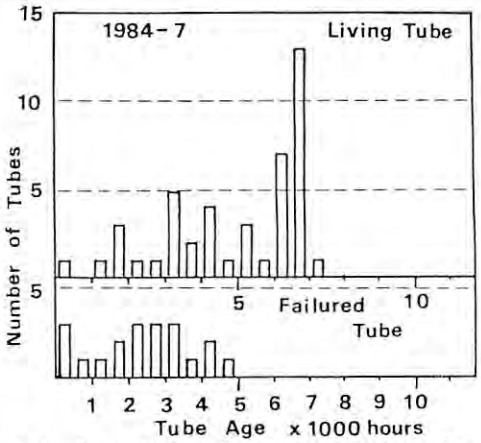

Fig. 5.1 Recent performance about the fault rate, beam voltage and average output power. "Ex. kly" denotes replacement of the klystrons for the corresponding period.

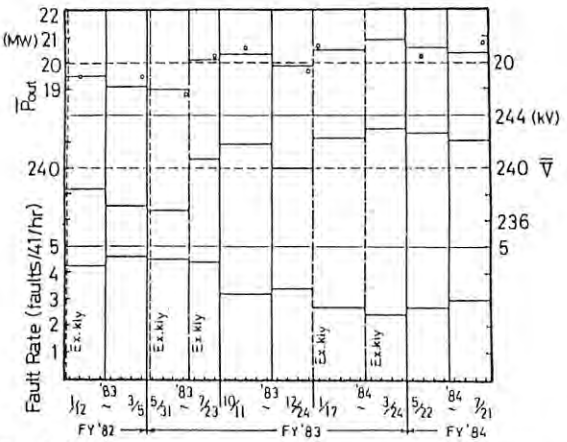

Fig. 5.2 Age distribution of the failured and living tubes.

improvements are making it possible to decrease the fault rate year by year. Average fault rate at the beginning of 1983 was 4.8 faults/hour, and recently this rate was decreased to 2.6 faults/hour (i.e., 1 fault/23 min). Figure 5.2 shows the recent performance about the fault rate, beam voltage and average output power for each operation period.

Tube failures and improvements

In this section the causes of the failures and improvements are described. The main causes of the failures are as follows.

(a) Puncture of high voltage seal ceramic,
(b) Filament short or open,
(c) Mechanical failure,
(d) R.F. Window failure,
(e) Internal arcing.

At the first operation, the failure (a) was dominant; this was possibly caused by the dielectric breakdown or puncture of the ceramic which was originated charging up of the ceramic surface by the electrons emitted from the brazing joint between ceramic and metal. A typical phenomenon was flashing glow in the tube and resulted in ceramic surface coloring. Initially this was avoided with a corona shielding cylinder around the brazing part and recently the cylinder shape was changed into conical one.

The failures (d) and (e) are serious, and these problems are essentially not yet solved. Generally the causes of window puncture seem to be dielectric breakdown and thermal breakdown. In KEK, former is dominant because of low duty operation. Processing procedure takes the important role to prevent the window breakdown. It was found that the ceramic itself had a rather large outgassing rate at the small output power (less than 1 MW), and glow discharge was always observed. Careful operation and processing at the start-up are done currently and seem to be effective. An air exposure on the ceramic surface is harmful so that nitrogen gas is filled inside as far as possible when tubes are stored. To solve these problems about (d) and (e) window study and coating work are in progress.

Arcing is the most serious problem for the high power klystrons. A common phenomenon is that the applied beam voltage between the anode and cathode must be gradually decreased because of the large fault rate. One of the reason of these faults seemed to be due to the collector trouble. This is the collector melting occurred by the imperfect beam dispersion at the collector because of the strong reverse fringing magnetic field of the permanent magnet. In fact small melting copper balls were found in some of the opened klystrons. This problem was cured by means of adding the magnetic shield to the collector. However internal arcing problem still remains.

Basically internal arcing has strong relation to the gun structure itself and material used. Also it depends on the way of processing of the gun assembly, i.e., cleaning or outgassing process. This kind of troubles has been pointed out frequently and the intense study for the development of a more stable electron gun has been done in the SLAC. The PF linac has tried to collaborate about the improvement of the klystron with MELCO; the current items related are as follows.

(a) Improvement of the oxide cathode: Oxide cathode needs essentially so called the "conversion process", and this process has the excessive outgassing rate. This possibly leads to the large contamination in the tube. A black thick film of the cathode material was found on the anode nose. It is not clear that this is related to the internal arcing. The manufacturer has tried to improve the oxide cathode itself by means of production process control and careful selection of nickel powder and carbonate materials. Another possible trial was to use the different type of cathode such as the dispensor cathode. This is also going to start.

(b) Design improvement of the gun: Arcing has also close relation to the gun structure, because high voltage is applied to narrow space between the anode and cathode. One trial was change in the shape of a focus electrode, and

another was development of the low gradient gun. These improved klystrons are now waiting for test in the PF linac.

(c) Materials used in the gun: Materials used for the gun assembly seem to be also important, and it should be considered what materials are most useful. Recently it is pointed out at the SLAC that carbon contamination is harmful to the gun. In the tube of the PF linac stainless steel is used for the focus electrode, and currently more low carbon material (e.g., SUS-316L) is brought into use.

(d) Improvement of the processing: Since all parts of the gun assembly are used in the circumstances like high temperature (about 850°C) and high voltage (about 270 kV), it is difficult to obtain the high vacuum (about 10^{-8}, Torr); therefore the careful cleaning process is important to make a more reliable gun. Currently, vacuum firing and induction heating of the assembly are performed sufficiently for the outgassing with oil-free pumps.

These programs are performed at the manufacturer's facility under the collaboration of the PF linac group. Since remarkable arcing phenomena have been able to be observed after a long operation run, it is difficult to evaluate immediately the result of the improvement; It takes more operation time to obtain the conclusive evaluation.

6. DEVELOPMENT OF RF DUMMY LOAD

At the end of every accelerator guide, an rf dummy load is installed in order to absorb the remaining rf power traversed through the accelerator guide.

The dummy load is a ceramic type SiC mounted in a short rectangular waveguide. The ceramic type SiC has excellent characteristics in both the rf power absorption capability and heat conductivity. The SiC dummy loads used so far were not necessarily satisfactory for high duty cycle operation. Improvement of the dummy load, therefore, has been promoted in the shape and cooling.

The dummy load structure was remodeled so as to cool the ceramic block directly by pure water; instead of a plate shape in the old model, the improved dummy load has such a shape as a cylindrical pipe with a conical head and is housed in a rectangular wave guide as shown in Fig. 6.1. Four sets of dummy loads were replaced by the new ones in the acceleration unit No. 6 of sector 5, and have been tested. Up to the present time, no trouble has occurred.

7. THE PHASING SYSTEM

In the electron linac of the traveling wave type, centers of accelerated beam bunches must be on the crests of the rf accelerating wave. If the correct condition dose not hold, the accelerated beam energy decreases and also the energy spread becomes wide. The phasing system makes it possible to satisfy this condition for all of the accelerator guides.

7.1 Methods of the rf phasing

General methods of the rf phasing are as follows:

(1) Beam energy maximization,
(2) Beam loading maximization,
(3) Direct phase comparison ("beam induction method").

"Beam energy maximization" is a method to adjust the phases of klystrons by using a beam energy analyzer placed at the end of the linac so that the accelerated beam energy is to be maximum. However, increase in the number of klystrons used decreases the ratio of energy variation by the phase rotation of one klystron. Furthermore the fine tuning becomes difficult around the optimum state, because the sensitivity (the ratio of energy variation to change in phase $\equiv \Delta E/\Delta\phi$) reaches zero. In the PF linac operation with 41 klystrons, tuning for reduction of phase error within ±5% requires an energy analyzer with resolution better than 10^{-4}; this method is not suitable for a long linac.

"Beam loading maximization" is a method of adjusting rf phase of klystrons so as to maximize the reduction rate of rf power level due to beam loading in accelerator guides. In an accelerator guide, an acceleration field is the vector resultant of the field from a klystron and the beam induced field as illustrated in Fig. 7.1. When these two field vectors are just in the opposite direction, the resultant field strength becomes minimum and the beam acceleration gain becomes maximum. This method is a very simple way and can be made without any special equipment; therefore this method is adopted widely. On the other hand in the case of the low beam current, an effect of the beam loading is small and the phasing becomes inaccurate.

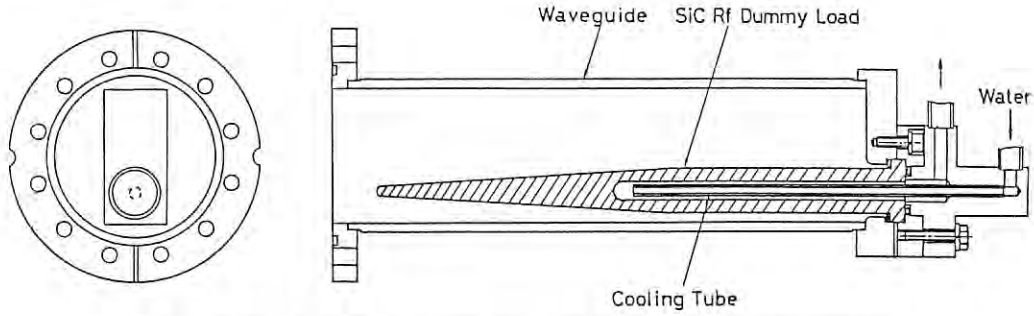

Fig. 6.1 Improved rf dummy load using a ceramic type SiC.

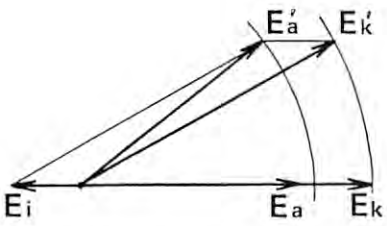

Fig. 7.1 Vector diagram illustrating the effect of beam loading. Ei represents the beam induced field, Ek the field from a klystron, Ea the acceleration field, and the primed for the case of incorrect phasing.

"Beam induction method" is a way to obtain the correct phase relationship between the beam bunch centers and the crests of the rf acceleration wave by means of phase comparison between the beam-induced wave and the wave from klystron. However these two waves are mixed in the accelerator guide and cannot be divided into each other. In order to compare these waves, it is necessary to separate them by shifting the pulse timing of klystron. To get a correlation between these phases, another cw signal (coherent reference signal) is required. A delayed position of the klystron pulse timing is referred to as the "standby" position. At that position its corresponding acceleration unit does not accelerate the beam; consequently the beam energy decreases. This is the only disadvantage of the beam-induction method. However this method has a number of advantages. The most exceeding one is its high sensitivity. This method is most appropriate for the fine tuning and is adopted at most long linacs.

7.2 Beam induction technique and automatic control

The rf system of the PF linac is shown in Fig. 7.2. The cw phase reference signal is transmitted from a multiplier installed in each sub-booster. The sub-booster klystrons are in double pulsed operation. The first pulse is used for the beam acceleration and the second pulse for the standby.

In this rf system, the principal procedure of the phasing with the beam induction method is as follows:

(1) The klystron to be phased is selected to the standby mode. Then, the rf monitor signal from the accelerator guide gives the waveform illustrated in Fig. 7.3.

(2) The first pulse signal phase is compared with the cw reference and is adjusted to the phase difference of +90° (or -90°) with changing the reference phase shifter.

(3) Next, the second signal is compared with this reference signal and is adjusted to the difference of -90° (or +90°) by the phase shifter of the klystron (IφA unit). Thus the phase difference between two signals results in 180°.

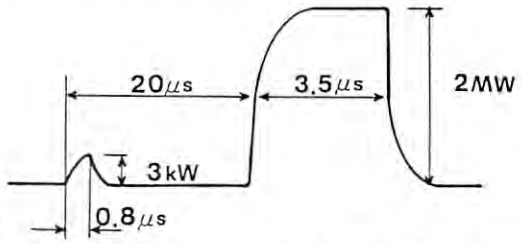

Fig. 7.3 Rf signal at the end of the accelerator guide in the standby mode.

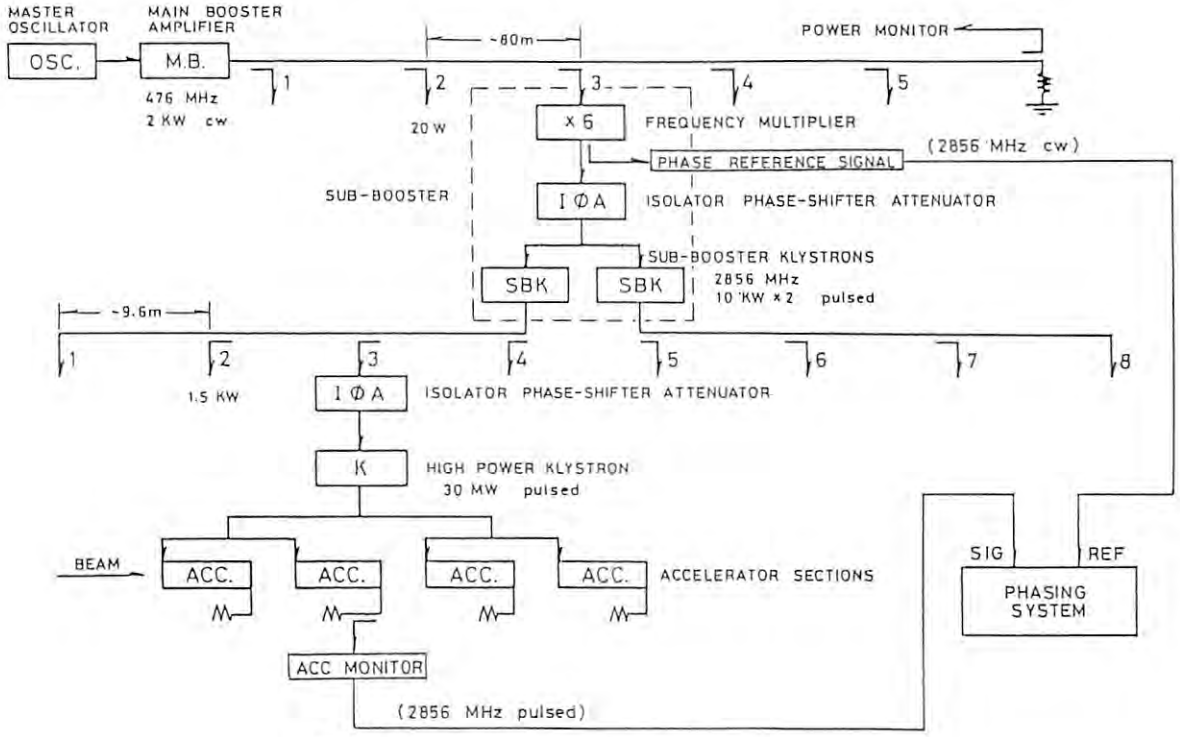

Fig. 7.2 Block diagram of the rf system.

(4) The mode switch is turned to the acceleration mode, and it is confirmed for the beam induced and klystron rf waves to be in a correct phase relation by observing the beam loading reduction.

These procedures are repeated for the 41 klystrons. Actually to perform these procedures, a large number of equipments and the complicated control system are required. Especially the most serious problem was development of the efficient phase detector covering the wide dynamic range. The difference between the amplitudes of the two signals is roughly 30 dB at the normal operation current. The phase detector normally used for the phase comparison is composed of diodes and a hybrid device, such as the slotted line hybrid or rat race bridge. For this large amplitude difference a special detector, which has a high precise hybrid and well balanced diodes, was developed, because phase detection error of within ±3° was very difficult.

Also an automatic control system is indispensable to achieve the phasing in a short time operation, because the number of equipments and their sorts to be controlled are too many, and their operations are complicated. Figure 7.4 is a schematic diagram of the phasing control system. All of the units in this system are already fabricated and being now worked in manual operation. Figure 7.5 is a block diagram of the controller for automatic control. The development of its software is now under way and scheduled to be completed within a short period.

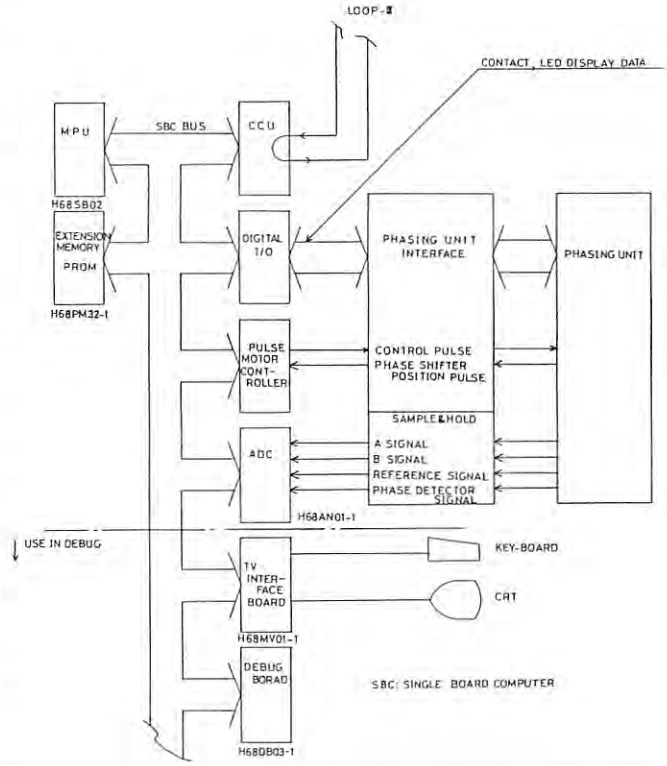

Fig. 7.5 Arrangement of the automatic phasing controller.

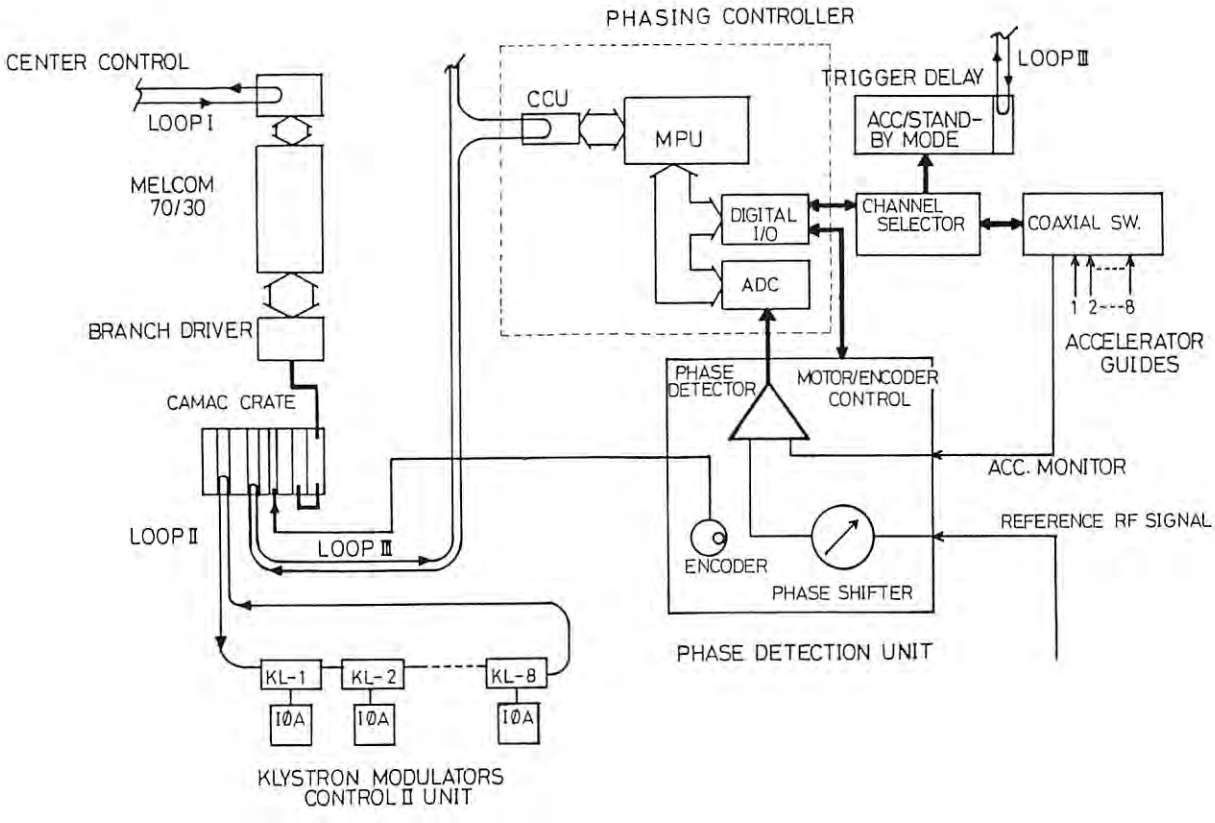

Fig. 7.4 Schematic diagram of the phasing control system for every sector.

8. LINAC CONTROL SYSTEM

8.1 Communication line and LSI trouble

Since fiber optic cables were laid down in the linac building in the early spring of 1981, they have been broken twice by careless work around optical transceivers. In those cases the break points were near the optical connectors where the protective outer sheath was removed from the fiber cables and individual fiber codes 3mm in diameter were naked. A He-Ne gas laser was used to find the break points where the intense light was leaking out through plastic coating and was able to be detected visually.

In general, digital integrated circuits (IC) are very reliable, but some IC failures were experienced at an early stage of test operation. One of them is a Serial Data Link Controller LSI (WD1933, Western Digital) which is used in the LOOP-II communication control circuits for the gun and klystron modulators. Three chips broke down during the test operation; at that time 60 chips were being operated. Moreover, this type of LSI has another trouble. It is specified to be operable in a loop mode with a GO-AHEAD sequence; however it fails to achieve a GO-AHEAD operation owing to an LSI bug. In the present LOOP-II communication circuit, a loop mode operation is realized by a conventional polling method: Every secondary station is polled one by one from the primary station, and a secondary station polled starts to send a message to the primary station after recognizing the line idle state.

8.2 Multiple controller CAMAC system

The Photon Factory injector linac is controlled by a distributed processor network in which an operator's console control station and six subcontrol stations are constructed on the basis of a single-minicomputer-controlled CAMAC system. In this system all messages interchanged between the main operator's console and the terminal equipments (klystron modulators, etc.) are transmitted through minicomputers for the operator's console and subcontrol station. The traffic on the communication line between the minicomputers sometimes becomes very heavy to intercept message transmission, particularly when an analog value is set to a phase shifter or a beam transport magnet power supply controller by manual rotation of a rotary encoder at the operator's console. In order to avoid this difficulty, a new auxiliary transmission line is required to transmit messages issued by rotary encoder operation not through the minicomputers.

From the beginning of the PF linac construction, it has been intended that the auxiliary communication line interconnecting subcontrol stations is to be built with a CAMAC system in the multiple controller configuration as defined in the CAMAC specification EUR 6500e - 1978. Figure 8.1 shows the transmission line configuration where a multiple controller configuration is adopted to reduce heavy load of minicomputers. The single controller and multiple controller configurations are simply illustrated in Fig. 8.2. In the multiple controller configuration, a single board computer with a 6800 type microproccssor and an auxiliary controller specified in EUR 6500e - 1978 are added to the single controller CAMAC system. In the single controller system, all modules contained in a crate are controlled through a crate controller type A2 by a minicomputer MELCOM 70/30, while in the multiple controller case, the CAMAC control load is shared by multiple computers.

A prototype auxiliary controller was made up and tested at the end of FY 1982. On the basis of this prototype, the second version auxiliary controllers were fabricated in FY 1983. They are to be installed in the subcontrol stations in conjunction with single board computers. The circuit block diagram is shown in Fig. 8.3.

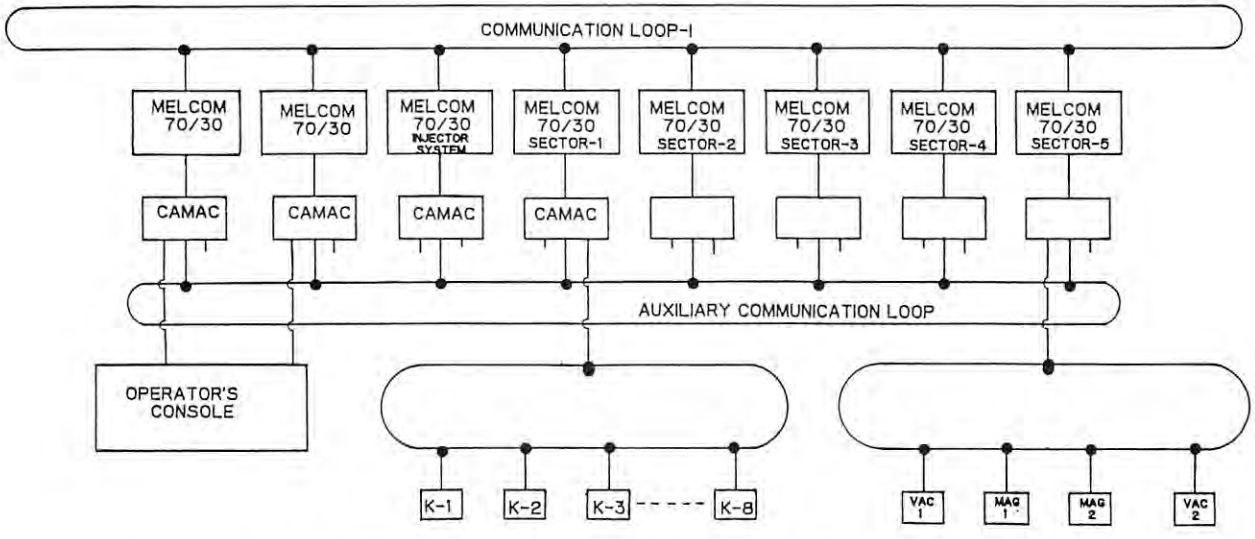

Fig. 8.1 Auxiliary communication loop configuration. This new loop is to be used to transmit messages for analog value setting to phase shifters and beam transport system controllers.

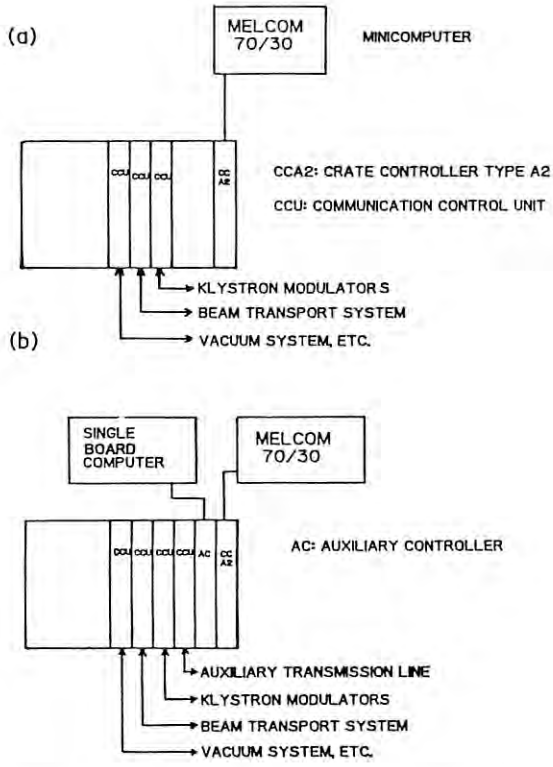

Fig. 8.2 Simplified block diagram for a sub-control station CAMAC system. (a) Single controller configuration using a minicomputer MELCOM 70/30. (b) Multiple controller configuration including an auxiliary controller and a single board computer with a 6800 type microprocessor.

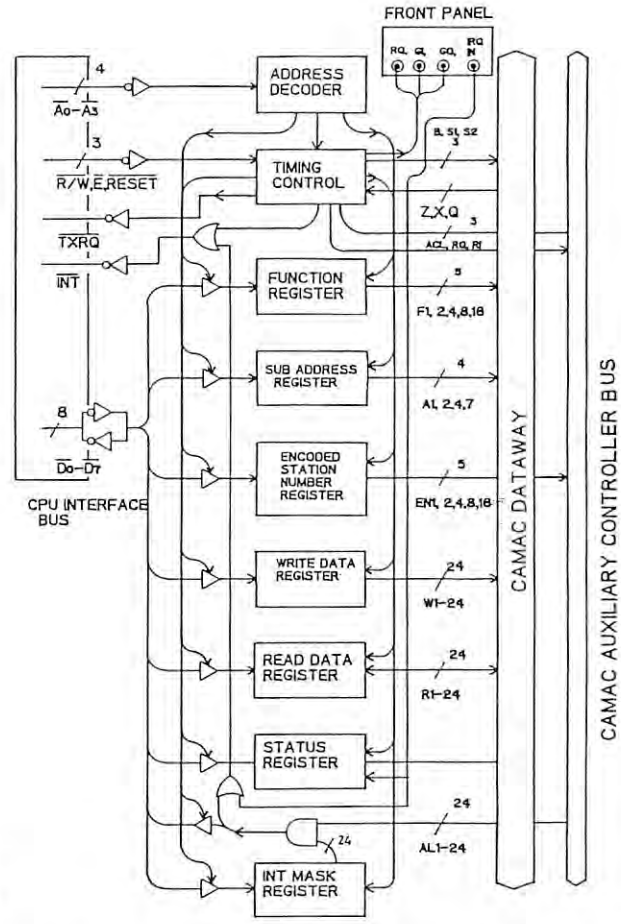

Fig. 8.3 Auxiliary crate controller circuit block diagram.

8.3 CAMAC test system

A useful CAMAC test system was constructed with an auxiliary crate controller and a personal computer FM-11. Figure 8.4 shows the system block diagram. Any CAMAC module can easily be tested by the system using a BASIC interpreter. A multi-user system can be made up with multiple auxiliary controllers and personal computers. Using this test system, linac equipments (klystron modulators, vacuum system controllers, etc.) may be tested even when the linac is being operated.

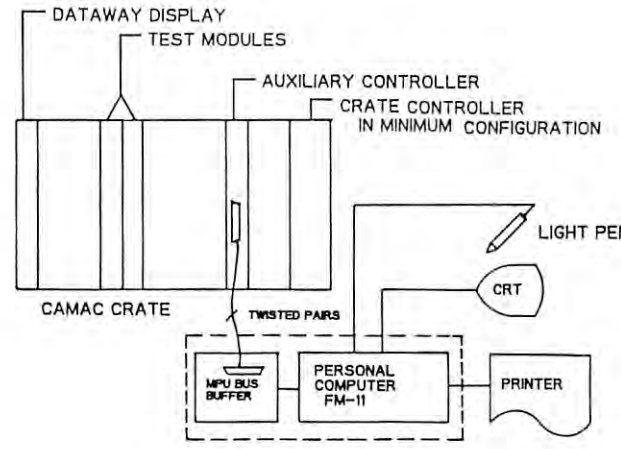

Fig. 8.4 CAMAC test system using an auxiliary crate controller and a personal computer.

9. BEAM CHARACTERISTECS MEASUREMENT

9.1 Introduction

Beam characteristics are usually described as those of a pulse as a whole, but may change in the course of time within the same pulse. This is often experienced when the beam energy is analyzed. Therefore, experiments are made to measure the variation of the bunch width and energy spread as a function of time in one pulse, the bunch width is one of the fundamental quantities which determine the energy spread.

9.2 Bunch width measurement

The method used to measure the bunch width is reported previously, and here described only briefly. The width is estimated from the energy spread of the beam with a special procedure to reduce the relative energy spread arising from other reasons than the finite bunch width. More specifically, in the injector the beam is accelerated at an optimum rf phase, and then accelerated in the first sector at an rf phase angle deviated from the top by certain amount and the beam energy spectrum is analyzed. Figure 9.1 is an example of the data thus obtained. The parameter indicated is the time in the pulse measured from the rising point of the pulse. In this experiment the injection current from the gun is varied and similar measurements are performed. The results are summarized in Fig. 9.2. As is seen in the figure, the bunch width remains constant, 1 to 2 degrees, as far as the current is less than 200 mA. When the current is increased above this value the width also increases, this fact is consistent to that reported previously. Furthermore, there seems to be a tendency that this width increase is more clear at earlier time than at later time in the same pulse, although the reason is not yet clear.

9.3 Energy spectrum measurements

The variation of energy spectrum with the time is measured at the end of the injector with an energy analyzing system consisting of an analyzing magnet, a slit and a beam catcher. The results are summarized in Fig. 9.3. A substantial difference is that the beam energy is higher at the beginning of a pulse due to the effect of rf tranjent state as is expected. Except this difference there is not much difference in the energy spread itself as is seen in the figure.

The beam characteristics so far discussed are with a long pulse beam. As for a short pulse beam, the energy spread is measured with the same analyzing system except that the beam catcher is replaced with another one of a coaxial type. The beam has a width of about 1.5 nsec and a peak current of 100 mA. The result is shown in Fig. 9.4. The spectrum shows a wide flat top, which is due to the fact that the resolution of the analyzing system is only about 0.8 %. Therefore, the actual energy spread is much less than that shown in the figure, and probably about the same magnitude as the resolution. This spread is much smaller than that of a long pulse because there is almost no beam loading effect for a short pulse beam.

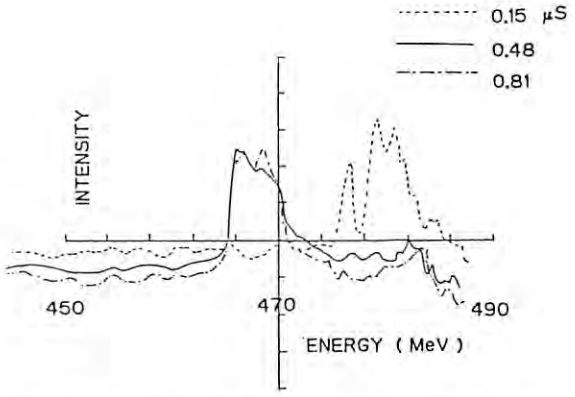

Fig. 9.1 Energy spectra at various times in a pulse.

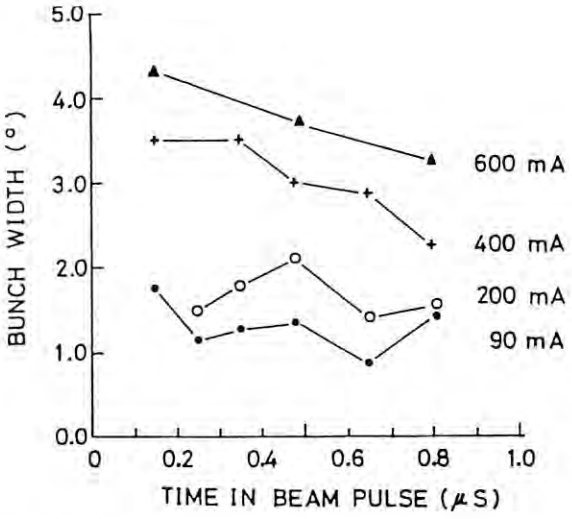

Fig. 9.2 Bunch widths at various times in a pulse. The parameter is an injection current.

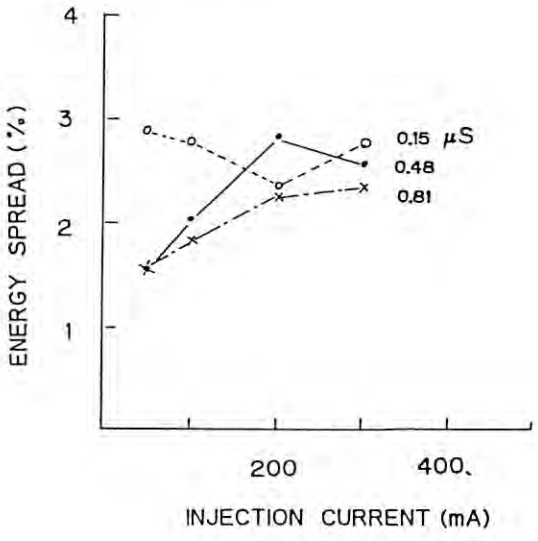

Fig. 9.3 Energy spread as a function of injection current.

resolution. This spread is much smaller than that of a long pulse because there is almost no beam loading effect for a short pulse beam.

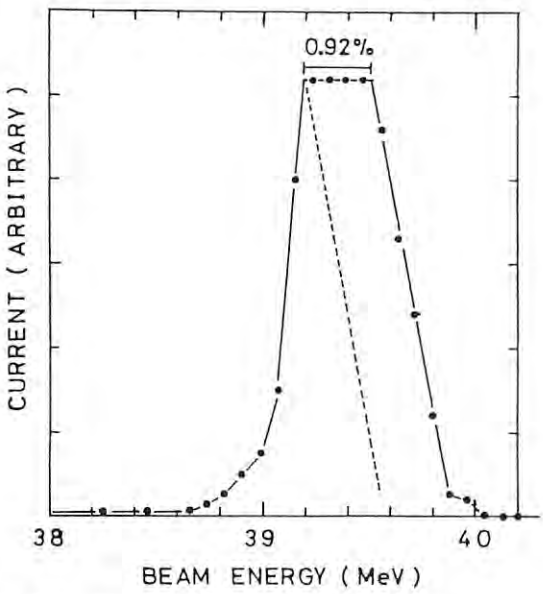

Fig. 9.4 Energy spectrum of a short pulse beam.

10. POSITRON GENERATOR CONSTRUCTION STATUS

10.1 Introduction

The positron generator is a positron source for the TRISTAN project. The construction started in 1982 with the budget of about 1 Billion yen; it is scheduled to be completed by the end of March 1985.

It was designed to produce a short ($\approx$1.5 ns) and high intensity (up to 10 mA) positron beam. The generator consists of an upstream linac capable of accelerating high intensity electron beam up to an energy of 200 MeV, a positron production target and a 250 MeV downstream linac for positron acceleration. They are housed in a two-storied building about 90 m long which is located on the west side of the PF linac. Figure 10.1 shows a sketch map of the positron generator linac, and the general parameters are listed in Table 10.1. Most of the components were fabricated so as to maintain replaceability with those of the PF linac.

This positron generator will be used also for the positron beam injection into the PF storage ring, since it has been experienced in other laboratories that the positron beam stored in the ring is considerably stable as compared with electron beam storage.

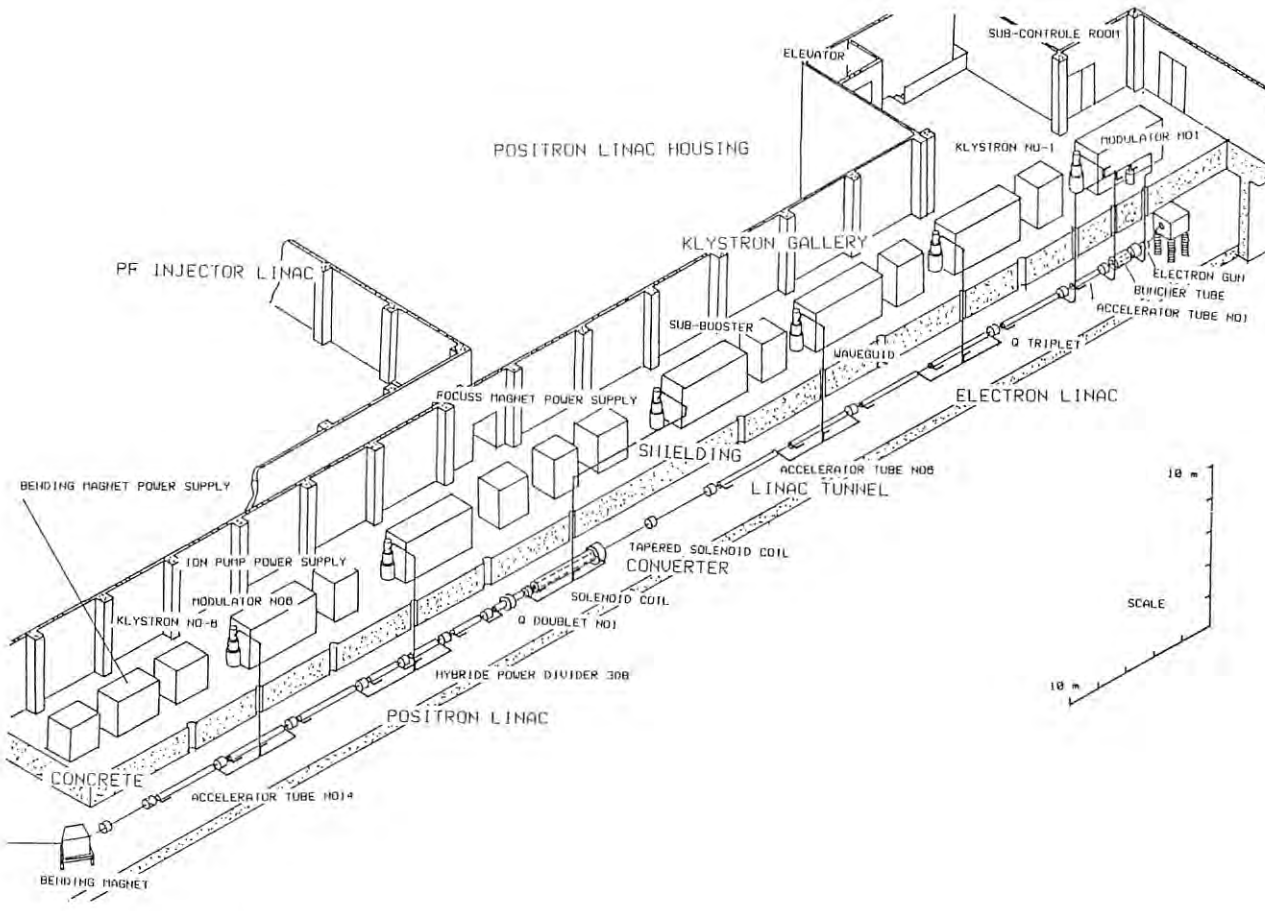

Fig. 10.1 Sketch map of the positron generator linac layout.

Table 10.1 General parameters of positron generator linac.

	Electron linac (Upstream)	Positron linac (Downstream)
Energy (MeV)	200	250
Peak current (mA)	10,000	10
Beam pulse width (ns)	1 - 2	1 - 2
Pulse repetition rate (pps)	50	50
Accelerator guide		
Type	quasi-constant gradient	quasi-constant gradient
Length and numbers	4 m × 5	4 m × 4
	2 m × 1	2 m × 4
	1.5 m × 1	
Microwave frequency (MHz)	2856	2856
Number of klystrons	3	3
Peak output power of klystron (MW/klystron)	30	30
Pulse width of microwave power (μs)	3.5	3.5

10.2 Acceleration unit

The accelerator guide system of the positron generator consists of 6 acceleration units. Four of them were fabricated in FY1983. The remaining units are fabricated in FY1984.

Structure of acceleration units

Six acceleration units are arranged along a beam line and are named units P-1,..., P-5 and P-6, respectively, from the upstream to the downstream. The 3 units (P-2, P-3 and P-6) have a same structure and the remaining 3 units (P-1, P-4 and P-5) are individually different structures. The unit P-1 is composed of a pre-buncher (0.3 m long), a buncher (1.5 m long), a short accelerator guide (2 m long) and a long accelerator guide (4 m long). The other units (P-4 and P-5) are also composed of two short accelerator guides and a long one, and are arranged in reverse order each other. Each of the standard units are formed with two long accelerator guides mounted in series on a support girder; the unit is illustrated in Fig. 10.2.1. The basic component parts of the unit are as follows: accelerator guides, rectangular waveguides, alignment equipments, vacuum manifolds, ion pumps, beam ducts and some supporting stands. The microwave power out of a klystron is divided into two branches with a hybrid divider to be fed to the two long accelerator guides of an acceleration unit.

Both ends of a long accelerator guide are supported with two large stands; its middle point is also supported with a small pole stand. In order to align the accelerator guides using a laser beam, each supporting stand has individually a light axis detector which is used as a reference point.

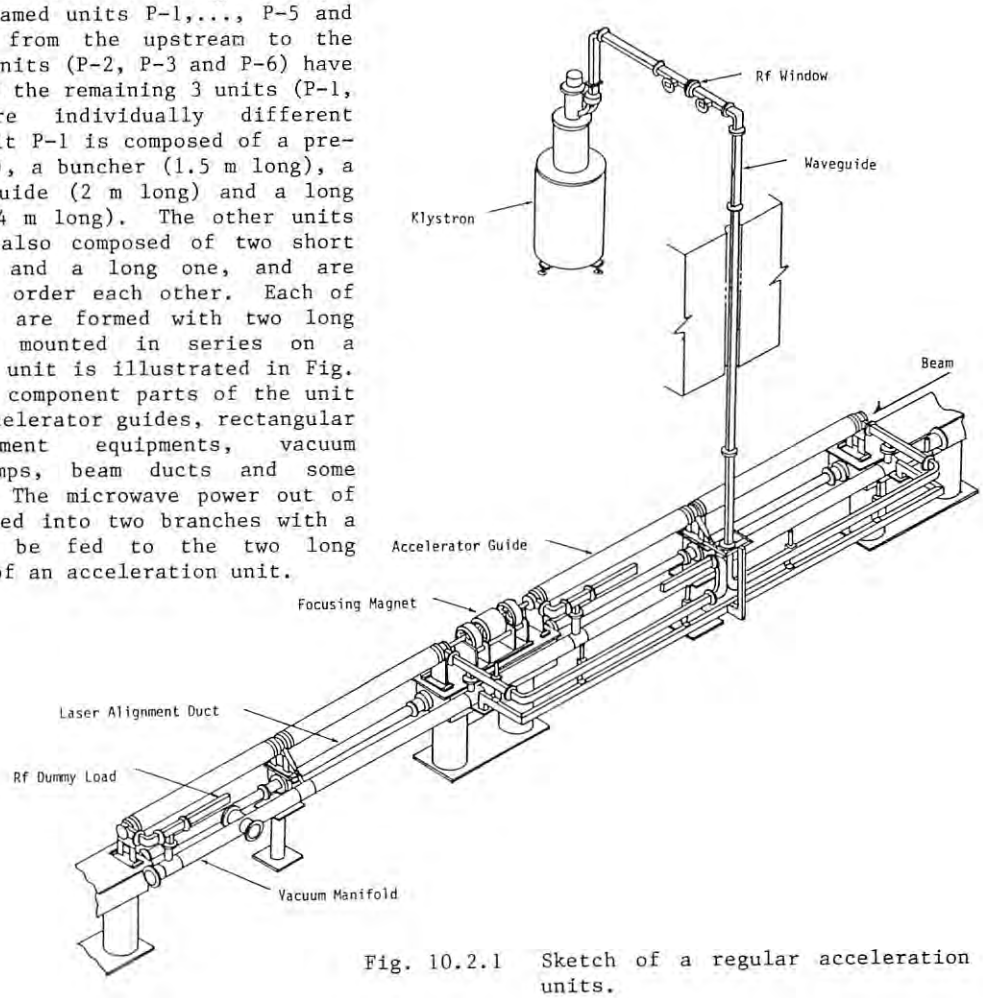

Fig. 10.2.1 Sketch of a regular acceleration units.

The special broad supporting stands are prepared in the units P-1 and P-4 to set up various focusing coils on them. The upper racks of those stands are made of casting aluminum metal to avoid magnetic field distortion as much as possible. An rf power loss in a rectangular waveguide system was estimated to be 0.5 dB from the klystron to the entrance of each accelerator guide.

Accelerator guide

A disk-loaded accelerator guide is made in such a way that disks and cylinders are alternatively piled up and solidified by electroplating method. A 2 m long accelerator guide contains 54 cells and two coupling cavities; the coupling cavities are fitted on both ends of the guide,

A technical development made possible manufacturing of a 4 m long accelerator guide. The long guide was welded two 2 m long guides inserting buffer cells. For evacuation, 16 small holes 5 mm in diameter were bored through the outside wall of the buffer cells. Electrical contacts between those guides are kept by welding stress by which the guides were joined together. Figure 10.2.2 shows the joint in detail.

The long guide was designed to obtain the accelerating energy of 44.3 MeV with the rf power of 12.5 MW without beam loading; consequently, a disk hole diameter at the entrance became 26.12 mm and the diameter gradient was decided to the step of 60 μm/cell.

Figure 10.2.3 shows calculated electric field strength on the guide axis and flowing rf power into the long guide without beam loading. Figure 10.2.4 shows shunt impedance and group velocity and Fig. 10.2.5 shows a relation between disk hole diameter 2a and inner diameter 2b of spacer cylinder. Some design parameters for the long accelerator guide are listed in Table 10.2.1.

Table 10.2.1 Accelerating structure characteristics for the positron generator linac

Type of structure	Approximately constant gradient, travelling wave $2\pi/3$ mode.
Operating frequency	2856 MHz
Number of long accelerator guide	9
Number of short accelerator guide	5
Length of long accelerator guide	3.999 m
Length of short accelerator guide	1.982 m
Number of cavities per long guide	110
Number of cavities per short guide	54
Field attenuation parameter in a 4 m long guide	0.685
Shunt impedance for fundamental space harmonic (r)	53.67-60.25 MΩ/m
Group velocity (v_g/c)	0.0084 -0.0227
Q factor	13500-14290
Filling time	0.960 μs
Waveguide inner diameter, 2b	8.189-8.333 cm
Iris aperture diameter, 2a	1.976-2.618 cm
Disk thickness	0.500 cm
Klystron peak output power	25 MW
Average number of accelerator guides per klystron	4
Average energy gradient at normal operating level	11.3 keV/cm

All of the disk-loaded guides for the PF injector were fabricated with vacuum melted copper (VMC); however those for the positron generator were changed into a special OFHC. It was done for cost-saving, because it was found that the total quantity of released gases from the OFHC was the same order as that of the VMC.

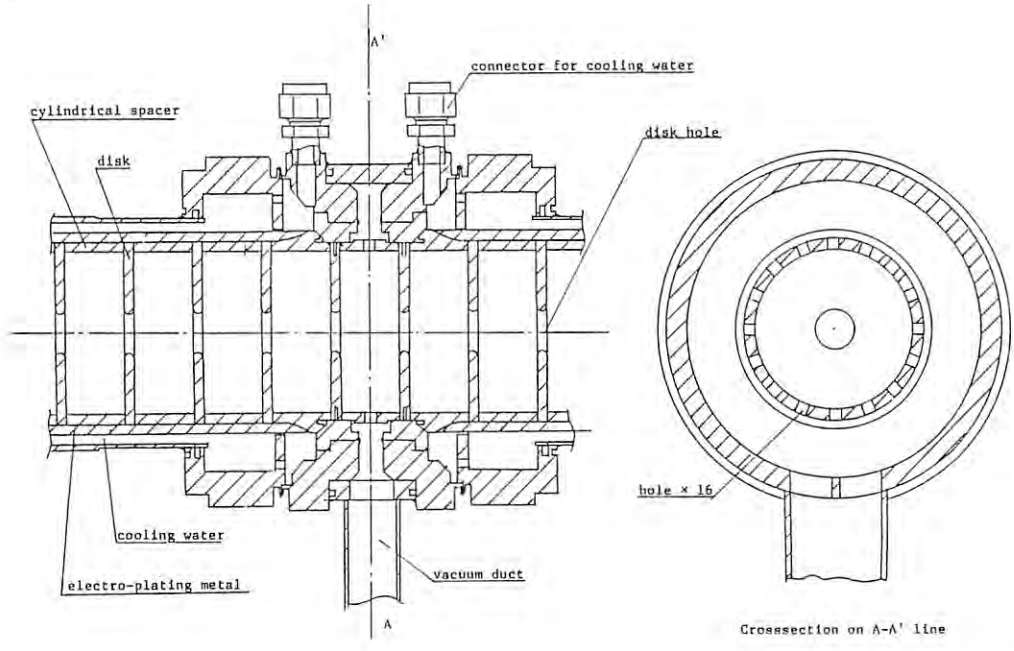

Fig. 10.2.2 Section view of connection part for a long accelerator guide with a buffer guide.

The two long guides was actually installed into the acceleration unit (5-7) in the PF injector, and the field test was finished without any trouble. Accelerating characteristics for the long guide was also investigated during its field test, and the measured values of the acceleration energy well agreed with the detailed calculation results. Two 2 m long guides of the units P-4 and P-5 are installed in series and are electrically connected by a waveguide, and those combined characteristics are almost the same as that of the 4 m long guide.

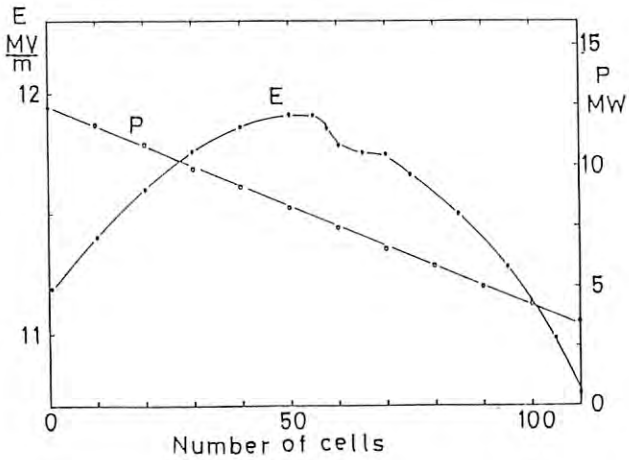

Fig. 10.2.3 Calculated electric field strength on the guide axis and flowing rf power into a long accelerator guide without beam loading.

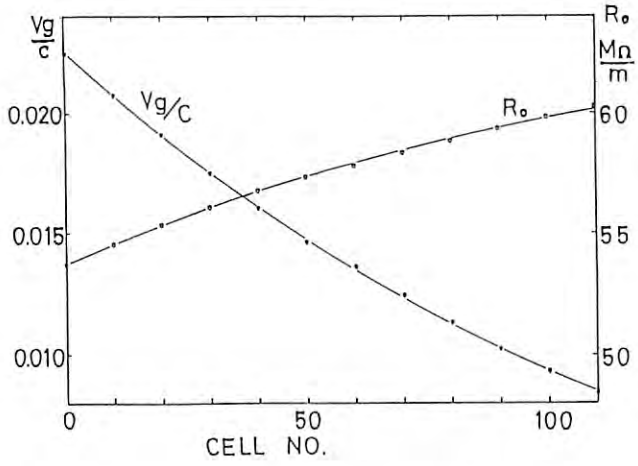

Fig. 10.2.4 Shunt impedance for fundamental space harmonic and group velocity located along the long accelerator guide.

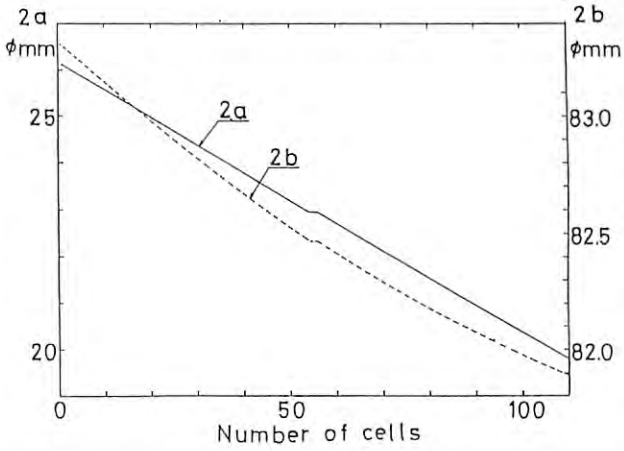

Fig. 10.2.5 Relation between iris aperture diameter 2a and waveguide inner diameter 2b within a 4 m long accelerator guide.

Positron generator tunnel.

Positron generator building.

10.3 Beam transport system

A beam focusing system was designed on the basis of the beam envelope calculation. All of the quadrupole magnets and their power supplies were fabricated. These power supplies were already installed into the racks located in the klystron gallery.

The architecture of the magnet power supply control system for the positron generator was changed from that for the PF linac. In the PF linac, power supplies are controlled by local control units each of which contains 16 monolithic digital-to-analog converters (DAC), an analog-to-digital converter (ADC) and other circuits, and can control 16 power supplies as shown in Fig. 10.3.1; in the positron generator, on the other hand, DAC's and ADC are excluded from the local control unit and distributed into each power supply. A compact printed circuit board with a DAC, an ADC, a UART (universal asynchronous receiver transmitter) and other control circuit is built in every power supply case. Figure 10.3.2 shows this printed circuit board. The power supplies are connected to their associated local control unit through a 48 kbps asynchronous communication loop. One can control power supplies from a local control unit panel or from the main operator's console in the same way as the PF linac system. One local control unit can control 64 power supplies at maximum. The system block diagram is illustrated in Fig. 10.3.3. Introduction of the new system reduced the number of wires required to connect power supplies with the local controller, and made it possible to locate a power supply anywhere.

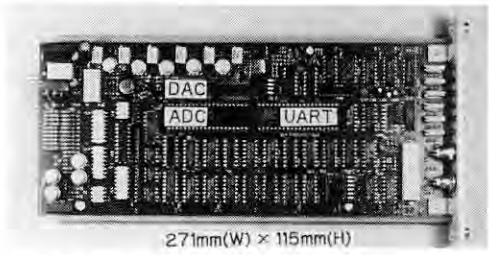

Fig. 10.3.2 Printed circuit board built in the magnet power supply in the positron generator.

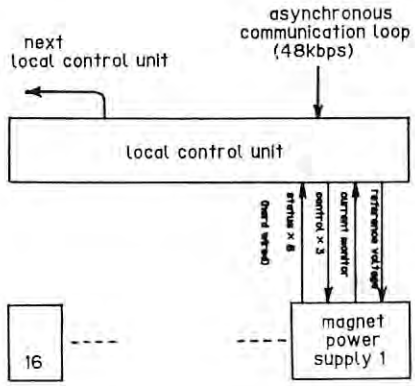

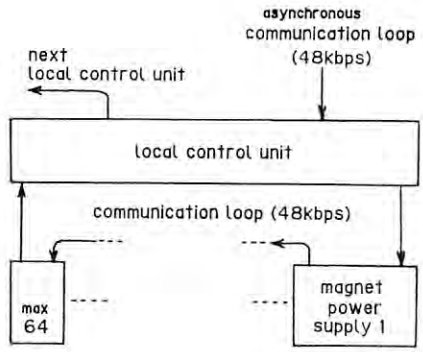

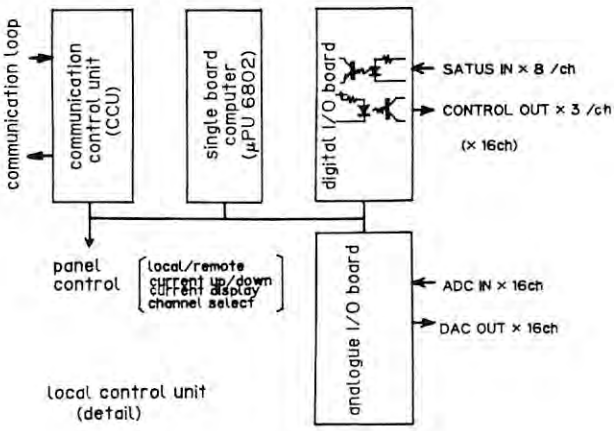

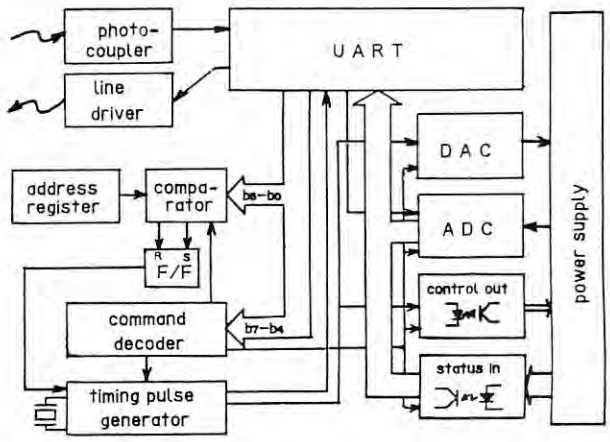

Fig. 10.3.1 System block diagram of the magnet power supply control in the PF linac.

Fig. 10.3.3 System block diagram of the magnet power supply control in the positron generator.

10.4 Rf system

The rf system of the positron generator is now under construction. The system is composed of five stages: a master oscillator (cw, 119 MHz), a main booster amplifier (cw, 476 MHz), a subharmonic buncher (SHB) amplifier (pulsed, 119 MHz), a sub-booster amplifier (pulsed, 2856 MHz) and six high power klystrons (pulsed, 2856MHz). The output rf power of each klystron is 30 MW and is split to be fed into two accelerator guides composing one acceleration unit. The main parameters of the rf source are as follows:

Number of klystrons	6
1 for the injection system	
2 for accelerating the electron beam	
3 for accelerating the positron beam	
Peak power per klystron	30 MW max
RF pulse length (flat top)	2 μs
RF repetition rate	50 pps max
Operating frequency	2856 MHz

It is necessary to adjust the rf phase of each klystron drive signal to the correct acceleration angle in order that the rf wave crest coincides with the electron bunch to within ±2°. The system which transmits the coherent rf wave to each klystron is the "drive system", which is shown in Fig. 10.4.1.

The master oscillator generates 119 MHz rf signal which is fed to both the main booster and the subharmonic buncher amplifier. The main booster multiplies the frequency to 476 MHz and amplifies the power to 1 kW (cw) by a solid state (10 W) amplifier and a cw klystron (Varian 3KM 3000LA). A part of the output power is supplied to the positron generator (100 W), and the rest is to the PF electron linac ($\gtrsim$ 1 kW) through the main drive lines in the frequency of 476 MHz, the sixth subharmonic of the accelerator frequency. This rf transmission for 476 MHz instead of 2856 MHz reduces transmission loss in the 400 m long main drive line of the PF electron linac. The main drive line of the positron generator transmits this rf power to a frequency multiplier followed by a 2856 MHz amplifier where the rf is multiplied from 476 to 2856 MHz and is amplified to two 10 kW pulse rf by the sub-booster klystrons (Thomson CSF TH2436). The sub-booster is installed at the middle of the klystron gallery of the positron generator. A subdrive line with two directional couplers transmits the 2856 MHz, 1.5 kW rf power to each of the three high power klystrons in one side of the sub-booster. The 2856 MHz rf power is amplified up to 30 MW by the high power klystron (MELCO PV3030A) and is fed to two accelerator guides through high power wave guides.

The SHB amplifier composed of transistors and a hard tube (Eimac 7651) supplies 5 kW rf power of 119 MHz to the SHB cavity. The six klystron modulators have been installed in the klystron gallery. Coaxial cables for the main drive, subdrive and signal monitor lines also have been laid.

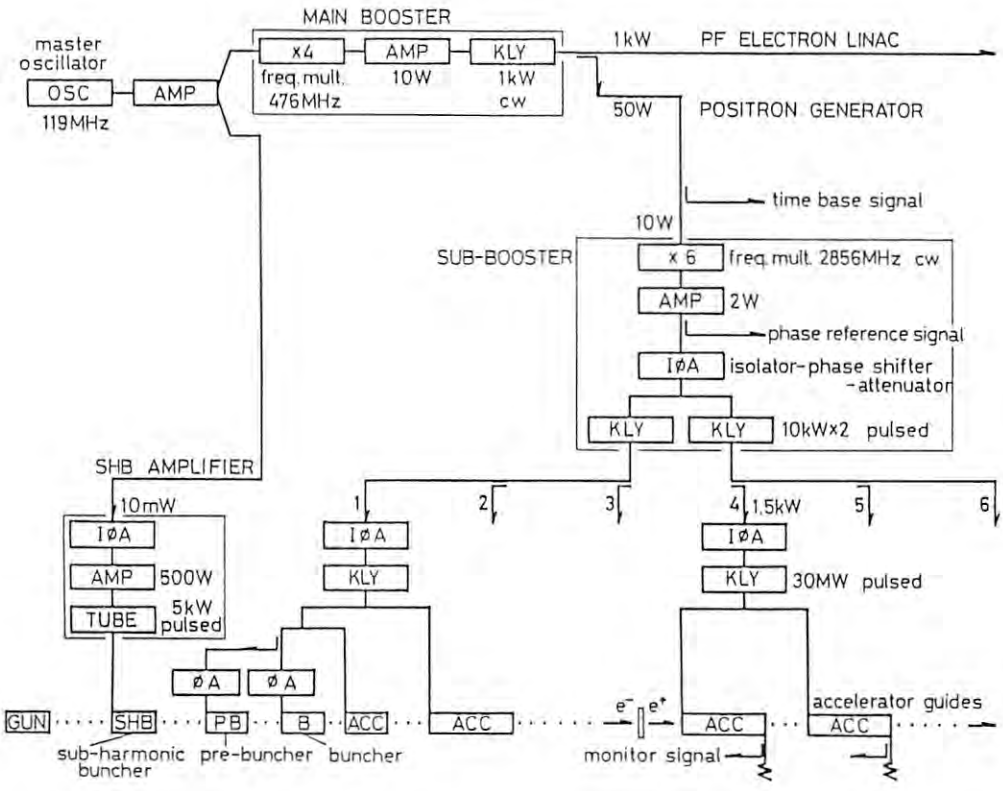

Fig. 10.4 1 Block diagram of the positron generator rf system.

10.5 Injection system

Introduction

Positrons produced by this generator are accelerated with the PF linac, TRISTAN accumulation ring and main ring to be used in high energy physics research on $e^+ - e^-$ collission experiment. To obtain a good statistics in the measurements, the positron beam intensity must be sufficiently high; it should be at least several mA in the linac. The electron to positron conversion efficiency is of the order of 10^{-3} around an electron energy of 200 MeV which is the designed electron energy at the converter. The expected maximum electron beam current at the converter is 10 A; higher the current, it is naturally more desirable.

Main components of the injection system are an electron gun, a prebuncher, a buncher and two accelerator guides. These components are similar to those of the PF linac; however, the gun injection voltage and RF power dividing system are different between the two injection systems. The injection voltage in the PF injector is 100 kV, but it is to be raised to 150 kV in the positron generator to make it easier to draw a high current and to simplify the beam focusing. In the PF linac the output of the high power klystron is divided in such a way that a half of the power is fed to the buncher and two of a quarter power to each 2 m long accelerator guide, while in the positron generator two of quarter rf power are fed to the buncher and a 2 m long accelerator guide, respectively, and a half power to a 4 m long accelerator guide. The latter configuration is obviously more advantageous to gain energy than that of the former where the energy gain is not very significant.

Design of prebuncher and buncher

A typical example of the beam trajectories with the final α and β values is shown in Fig. 10.5.1. The first part of less than 1.63 corresponds to the prebuncher, where electrons are weakly modulated to form a bunch. The following $(1 + 1/2)\lambda$ long space is a free space, and at the end of it a bunch is roughly formed. Weak modulation in the prebuncher seems to be important. At the entrance of the buncher the beam phases are shifted by 30° in Fig. 10.5.1, this means that the rf phase of the buncher is changed by this amount relative to the prebuncher.

In the initial part of buncher weakly bunched beam starts to be modulated strongly to form a tight bunch. This is an important part to accelerate high currents, and it is necessary to keep beam trajectories no intersecting one another as much as possible.

The final parameters are listed in Table 10.5.1, and the beam phase and energy at the output of the buncher are plotted as a function of the beam phase at the input in Figs. 10.5.2 and 3.

Beam transport system

A solenoidal magnetic field to produce Brillouin flow is most suited to transport high current beams with an energy around 150 keV from

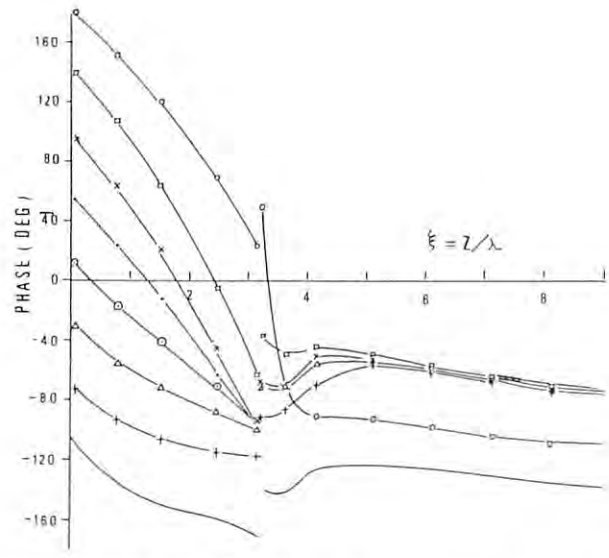

Fig. 10.5.1 Typical beam trajectories in the prebuncher and buncher.

Table 10.5.1 α and β values

PREBUNCHER			BUNCHER		
CAV. No.	α	β	CAV. No.	α	β
1	0.036	0.70	1	1.37	0.78
2	0.038	"	2	1.43	0.80
3	0.040	"	3	1.50	0.83
4	0.042	"	4	1.58	0.87
5	0.044	"	5	1.66	0.91
6	0.046	"	6	1.72	0.945
7	0.048	"	7	1.77	0.965
			8	1.82	0.983
			9	1.86	1.00
			10	1.90	"
			.	"	"
			.	"	"
			.	"	"
			44	1.90	1.00

the gun to the prebuncher. In the prebuncher and buncher where the energy is still not very high, a solenoidal field is also effective to transport these high current beams with a fairly large emittance.

At higher energies after the buncher, quadrupole magnets are more effective in beam focusing. Arrangement of transport elements in the injection system is shown in Fig. 10.5.4, and the beam envelope expected is shown in Fig. 10.5.5. These transport elements are under construction.

Electron gun and modulator

The electron gun to be used is similar to that used in the PF linac with some modification of the shape of electrodes. Another gun with a grid-cathode assembly of an EIMAC Y-796 tube is also planned for use.

The gun high voltage modulator was already manufactured, and its main parameters are as follows: The output voltage is variable from zero to 16 kV, and the output impedance is 12.5 Ω. The pulse has the flat top more than 2 μs and a flatness less than 0.3 %. A pulse transformer with a step-up ratio of 1 : 12 and a high voltage station were also made.

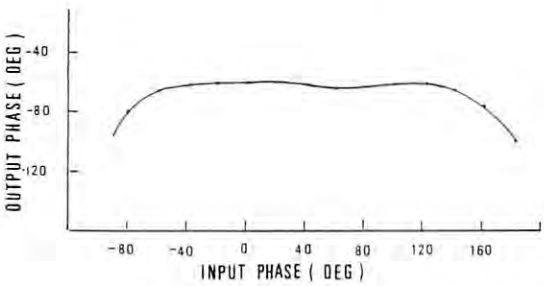

Fig. 10.5.2 Output beam phase versus input beam phase.

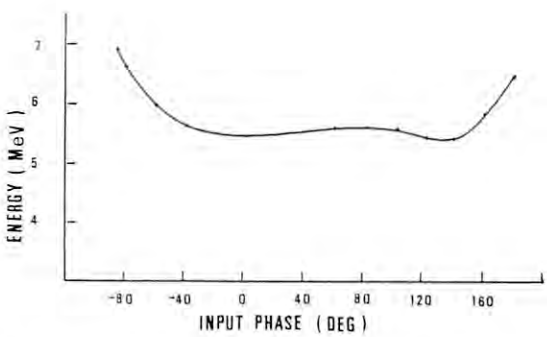

Fig. 10.5.3 Beam energy versus input beam phase.

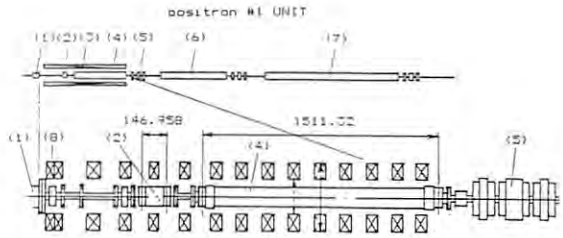

Fig. 10.5.4 Layout of injector. (1) Gun, (2) prebuncher, (3) solenoid coils, (4) buncher, (5) Q magnet, (6) 1st accelerator guide, (7) 2nd accelerator guide and (8) current monitor.

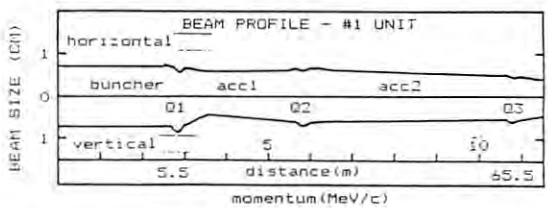

Fig. 10.5.5 Calculated beam envelope in the injector.

10.6 Positron production target

Positrons are generated in the following way. High energy electrons hit a target material with a large Z number are converted to high energy X-rays, i.e., Bremsstrahlung. These X-rays interact with atomic nuclei in the target and produce pairs of an electron and a positron. The target must be thick enough to produce sufficient X-rays but not too thick to cause an appreciable attenuation of the produced positrons. In the present positron generator, the energy of the incident electrons is planned to be about 200 MeV and the target, a tantalum plate, must have the thickness between one to two radiation lengths in this electron energy region.

Positrons thus produced have a large energy spread and are emitted in a fairly large forward solid angle. To collect these diverging positrons as much as possible, a strong solenoidal magnetic field is required and, therefore, a solenoidal coil which is pulsed to produce 5000 G is under design. Positrons emitted within a solid angle of 100 msr with an energy of 5 MeV to 15 MeV will be collected and accelerated with the following accelerator guides. The number of positrons thus collected is expected to be of the order of 10^{-3} per an incident electron.

The target should be cooled by water and is expected to become very radioactive, so that it will be shielded by lead 5 cm thick to reduce radiation in the vicinity of the target.

10.7 Trigger system

The trigger system for the positron generator is similar to that for the PF Injector linac. Most of the circuits have already been provided; coaxial cables for trigger signal transmission were laid down between trigger circuits, a gun pulser and klystron modulators. The block diagram of the positron generator trigger system is shown in Fig. 10.7.1. The function of this system is described below.

In a test operation independent of the PF linac, a master trigger pulse is generated in the positron generator trigger system itself. When positron beam is injected into the PF linac, the master trigger pulse is fed from a master trigger generator of the PF linac. A signal denoted by "TRIGGER-1" in Fig. 10.7.1 provieds the repetition rate of the high voltage klystron modulators and the TRIGGER-2 gives the repetition rate of the gun grid pulser. In an rf synchronizer circuit, the klystron trigger, ring trigger, monitor trigger and gun grid pulser trigger are synchronized with the accelerating frequency of the PF ring (500 MHz) or that of the AR (508 MHz) as well as the revolution frequency of the PF ring (1.6 MHz) or that of the AR (0.8 MHz). The last three of the four kinds of rf-synchronized triggers have the same repetition rate. The ring trigger is used as a trigger of pulsed septum and kicker magnets excitation for beam injection, and is outputted at the same time with the klystron trigger 100 μs earlier than the gun grid pulser trigger. The monitor trigger is outputted 1 μs earlier than the gun grid pulser trigger, and is used as a trigger of oscilloscopes. The klystron trigger is delayed coarsely by the main variable delay modules and finely by the sub-variable-delay modules. A step of delay time is 105 ns for the former and 21 ns for the latter.

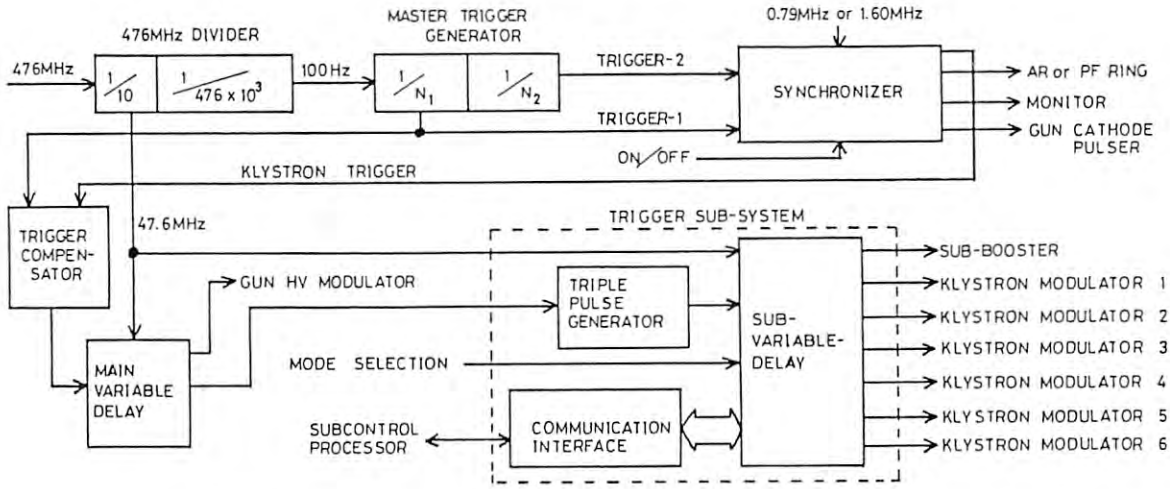

Fig. 10.7.1 Block diagram of the positron generator trigger system.

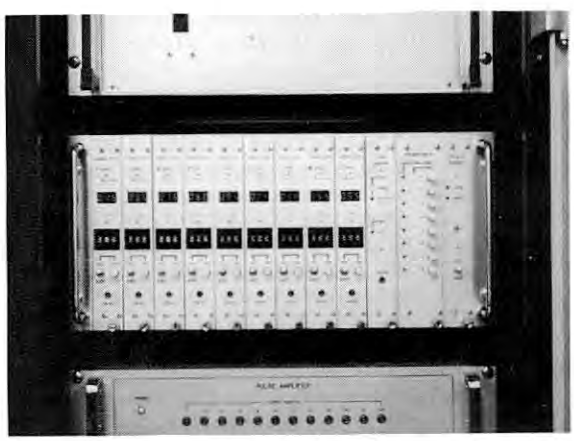

Trigger subsystem

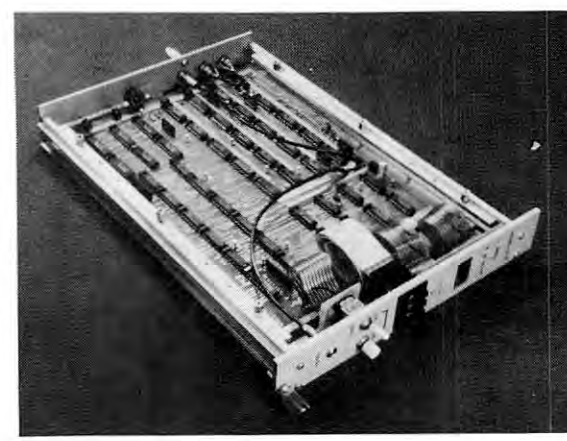

subvariable delay modules.

10.8 Control system

By the end of FY1983, most of the positron generator control system hardware had been provided. Cables for the radiation sefety interlock system and beam monitors were laid in October 1984. Software production is in progress.

The general principle for the positron generator control system construction is the same as that for the Photon Factory (PF) 2.5 GeV electron linac: Autonomous operation capability of every terminal equipment (klystron modulators, magnet power supplies, etc.), a completely hard-wired logic safety interlock system, system construction with easily replaceable modules and real-time remote control through computerized communication system with noise-free fiber optics.

The positron generator is to be controlled by a newly designed multi-microprocessor CAMAC complex system which forms one of subcontrol stations of the PF linac. The positron generator is required to be operable independently of the PF linac; it is matter of course that the new subsystem should be designed to be also operable from the PF linac main operator's console. All functions of the positron generator operation are concentrated in a subcontrol room with an area of 4.8×8 m^2 situated at the south end of the positron generator building.

The basic design of the communication system for the positron generator control is the same as that for the PF linac; however a subcontrol station for the positron generator is designed to be fairly different from the PF linac system as a result of recent technical innovations for microelectronics.

The PF linac control system has six subcontrol stations distributed along the linac at intervals of 80 m. Every subcontrol station consists of a minicomputer with a general-purpose operating system, a CAMAC crate and subcontrol panels with voltage and current meters, status indicating lamps, switches, etc. connected to various terminal equipments by hard-wiring. In contrast with this system, the positron generator subcontrol station is composed of a multi-microprocessor controlled CAMAC system and a local operator's console with five graphic display terminals. This subsystem has no 'central processor' like a minicomputer in the PF linac; that is a completely distributed processing system with many single-task-executing microprocessors. An outstanding feature of a multi-processor system, where every processor executes only one task, is simpleness of the software; any complicated multi-tasking operating system can be excluded.

Communications between the subcontrol station and terminal equipments are made in the same way as the PF linac communication system. Two kinds of bit serial communication loops are used: One is 'LOOP-II' with a 500 kbps synchronous transmission mode based on the High-level Data Link Control procedure (HDLC), and the other is 'LOOP-III' with a 48 kbps asynchronous transmission mode based on the Basic Mode procedure where a transparent mode protocol is adopted to transmit binary data. Figure 10.8.1 shows a simplified block diagram of the positron generator control system.

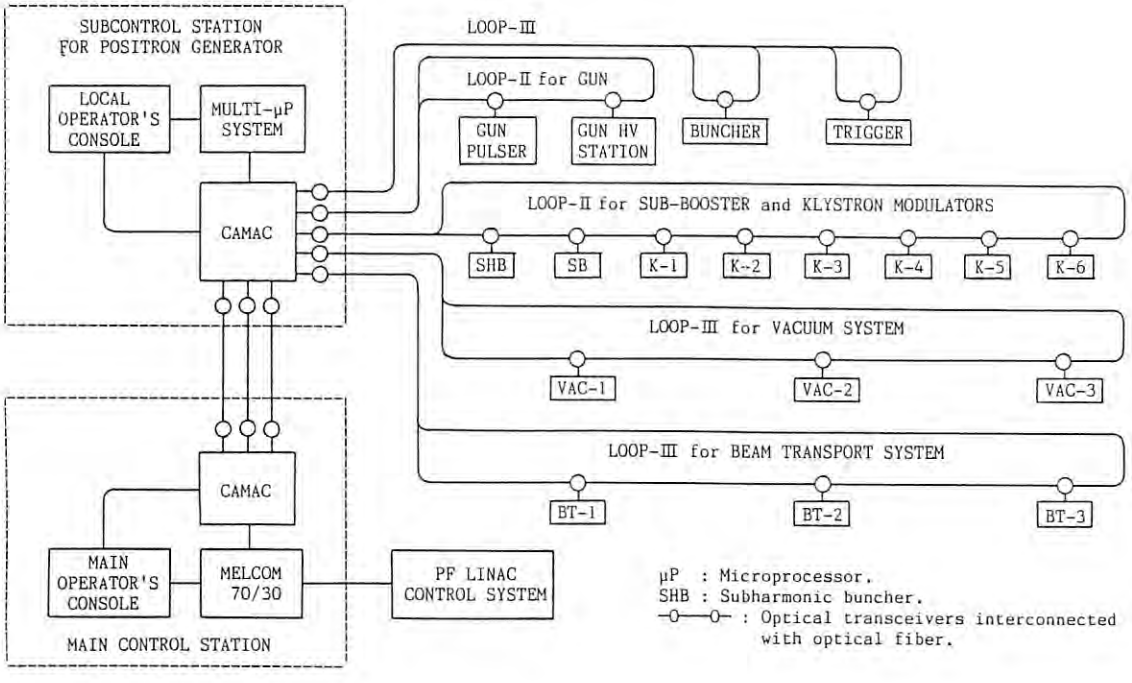

Fig. 10.8.1 Positron generator control system block diagram.

LIGHT SOURCE DIVISION

1. INTRODUCTION

The 2.5 GeV electron storage ring constructed at the Photon Factory, KEK, is a dedicated machine for the research work with synchrotron radiation. Present parameters of the storage ring are listed in Table 1.1. Although the 3 GeV operation of the ring was accomplished in June 1983, the ring has been operated at the nominal energy of 2.5 GeV, because the RF power is insufficient. In the normal operation the critical wavelength of the synchrotron radiation is 2.98 A. A superconducting vertical wiggler has been operated normally in the user's time since February 1984. The aimed field strength is 6 T, though the wiggler is now operating at 4.5 T because above 4.5 T was observed some beam instability. This field strength give the critical wavelength of 0.64 A, which makes it possible to do research works using hard X-ray around 0.2 A. The permanent magnet undulator which has 60 periods has come into operation since February 1983. This supplies synchrotron radiation with high brightness in the wavelength region from 7 Å to 40 Å. The brightness is higher by about two orders of magnitude than that of synchrotron radiation coming from the bending magnet.

Table 1.1

Principal parameters of the storage ring

Energy	2.5 GeV max. achieved 3.0 GeV
Stored current	150 mA max. achieved 250 mA
Mean radius	29.77 m
Radius of curvature	8.66 m
Critical wavelength	2.98 A (0.5 A at 6 T wiggler)
Emittance	horizontal $5.4\pi \times 10^{-7}$ m.rad. vertical $6.5\pi \times 10^{-8}$ m.rad.
RF frequency	500.105 MHz
Harmonic number	312
No. of cavity	4
Radiation loss	399 keV/rev. (510 keV with wiggler)
Straight section	2 long 5 m 8 medium 3.5 ∿ 3.75 mm
Insertion devices	vertical wiggler 4.5 T (aimed 6 T) 60 period undulator k=1.78 ∿ 0.1
SR channel	SR Exp. 8, beam diagnosis 1
Vacuum pressure	3×10^{-11} torr no beam 4×10^{-10} torr at current of 100 mA
Beam lifetime	15 hr at I=150 mA. 30 hr at 100 mA
Injection energy	2.5 GeV
Injection rate	1 Hz
Injection time	1.5 ∿ 10 minutes

2. STORAGE RING OPERATION

2.1 GENERAL

The scheduled operation of the storage ring started in June 1982 (run 2), and the run 8 ended in July 1984. Except the run 2, which was used mainly for machine tuning up, the storage ring was routinely operated at 2.5 GeV in multi-bunch mode. So far the maximum stored current is 250 mA, though usually the initial stored current has been limited to 150 mA because of the heating problem of the vacuum chamber. In a normal operation week, the storage ring is operated from Tuesday morning 9 o'clock through Saturday morning. Of 96 hours operation, 64 hours are dedicated to user's experiments, 24 hours are used for the accelerator study and 8 hours for machine tuning up. From FY 1983, the storage ring has accumulated the beam at every beginning of the Linac study time, so that users can make experiment during this eight hours study. This is the reason why the user time has become more than two thirds of the total operating time, though the first week of every run was used only for machine tuning.

2.1.1 Beam Time Statistics

The beam time statistics from April 1982 to July 1984 is shown in Table 2.1.1. The net time used for experiments exceeds 90% of the scheduled user's time. On the otherhand the percentage of machine failure is less than 3%, and the percentage of injection time is less than 6%. In short, the storage ring has been operated quite efficiently and stably.

The injection rate is 1 Hz and the beam storing rate ranges from 0.1 mA/sec to 2 mA/sec depending on the matching between Linac (2.5 GeV) and the storage ring. The accumulating time is very short, say, a few minutes. However, some beam instability was observed during injection and it often took long time to accumulate beams up to 150 mA. In FY 1983, the average injection time was 15 minutes including confirmation of the radiation safety. While the study on beam instabilities has progressed since FY 1983, the average injection time in FY 1984 becomes longer and is about 20 minutes. The reason is that the wiggler has been operated in an amount of 45% in the total time and it takes about 20 minutes to excite the wiggler, because

Table 2.1.1

Beam time statistics

Fiscal year		1982	1983	1984*	total
Ring operation time	hr	1298	2047	811	4156
Integrated current	A·hr	58	157	67	282
User's time**					
scheduled	hr		1336	384	
operated	hr	661	1357	423	2441
effective time	hr	594	1241	381	
time for injection	hr		66	33	
machine failure	hr	67	31	3	
miscellaneous	hr		19	6	
integrated current	A·hr	40	123	39	202
average current	mA	68	99	101	
number of injection		233	261	67	
ave. injection interval	hr	2.6	4.8	5.7	
Wiggler operation					
operated time	hr		115	175	
average current	mA		103	92	
ave. injection interval	hr		3.3	5.3	

* till July 27

** including wiggler operation

the vertical wiggler operation consists of the following complicated procedure; scraping beams, reducing the current of the superconducting coils, moving up the wiggler magnet, injecting beams, moving down the wiggler and exciting the coils.

2.1.2 Improvement of Beam Life Time

As illustrated in Fig. 2.1.1, the weekly average of stored current has increased though the initial current is still limited to 150 mA, and now the average is about 100 mA inspite of the wiggler operation. The average time interval between injections has also become longer, and in December 1983, the injection was done once a eight hours. Both facts are mainly attributed to improvement in the beam lifetime, which also means also that the vacuum pressure has been improved through the operation. At the end of the run 8, the beam lifetime was 15 hours at the current of 150 mA and 30 hours at 80 mA. Figure 2.1.2 is the best example of the beam decay recorder. The initial current was 152 mA and 19 hours after the injection the stored current still remained 67 mA and the beam lifetime was 46 hours at this point.

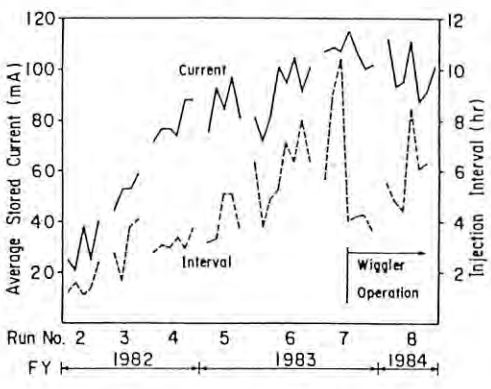

Fig. 2.1.1 Progress of the weekly average of stored current and of time interval between injections. Initial current is limited to 150 mA.

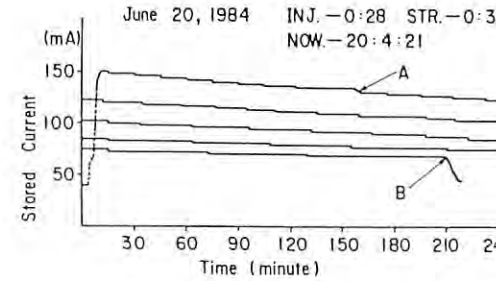

Fig. 2.1.2 The best example of the beam decay recorder. A and B show lifetime deteriorations.

2.1.3 Summary of Storage Ring Studies

The study on the storage ring itself is helpful to supply more stable and powerful synchrotron radiation for users. Accordingly, in a normal operation week, twelve hours are used for this study. The items of studies are as follows.

Tune diagram survey: On the tune diagram, except betatron resonance lines and their satellites, many lines or islands on which the beam lifetime is short are observed. Specially in the wiggler operation, the pattern of these lines or islands is complicated and seems to depends on the field strength of the wiggler. So extensive survey must be done to raise up the field strength of the wiggler.

Coupled bunch instabilities: A longitudinal instability which is excited by the higher order mode resonance of the cavity, 758 MHz, was observed. Also two horizontal instabilities (830 MHz, 1070 MHz) were observed and were cured by lowering the temperature of cavity with cooling water. The longitudinal instability gives no beam loss but causes the horizontal beam density modulation with the frequency of about 200 Hz, which sometimes makes the beam lifetime short. There are two RF stations in the ring and the suitable phase

change between two RF stations can cure this modulation, but the phase control is not so easy. Another method of the cure is to modulate the RF power with the synchrotron frequency, but this enlarges the beam size both in horizontal and longitudinal direction.

Two beam instability: This instability is caused by so-called ion trapping and induces the pulsation of beam density in the vertical direction. The partial fill operation, already mentioned, can eliminate the pulsation fairly well. Another method of the cure is that RF fields with the frequency of about 1.3 MHz are applied to the beam. The mechanisms of these cures are not clearly understood.

Head-tail instability: This instability was observed in the partial fill operation and more clearly in the single bunch operation. This instability was cured by operating the sextupole magnets which corrects chromaticities of both horizontal and vertical direction to zero or slightly positive value.

In the machine study, RF knock out electrodes measuring the betatron tune, the spectrum analyser measuring the frequency of a oscillation which is the origin of a beam instability, the television camera measuring the beam profile, the photodiode array measuring the electron density distribution, the counter telescope measuring bremsstrahlung, that is, measuring the local vacuum pressure at the electron beam, the undulator lights measuring the brightness of synchrotron radiation, were used as powerful apparatuses, and now a streak camera is introduced as a useful tool.

2.2 BEAM DYNAMICS

The storage ring is routinely stored with the beam of 150 mA in the multi-bunch mode at the present user time, with a long beam lifetime under the operation of the vertical wiggler and the permanent magnet undulator. Parameters of the storage ring is summarized in Table 2.2.1 together with symbols to be used in this report. Beam instabilities, which will be described in this section, sometimes bring problems to the machine operation especially during operating the vertical wiggler, because its beam chamber is narrow horizontally. Stability of the beam is, needless to say, important especially for the SR experiments. Therefore, the most of time in machine study has been occupied in investigation of the beam instabilities in order to suppress them. So far we have observed following instabilities:

(1) Coupled-bunch instabilities arising from the higher order mode resonances of the RF accelerating cavities.

(2) Vertical beam blow-up observed in the multi-bunch mode operation.

(3) Abrupt deterioration of the beam lifetime or sudden beam loss.

(4) Single-bunch head-tail instabilities observed with negative chromaticities.

The coupled-bunch instabilities (1) in the PF storage ring have been studied extensively and results of early studies were already reported[1,2,3]. In section 2.2.1, properties of the coupled-bunch instabilities will be summarized together with problems brought into the machine operation and the SR experiments. The instabilities (2) and (3) are probably both caused by the ion-trapping, although it is not clear yet. A forced oscillation externally applied to the beam can suppress the vertical instability, details of which will be described in section 2.2.2. Operation in the single-bunch mode will be described in section 3.3, where observed thresholds of the head-tail instability will be presented.

Table 2.2.1

Parameters of RF system

RF frequency	f_{RF}	500.105 MHz
Revolution frequency	f_r	1.60290 MHz
Harmonic number	h	312
Number of bunches	B	312
Momentum compaction factor	α	0.040
Synchrotron radiation loss	V_s	0.51 MV (6 T)
Power dissipated in cavities	P_c	116 kW
Cavity gap voltage	V_c	1.9 MV
Shunt impedance (four cavities)	R_s	33 MΩ
Unloaded Q-value of the fundamental mode	Q	37,000
Quantum lifetime	τ_q	4 days
Synchronous phase	ϕ_s	77°
Bunch length	τ_ℓ	79 ps
Synchrotron frequency	f_s	58 kHz
Field of vertical wiggler	B_w	6 T
Number of RF stations		2
Number of klystrons		2
Number of RF cavities		4

2.2.1 Coupled-bunch Instabilities

Summary of the coupled-bunch instabilities

Three coupled-bunch instabilities have been observed and they are all caused by the high coupling impedances of the RF accelerating cavities. The observed instabilities are summarized in Table 2.2.2, where the related cavity modes, resonant frequencies, and modes of the coupled-bunch oscillation are presented. If the bunches oscillate correlatively each other, the beam has the frequency components of

$$f^{\pm}_{\mu,n} = nBf_r \pm (\mu f_r + f_{osc})$$

Table 2.2.2

Summary of coupled-bunch instabilities. Observed resonant frequencies, Q-values and coupling impedances of the RF cavity are presented. Units of impedances are MΩ and MΩ/m for TM0 and TM1 modes, respectively.

Cavity mode		Frequency (MHz)	$Q_{exp.}$	R (MΩ or MΩ/m)	Mode of coupled-bunch	Instability	Problems
"758"	TM011-like	758	19,000	3.02	161	Longitudinal	Short lifetime
"1070"	TM111-like	1070	21,000	27±1	268	Horizontal	Beam loss
"830"	TM110-like	829	29,000	12±1	103	Horizontal	Beam loss

for zero and positive integer values of n. Where B is a number of bunches, μ an interger of 0 to B-1 representing mode number of coupled-bunch oscillation, and f_{osc} is a reminder of the oscillation frequency divided by the revolution frequency f_r. From the frequency spectrum of the beam signal, the mode number μ in Table 2.2.2 can be derived using this relation.

(1) The longitudinal coupled-bunch instability "758" leads to no beam loss at least up to 250 mA. The growth of the oscillation amplitude seemed to stop at a certain value. However, the longitudinal beam oscillation enlarges beam size horizontally, and moreover, accompanies with beam size fluctuation, whose frequency is approximately 200 Hz as seen in Fig. 2.2.1, where

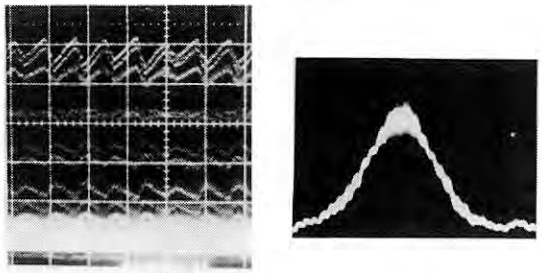

Fig. 2.2.1 Horizontal beam profiles observed with a photo-diode array which detects synchrotron light. Beam size fluctuates correlatively with the longitudinal coupled-bunch instability "758". Sweeping time: (a) 10 ms/division, (b) 10 μs/division.

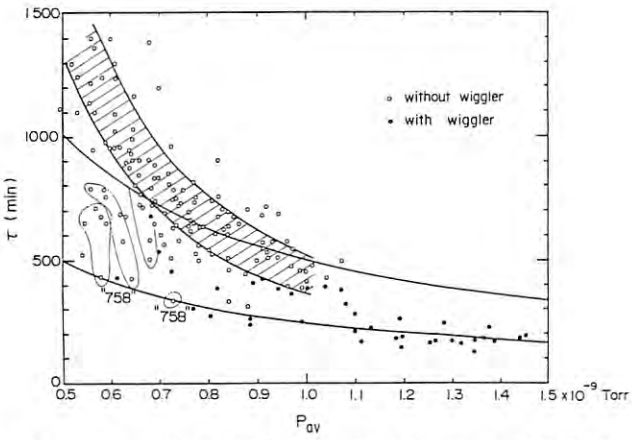

Fig. 2.2.2 Beam lifetime τ(min) as a function of average pressure P_{av} (Torr) in the beam chambers. Open circles represent data with no wiggler operation, and closed ones with wiggler operation. Solid curves show that $P_{av} \cdot \tau$ = constant.

Fig. 2.2.3 Beam profile on the TV beam monitor showing horizontal beam blow-up due to "1070".

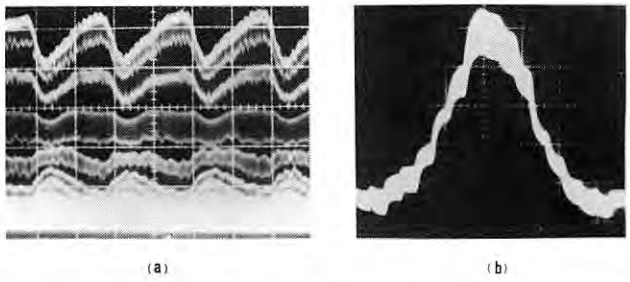

Fig. 2.2.4 Large oscillation of the horizontal beam profile observed with the photo-diode array. This oscillation is caused by the instability "1070". Sweeping time: (a) 10 ms/division, (b) 10 μs/division.

photos were taken with the horizontal profile monitor. When the fluctuation amplitude is large, the beam lifetime decreases. In Fig. 2.2.2, the lifetimes τ (min) of every runs are plotted against the average pressure P_{av} (Torr) in the beam chambers. Runs with the large fluctuation, which are indicated as "758" in the figure, clearly have short lifetime.

(2) The coupled-bunch instability "1070" leads to a destructive beam blow-up horizontally, as seen in Fig. 2.2.3, which is a picture of a TV screen monitoring synchrotron light. The beam profiles indicate the horizontal enlargement of the beam size accompanying with a low frequency fluctuation as seen in Fig. 2.2.4. A lot of trouble is caused by the instability during beam injection and the storage time; e.g., accumulating beam reaches at a certain current, it suddenly drops after a violent beam oscillation.

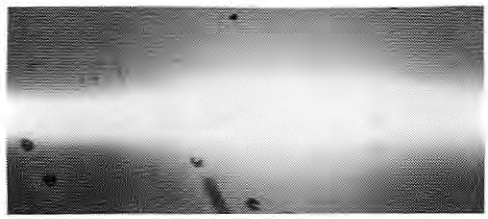

Fig. 2.2.5 TV profile monitor showing beam blow-up due to "830".

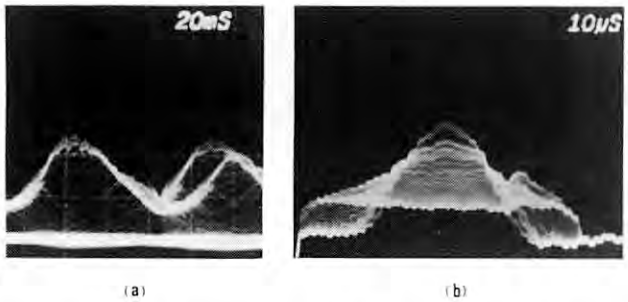

Fig. 2.2.6 Horizontal beam profiles. (a) Horizontal beam blow-up due to "830". (b) Fluctuation of horizontal beam size in 20 ms/division.

(3) The coupled-bunch instability "830" was resently recognized that it is caused by the TM110-like mode of the accelerating cavities. Here the resonant frequency is close to 830 MHz and the transverse coupling impedance is 12 MΩ/m. This instability also enlarges the beam horizontally, and appears to be similar to the instability "1070", as shown in Fig. 2.2.5 for the TV monitor and in Fig. 2.2.6 for the horizontal beam profiles. It also leads to beam loss during injection.

Threshold currents and unstable regions of the coupled-bunch instabilities

Cavity temperature can be given by the values of cavity dissipation power P_c and

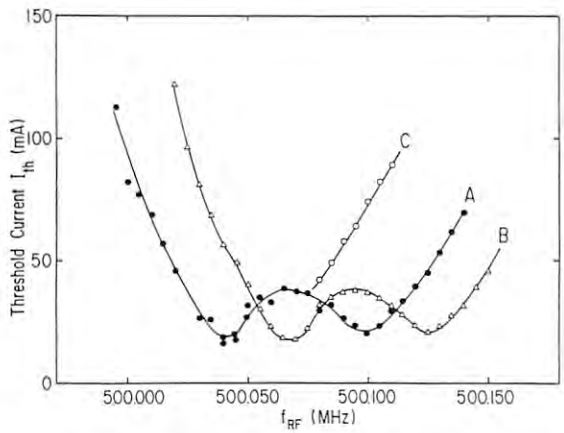

Fig. 2.2.7 Thresholds of the longitudinal coupled-bunch instability "758" as a function of the RF accelerating frequency f_{RF} in the partially filled mode[4]. A, B, and C represent the cavity temperature conditions: A = (T_w, P_c) = (20°C, 116 kW), B = (20°C, 89 kW), and C = (25°C, 116 kW).

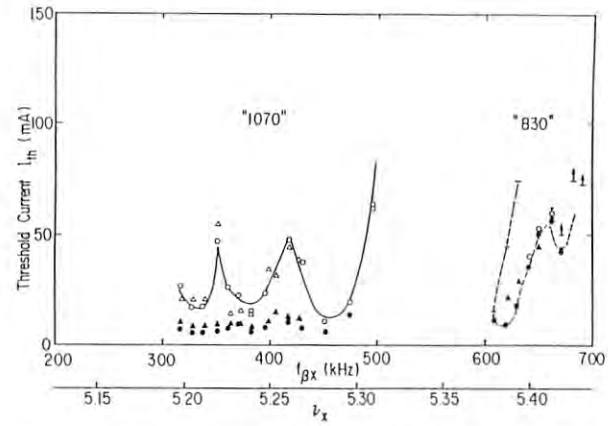

Fig. 2.2.8 Tune dependence of the threshold currents for two horizontal coupled-bunch instabilities "1070" and "830". Here the accelerating frequency was 500.105 MHz. Closed circles and triangles: Threshold currents at which peaks observed on the spectrum analyzer in the uniform and partial filling mode, respectively. Open circles and triangles: Currents at the beam loss began for the uniform and partial filling mode, respectively. Temperature condition was C = (25°C, 116 kW).

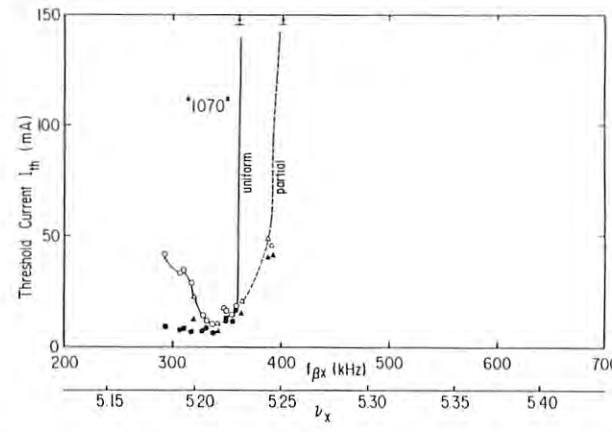

Fig. 2.2.9 Tune dependence of the threshold currents for the horizontal coupled-bunch instabilities at the temperature parameters of (20°C, 116 kW). Marks are all same as given in Fig. 2.2.8 and f_{RF} = 500.110 MHz.

cooling water temperature T_w. The frequency shift of the accelerating mode due to temperature change can be canceled correctly by the tuning plunger. However, the shifts in the frequencies of the higher order mode resonances

cannot be corrected. As a result the unstable regions of the cavity caused instabilities move with the cavity temperature.

Study for the threshold currents by varing the parameters P_c and T_w has been carried out and results are presented in Figs. 2.2.7, 2.2.8 and 2.2.9. Figure 2.2.7 shows the threshold currents I_{th} of the longitudinal instability "758" as a function of the accelerating frequency f_{RF}. Early study of the threshold currents was reported in Ref. 1. This time one of four cavities is new one that was exchanged in May 1984, because a vacuum leak was found on the old cavity at the flange supporting the tuning plunger (see Section 2.3.6). The threshold currents are defined as the beam current at which peaks due to the instability appeared in the beam spectrum.

Figure 2.2.8 shows the thresholds of the transverse coupled-bunch instabilities, "1070" and "830", which were measured by varing the horizontal betatron tune ν_x, at T_w = 25°C and P_c = 116 kW. Here, the threshold currents are plotted on two definitions; one is the same definition of "758" in Fig. 2.2.7 and the other is the beam current at which the beam loss begins during beam injection. Using these data, we plotted the unstable regions with the parameters of P_c and T_w. Figure 2.2.10 shows that of "758" as a function of the accelerating frequency f_{RF}. Unstable regions of "1070" and "830" are presented in Fig. 2.2.11 as a function of the horizontal betatron tune ν_x. For the operation of the vertical wiggler, P_c is set at 116 kW for the quantum lifetime of 4 days. Thus the operating region is on a horizontal line indicated in the figures.

As mentioned previously two transverse instabilities are destructive and should be

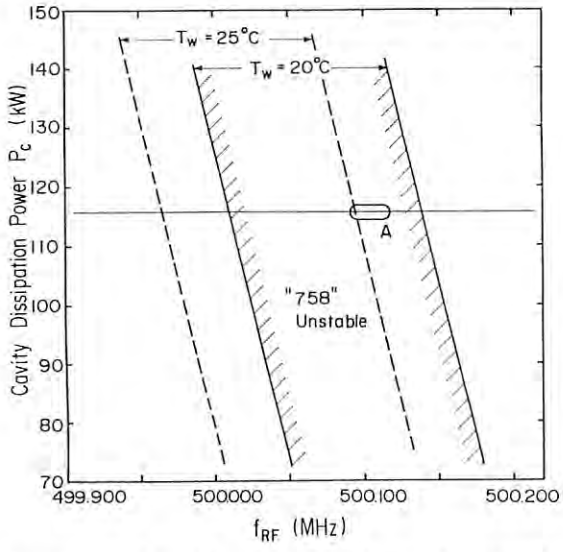

Fig. 2.2.10 Unstable regions of the longitudinal instability "758". Present operating point is indicated as A.

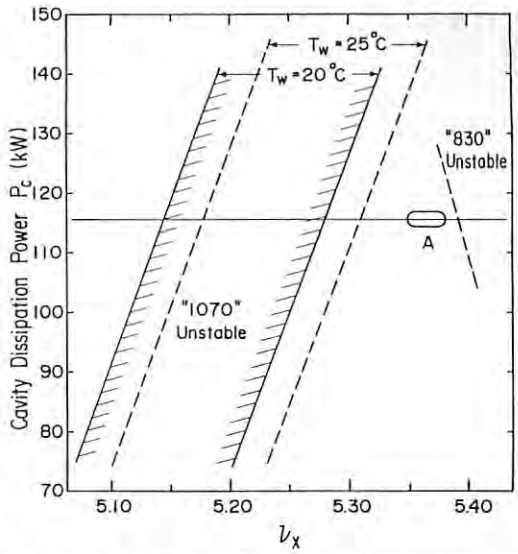

Fig. 2.2.11 Unstable regions of the horizontal instabilities "1070" and "830". Present operating point is indicated as A.

avoided. Present temperature regulation system for the cooling water is limited in the range from 20° to 30°C with errors of ±1°C, and cannot set temperature for each cavity. With this regulation system, operation at higher temperature than 25°C is difficult, because both transverse instabilities come closer to the operating point. Therefore present operating temperature T_w is set at 20°C and the ν_x is chosen to be between 5.35 and 5.38 as indicated as "A" in Fig. 2.2.11. However, the instability "758" cannot be eliminated under this condition as seen in Fig. 2.2.10.

Longitudinal instability "758" and the RF station phase

We have two RF stations in the north and south sides of the storage ring. Each station contains a klystron and two accelerating cavities. Phase difference ϕ_{AB} can be defined as $\phi_{AB} = \phi_B - \phi_A$, where ϕ_A is the phase of the accelerating field of the south station and ϕ_B is that of the north station. Normally, the phase difference should be kept nearly zero. If ϕ_{AB} is given a non-zero value which is not so large, difference of the beam loading power in both stations increases. The cavity dissipation power P_c of each cavity increases or decreases depending on the its phase relation, thus, we can give proper power P_c by adjusting ϕ_{AB}.

Remarkable effect can be seen in Fig. 2.2.12, when applying the phase difference ϕ_{AB} of +18°, beam size fluctuation become large (a). Oppositely if we give ϕ_{AB} as -20°, the fluctuation stops (b). At present this method is employing to reduce the "758" effect.

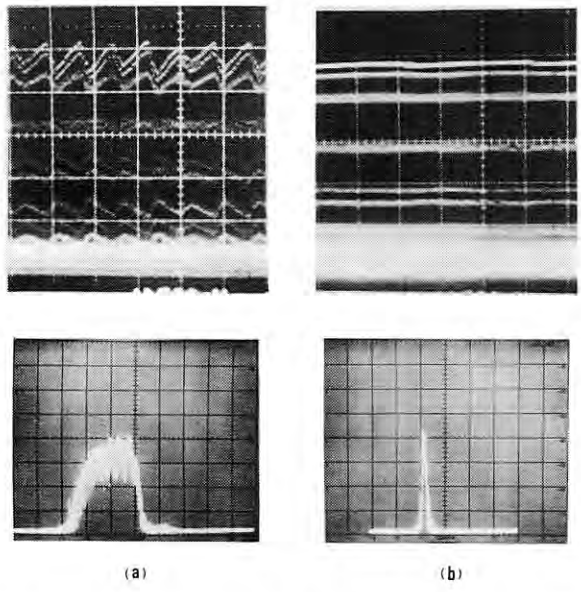

Fig. 2.2.12 Horizontal beam profiles (top) in sweeping time of 10 ms/division and beam spectra of the "758" instability (bottom) in scan width of 2 kHz/division.
(a) Phase difference between two RF stations ϕ_{AB} = +18°. Beam fluctuated violently. Simultaneously broadening of the "758" peak was observed.
(b) Phase difference ϕ_{AB} = -20°. The fluctuation stopped and the peak became sharp.

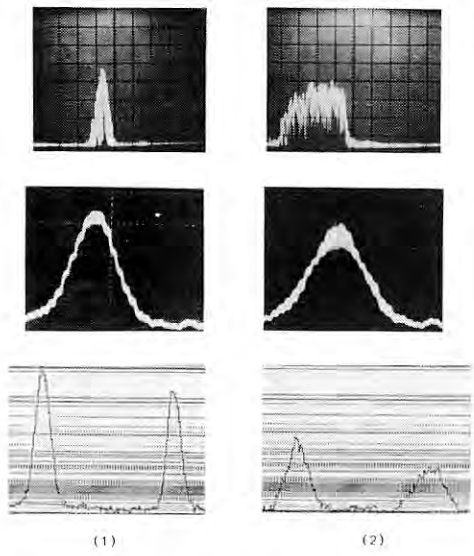

Fig. 2.2.13 The phase ϕ_{AB} was chosen as (1) "758" small and (2) "758" large. From top, the "758" spectra, horizontal beam profiles, and bunch length measured with the streak camera.

Bunch lengthening and widening related to "758"

The longitudinal instability "758", which accompanies with the horizontal beam size fluctuation in approximately 5 msec period, causes a bunch lengthening, and as a result, beam size widening horizontally. This is probably a cause of the short lifetime during the vertical wiggler operation.

The bunch length and the horizontal beam size were measured in relation to the amplitude of "758" with following two sets of ϕ_{AB};
(1) The phase ϕ_{AB} was set at the value for the user runs, in which the effect of "758" can be suppressed fairly, but not completely.
(2) The phase ϕ_{AB} was chosen to be the effect of "758" large.

Figure 2.2.13 shows, from the top, the frequency spectra of the "758" peak, the horizontal beam profiles and the bunch length measured with the streak camera, under both phase conditions (1) and (2), in the left and right, respectively. Where the stored beam current was 150 mA. Bunch lengths and widths of condition (1) are plotted in Fig. 2.2.14 indicating that both enlarge as the "758" fluctuation increases. Below the threshold of "758", observed value of bunch length is 200 ps (FWHM) and calculated natural bunch length is 180 ps. It seems consistent if we taking into account that a resolution and an ambiguity for time measurement are order of 20 ps with the present streak camera system. Horizontal beam size below the threshold was 6.1 mm (FWHM), which is nearly equal to the calculated value. Under the condition (1), the spread of the beam size is approximately 10% at 150 mA. Results of phase condition (2) are plotted in Fig. 2.2.15,

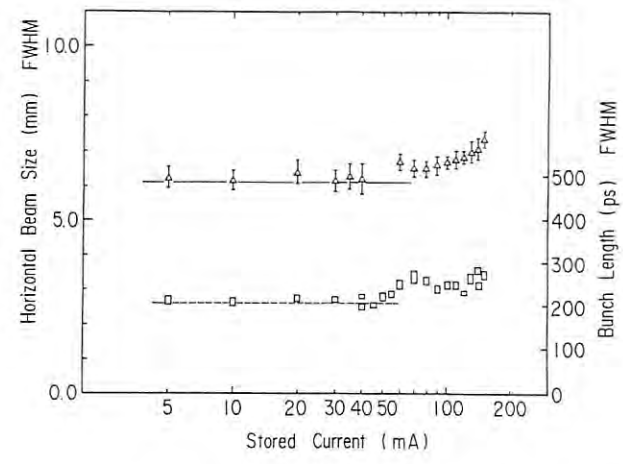

Fig. 2.2.14 Beam size and length for the phase set (1). Triangles: Horizontal beam size (FWHM).
Rectangles: Bunch length (FWHM) measured by the streak camera.

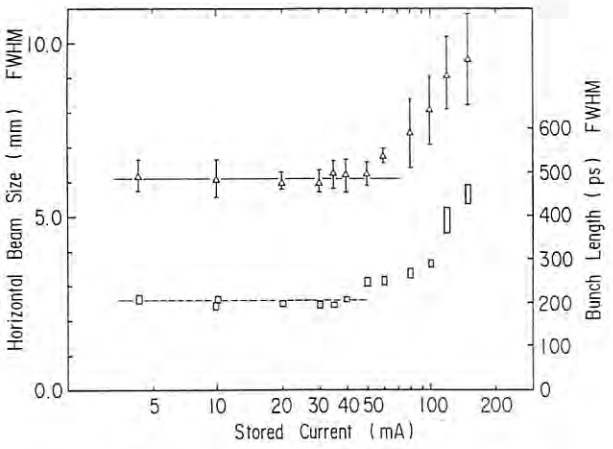

Fig. 2.2.15 Beam size and length for the phase set (2). Marks are all the same as given in Fig. 2.2.14.

showing that the bunch lengthening and widening are largely related to the frequency spread of the "758" peak.

External phase modulation[11] of the accelerating field and "758"

Small external modulation applied on the accelerating field can suppress the beam size fluctuation due to the instability "758". This phenomenon was investigated in a practical point of view. Dependence on the driving frequency f_ϕ of the phase modulation was studied in relation to the properties of the "758" fluctuation. Changes in the horizontal and vertical beam profiles were also studied simultaneously. The phase modulation can be made by giving a bias voltage V_{pp} on a electrical phase shifter that is located right after the master oscillator. This applied voltage modulates the phase of the cavity field, then oscillate the beam longitudinally. The phase modulation causes a phenomenon seen in Fig. 2.2.16, in which the stored current was 147 mA, where the frequency spread of "758" was large (a). When the phase modulation of f_ϕ = 56 kHz, V_{pp} = 80 mV was applied, peak of "758" became small (b), where a peak related to the external force f_ϕ can be also seen. Under this condition, the beam size fluctuation is small. By giving the constant voltage of V_{pp} = 80 mV, stable region was measured as shown in Fig. 2.2.17. Also, observed V_{pp}-dependence is presented in Fig. 2.2.18.

Horizontal beam size is broadened by 20% and effect in vertical size is small when applying the voltage of 80 mV and frequency of 56 kHz. This causes no trouble on lifting up and down of the vertical wiggler system.

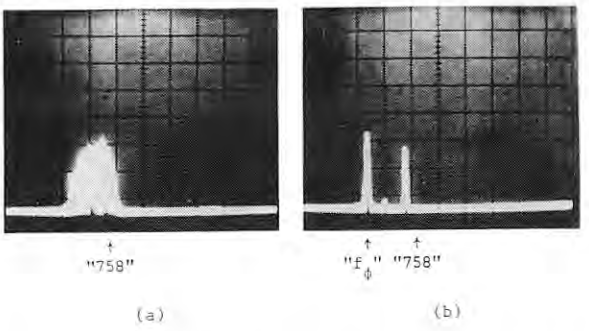

Fig. 2.2.16 External phase modulation can suppress the beam size fluctuation due to "758". (a) Beam spectrum of the "758" peak without external force. Large frequency spread was observed. Scan width: 2 kHz/division. (b) By applying the external phase modulation, beam size fluctuation stopped. V_{pp} = 80 mV and f_ϕ = 56 kHz.

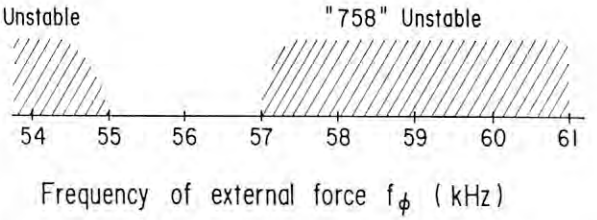

Fig. 2.2.17 Frequencies f_ϕ which can stabilize the beam size fluctuation. Where V_{pp} = 80 mV and stored current was 120 - 100 mA.

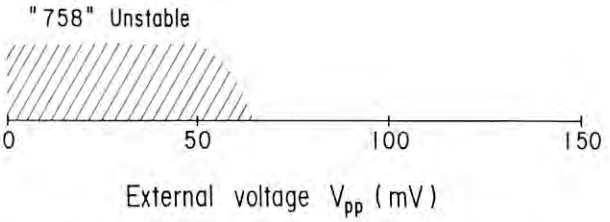

Fig. 2.2.18 Applied voltage V_{pp} and "758" fluctuation at f_ϕ of 56.1 kHz.

Mechanism that the phase modulation suppresses the "758"

It is sometimes observed that the instabilities are suppressed when applying an external forced oscillation whose frequency is close to the natural frequency of the instabilities. Oscillation of "758", as observed above, is suppressed or reduced by the external phase modula-

tion. The frequency of the external force is close to the synchrotron frequency f_s, although having no direct relation to the frequency of "758", which is written as

$$f(758) = 473f_r + f_s \quad .$$

On the other hand, the synchrotron frequency side bands of f_{RF} can be seen although it is very small in the beam spectrum during the storage time. Probably, it is a coherent synchrotron oscillation excited by noises. This side-band peaks of f_s also eliminated by the phase modulation. Figure 2.2.19 presents the phenomenon that the f_s peak seen in (a) eliminated by applying the external voltage of 150 mV and f_ϕ of 55 kHz (b).

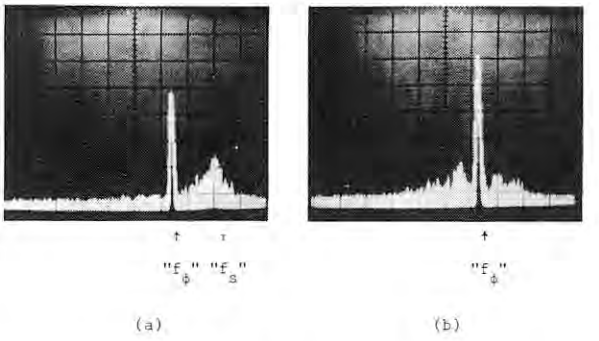

Fig. 2.2.19 (a) Peak of the synchrotron frequency sideband, $f_{RF} + f_s$ = "f_s", can be seen in the beam spectrum (right peak) in scan width of 2 kHz/division. Left peak is due to the external phase modulation (f_ϕ = 55.06 kHz, V_{pp} = 100 mV). (b) Peak "f_s" disappeared when applying V_{pp} = 150 mV.

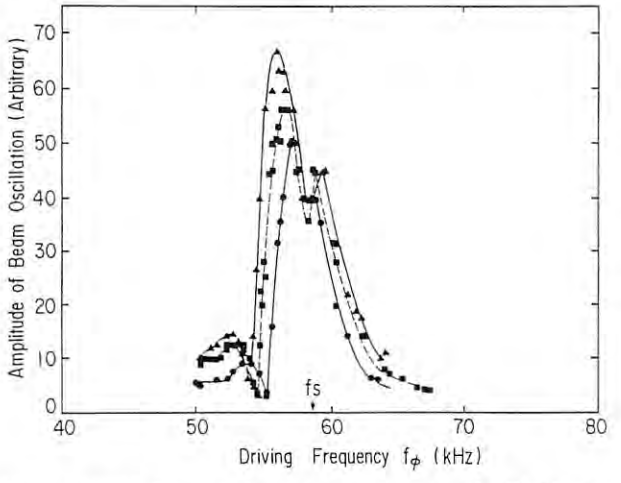

Fig. 2.2.20 Dispersion curves around "f_s" at beam current of 55 mA. Closed circles: V_{pp} = 120 mV. Squares: V_{pp} = 180 mA. Triangles: V_{pp} = 240 mV.

Dispersion curves were measured around the synchrotron frequency side bands. By varing the external frequency f_ϕ, and setting the value of V_{pp} as a parameter, the peak height appeared in the beam spectrum were plotted, as shown in Fig. 2.2.20. Measurements were performed with increasing the value of f_ϕ and then decreasing that. Any hysterisis effect cannot be observed.

Driving frequency at the maximum amplitude is approximately 2 kHz lower than the observed synchrotron frequency of 58.3 kHz. The resonant frequency shift become larger as V_{pp} increases. The left side of the dispersion curves is sharp oppositely the right side is smooth. These phenomena can be explained by taking into account the non-linear terms of the accelerating field. Assuming sine-wave acceleration field, shift in the resonant frequency can be expressed as

$$\frac{\Delta f}{f_s} = \left(\frac{1}{16} + \frac{5}{48}\cot^2\phi_s\right)\omega_{rf}^2 A^2$$

where ϕ_s is the synchronous phase, A the half bunch length in seconds.

On the other hand, bunch lengths were measured using the streak camera, and observed bunch lengths were larger than 200 ps when applying phase modulation. The frequency shift by this bunch length is calculated as

$$\Delta f \cong -2 \text{ kHz}$$

which is explaining the observed frequency shift.

Suppression of "f_s" peak observed in Fig. 2.2.19 can be explained by the tuning phenomenon in the non-linear equation of motion with external forced oscillation. Calculation using van der Pol's equation with driving force shows that as the amplitude of the forced oscillation increases, suddenly "f_s" peak is suppressed. Thus, we can explain the phenomena around the synchrotron frequency side bands. However, suppression mechanism of "758" has not completely been understood yet.

2.2.2 Vertical Instability[5]

Experiments on the vertical instability

The vertical instability observed in the PF storage ring has been considered as an effect of ion-trapping, because there are several indications that the ion effect can explain phenomena concerning about this instability such as tune shifts, tune spreads, increase of beam height, lifetime shortening and so on.

Threshold currents were measured by changing the vertical betatron tune over a wide range. For the simplification, the sextupole magnets were turned off and the measurement was carried out with uniform filling mode. The

result implies that a possible explanation of the mechanism is so-called two-stream instability which is caused by an interaction between the electron beams and trapped-ions. We also found that the vertical instability can be stabilized by exciting the RF knockout field at a frequency within a certain range. Preliminary result will be given together with its plausible explanation.

When the beam profile fluctuates owing to the vertical instability, we always observe peak $f_r - \Delta f_y$ on the spectrum analyzer of RF knockout system, as shown in Fig. 2.2.21, and also on the frequency spectrum of the signals from position monitors. Here f_r and Δf_y are the revolution frequency and the fractional betatron frequency, respectively.

Even if it is difficult to see the fluctuation in the beam profiles because the instability is weak, we still have the peak $f_r - \Delta f_y$. We sometimes observed the other peaks Δf_y, Δf_x, $f_r - \Delta f_x$ near the threshold currents at which a large part of the beam was abruptly lost. After the beam loss, we usually observed an wavelike beam-filling on the current monitor as shown in Fig. 2.2.22. The shapes of the filling depend on the circumstances, but generally we have five or six peaks per revolution or almost double numbers. These observations indicate that the coherent motion of the vertical instability is a dipole motion, although we can not discard a possibility that the coherent quadrupole motion would also be excited, because we do not have any methods for measuring the quadrupole motion.

We measured the dependence of the threshold current on the vertical betatron tune. The working points on which we took data are shown as a hatched region in Fig. 2.2.23. A typical working line in tune diagram is also shown as an arrow. The data are plotted in Fig. 2.2.24 with

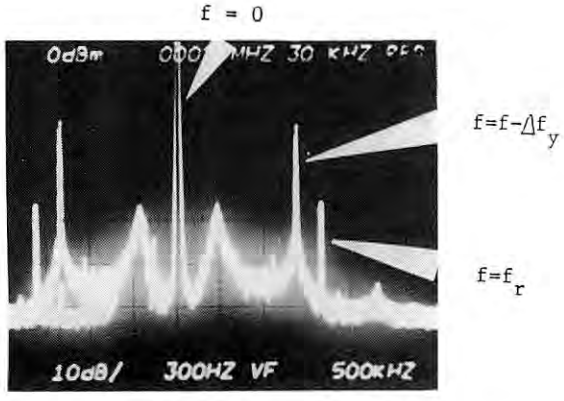

Fig. 2.2.21 Frequency spectrum when the vertical instability was observed.

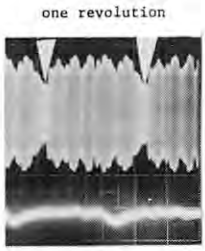

Fig. 2.2.22 A shape of beam-filling after the abrupt beam loss.

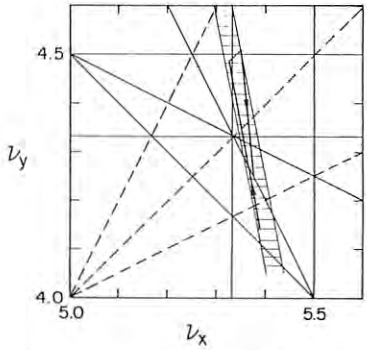

Fig. 2.2.23 The working points where the threshold currents were measured.

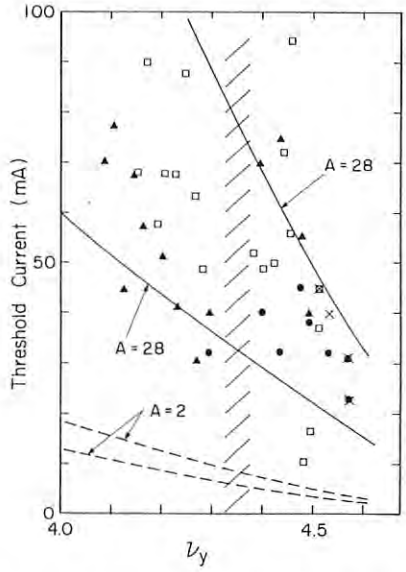

Fig. 2.2.24 Dependence of the threshold currents on the vertical betatron tune. The lines denote the theoretical lower limits of the threshold for the dipole instability: Solid lines are for 100% neutralization and dashed lines for 10% neutralization.

● □ ---Thresholds at injection with kicker being excited.

△ ---Thresholds after injection.

× ---Abrupt loss of a large part of beam.

the theoretical threshold current of the dipole instability, which will be described below.

A differential resonance was excited in the region hatched in Fig. 2.2.24, and the beam became round as we had experienced many times before. We skipped the region because it was difficult to take the data efficiently at the differential resonance point. We also crossed a line of the third resonance. However we encountered no difficulty arising from that the sextupole magnets were turned off.

Stabilization by RF knockout

We found that the vertical instability can be suppressed by exciting RF knockout field. The frequency spectra after the suppression of the instability are shown in Fig. 2.2.25. The driving frequency which can suppress the instability has a wide range of ±100 kHz around 1.2 MHz for the uniform-filling, but for the partial-filling its frequency range is very narrow only a few kHz. The frequency range also depends on the driving power of RF knockout. When an operating point is chosen and a power level is set for RF knockout, the frequency range stabilizing the instability is split into two or three parts for the uniform-filling.

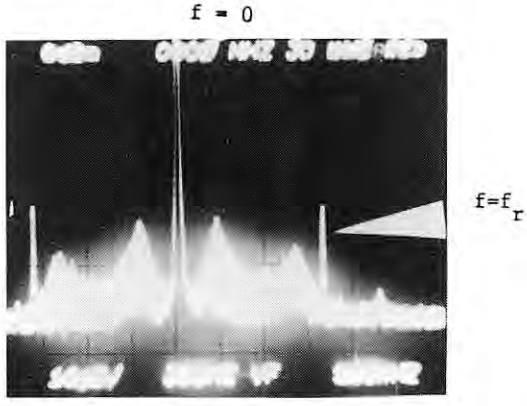

Fig. 2.2.25 Frequency spectrum after the instability was suppressed by the RF knockout.

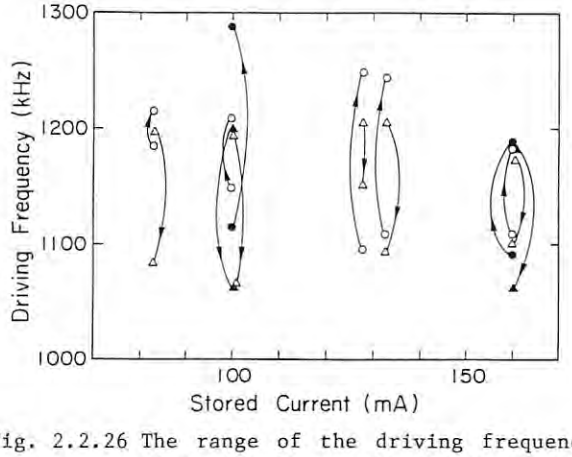

Fig. 2.2.26 The range of the driving frequency of RF knockout that stabilizes the instability. The range is denoted by the line between the marks of circle or triangle, and filled and empty marks have different powers. Here the driving power is relatively low.

Suppression of the instability depends on the direction of changing the driving frequency. Figure 2.2.26 shows hysteresis of stabilization. We also measured the current dependence of the driving frequency that can suppress the instability, and the tune dependence of the frequency. From the preliminary measurement, we could not clearly find their dependence, but it seems that the driving frequency decreases as the vertical tune increases. For the uniform-filling, we sometimes failed to stabilize the instability by using RF knockout only, although we did not try to use sextupole magnets along with RF knockout.

Theoretical interpretation

The single particle behavior and mechanism of ion-trapping are analyzed in Ref. 6, and the critical mass number A_c for the vertical motion is

$$A_c = \frac{N_e}{n}\frac{r_p}{n}\frac{\pi R}{\sigma_y^2(1+\sigma_x/\sigma_y)} \quad , \qquad (1)$$

where N_e is the electron number of beam, r_p the classical radius of proton, R the average radius of storage ring, n the number of bunches and σ_x and σ_y are the beam width and the beam height. The rough estimation of A_c for uniform-filling with 312 bunches gives the order of magnitude 10^{-3} in the PF storage ring even at the beam current of 500 mA. Therefore, according to Eq. 1, any ions can be trapped on the electron orbit.

Since the ionization times at the pressure of 10^{-9} Torr are nearly the same as the repetition rate of the injection, ions tend to neutralize the electron beam.

Keil and Zotter[7] studied the e-p instability in the coasting proton beam where the electrons from ionized molecules are trapped in the electric potential of beam. Their analysis for the coasting beam can be applied to our case of bunched beam.

In the coasting beam approximation, the coherent dipole motions of the electron beam and ion in the vertical direction are give by

$$\ddot{y} + \omega_y^2 y = -\omega_e^2(y-z)$$
$$\ddot{z} = -\omega_i^2(z-y) \qquad (2)$$

where y and z are the vertical position of the center of the electron beam and that of ion, ω_y is the angular frequency of the vertical betatron oscillation, and ω_e and ω_i are

$$\omega_e^2 = \frac{2\rho_i r_e c^2}{\gamma} \frac{1}{q(p+q)} \quad ,$$

and

$$\omega_i^2 = \frac{2\rho_e r_p c^2}{A} \frac{1}{b(a+b)}$$

with ρ_i, ρ_e the ion and electron numbers per unit length, γ the Lorentz factor, r_e the classical radius of electron, A the mass number, p and q the rms width and height of ion, and a and b the rms width and height of electron beam, respectively. Assuming the density of ion to be uniform, we have from Eq. 2,

$$(\Omega^2-\nu_i^2)\left[(\Omega-m)^2 - (\nu_y^2+\nu_e^2)\right] - \nu_e^2\nu_i^2 = 0$$

where ν_y is ω_y/ω_r and ν_i is ω_i/ω_r with ω_r the angular revolution frequency, m the mode number and Ω the eigen-frequency corresponding to m. The coherent quadrupole instability caused by ion-trapping can be analyzed in almost the same method as the dipole case.

The analysis shows that the most dangerous mode number for the dipole instability is the nearest integer above the tune ν_y that is m = 5 for the present operation, and for the quadrupole instability the nearest integer above $2\nu_y$ that is m = 9. It also shows that the frequency of the dipole oscillation excited by the instability is near $(m - \nu_y)\omega_r$ when measured at a certain location in the storage ring.

It should be noted that the magnetic field in bending magnets and the electric field induced by the beam tend to remove ions from the bending magnets by the effect of drift velocity. This effect and the different densities of neutral molecules along the ring cause the ion density to vary at the location. It should be also noted that the coherent quadrupole motion is disturbed in the bending magnets due to the cyclotron motion, the effect of which is not included in the calculations of Fig. 2.2.24.

There are several subjects and questions about the vertical instability: (1) The effect of sextupole magnets should be studied in detail. (2) The Landau damping and the nonlinear effects would play an important role. (3) Neutral molecules may give an effect on the motion of ions specifically at higher vacuum pressure. (4) The interactions between different kinds of ions and their influence on the electron motion should be included in the calculations. (5) The quadrupole component in the field produced by RF knockout would play a role in the suppression.

2.2.3 Synchrotron Sidebands in Betatron Oscillation[8]

The betatron sidebands in the PF storage ring were observed by use of the RF knockout system, which had earlier been introduced for the measurement of tune parameters. By exciting the beam with transverse magnetic field, we observed transverse beam oscillations with a quadrature photodiode[9] which detected the synchrotron light from the beam. The photodiode signal was fed to a spectrum analyzer to obtain the frequency distribution. Both incoherent and coherent longitudinal oscillations were distinguished in the distribution and their amplitudes were compared with theoretical predictions. Also their chromaticity dependence was obtained to test the theoretical model.

Theoretical foundation on the subject is given in a paper by D.E.P. Mohl and P.L. Morton[10]. They indicate that it should be possible experimentally to obtain both incoherent and coherent longitudinal oscillation frequencies by measuring the coherent transverse oscillation response.

Three kinds of measurements were made. First, the beam was excited at betatron frequencies f_x, f_y and their sidebands stepped by $\pm nf_s$. Second, their chromaticity dependence was observed at $f_y \pm f_s$ by changing the current of the defocusing sextupole magnets. Third, there are such cases that the main peak is enhanced more strongly than the sideband at a new driving frequency differing only by a few kHz from that used in the first measurement made above. This is the case when the longitudinal phase oscillation is coherent.

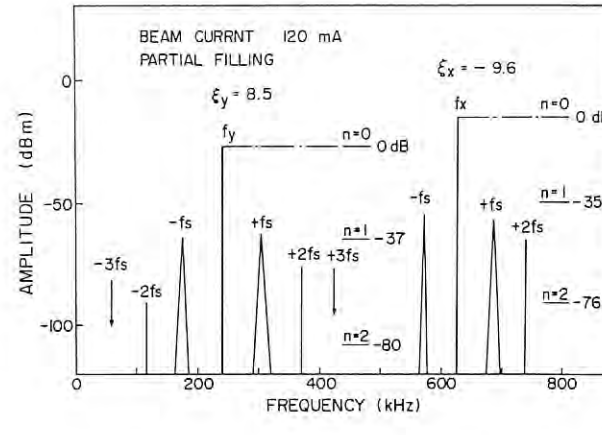

Fig. 2.2.27 Synchrotron sidebands of f_x and f_y taken with beam current of 120 mA. Theoretical values are shown with horizontal broken lines for mode n. Broad peaks are shown in triangular shape to indicate their widths.

Betatron sidebands due to incoherent longitudinal oscillation

The data are taken for different current values with both uniform and partial fillings of RF buckets[4]. Figure 2.2.27 shows a spectrum for sidebands obtained with beam partially filled and its current of 120 mA. For f_x, peaks are seen clearly at $\pm f_s$ and $+2f_s$ but the peak at $-2f_s$ seems to be hidden in the background hill. For f_y, sidebands up to $\pm 2f_s$ are clearly seen. But they barely stick out of the background at $\pm 3f_s$. Only their upper limits are shown with arrows.

Theoretical values of spectrum strengths are also shown in dB with respect to the main peak with the mode number attached. Assuming the momentum distribution to be Gaussian with $\sigma_\varepsilon/E = (\Delta p/p)$ r.m.s., the ratio of the n-th amplitude to the fundamental peak (n = 0) is given by

$$\frac{|\langle x(n)\rangle|}{|\langle x(o)\rangle|} = \frac{1}{2^n n!}\left(\frac{\xi}{\nu_{si}}\frac{\sigma_\varepsilon}{E}\right)^{2n}$$

for $\xi\sigma_\varepsilon/\nu_{si}E \ll 1$, with $\nu_{si} = f_s$ (incoherent)$/f_r$ and chromaticity $\xi = \Delta\nu/(\Delta p/p)$.

Chromaticity dependence

To test the theoretical model, the strength of first sidebands were measured for different values of chromaticity. Figure 2.2.28 shows the amplitudes of first vertical sidebands $f_y \pm f_s$ when the chromaticity ξ_y was changed. Theoretical values are shown with solid lines. The amplitude of $f_y \pm f_s$ are normalized to the amplitude of the main peak.

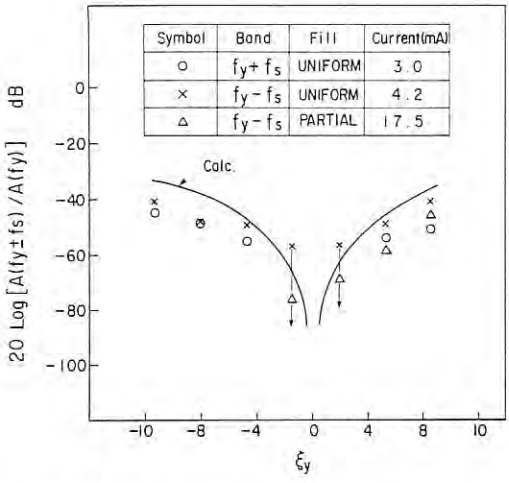

Fig. 2.2.28 Chromaticity dependence of sidebands $f_y \pm f_s$ taken with uniform or partial beam filling. Theoretical values are shown with solid curves.

Betatron Sidebands Due to Coherent Longitudinal Oscillation

According to the theoretical consideration, it is predicted there exists sideband frequencies which enchance the main peak higher than the sidebands at the driving frequency. For driving frequency $f_d = f_\beta + nf_s$ (coherent), the fundamental mode will dominate

$$\frac{|\langle x(n)\rangle|_n}{|\langle x(n)\rangle|_o} = \frac{1}{n!}\left(\frac{\xi B}{2\nu_{sc}}\right)^n$$

for $\xi B \ll \nu_{sc}$, with $\nu_{sc} = f_s$ (coherent)$/f_r$ and B the amplitude of coherent synchrotron motion. Searching carefully near the sidebands, we found that the main peak pronounced higher than the sidebands at frequencies differing by a few kHz from that of the incoherent case. Table below summarizes these cases. Mode number n in Column 1 indicates the driving frequency is set at $f_d = f_\beta + nf_s$ for n = 1,2 and the chromaticity $\xi_y = 8.5$. Two kinds of spectrum amplitudes are taken at frequencies $f = f_\beta$ and $f_\beta \pm nf_s$ and given as R(f) in Column 2 and 3. All the amplitudes (in dB) are normalized to the amplitude of the main peak taken with the driving frequency at $f_d = f_\beta$.

Data are also taken with RF phase modulation turned on. The RF phase was modulated with a 56 kHz cw source[11]. Results are listed in the table with symbol * to compare with data without the phase modulation.

Assuming the amplitude normalized to σ_ε/E, 1.5 ∿ 2.0, theoretical predictions are also added to the table. They lie near to the experimental results.

Mode No.		$R(f_y)$dB	$R(f_y \pm nf_s)$dB
n=1	Cal.	-18 ∿ -48	-36 ∿ -76
	Exp. *	-23	-37
	Exp.	-44	-51
n=2	Cal.	-42 ∿ -77	-84 ∿ -154
	Exp.	-33	-57

2.2.4 Operation of a Streak Camera System

A streak camera was installed for the observation of bunch structure in the storage ring. The Model C979 camera of Hamamatsu photonics Co. has time resolution of 10 ps and repetition rate of 1 kHz. It was added to the optical observation system of synchrotron light which has been working for monitoring beam qualities such as profiles, lateral oscillations and position. The layout of the optical system was given in the previous report. Minor modification was necessary for this experiment as described below.

Optical system

The synchrotron light is extracted from the storage ring with a water-cooled mirror placed in the vacuum duct and is driven down to a dark room. The light reaching there is first focused with a telescope and is split into five channeles for different purposes. The streak camera has its own channel composed of a series of lenses and mirrors so that the beam image is aligned lengthwise along a narrow slit of which width decides the time resolution (slit of 30-100 μm was used here). Especially when the amount of light output is small such as in multibunch mode, it is crucial to make light input to the slit as intense as possible in order to obtain the streak image in good photon statistics.

Triggering circuit

Figure 2.2.29 illustrates the streak camera system including a streak tube with its controller and analyzer and a series of triggering circuits. Streak triggering is controlled with its gate circuit which prohibits the camera from receiving unnecessary light input because the light signal is a pulse train spaced by 2 ns or 600 ns, depending on either multibunch or single-bunch mode of the storage ring. The gate circuit not only reduces background on the MCP due to the continuous lighting but also avoids double exposure due to the backward sweep voltage after a shot. The circuit also prevents the camera from running at more than 1 kHz repetition rate for securing its recovery time.

The triggering signal is prepared as shown in the figure where pulse shapes are drawn in for later reference. The first circuit, DRIVE 500/312 counts down 500 MHz RF signal to produce a pulse per every 312 bunches and gives a delay between input and output. The succeeding pulse generator produces a masking pulse with a delay with respect to its input signal. The TTL AND-GATE next to it transfers only the bunch pulse covered within the masking pulse. The following line driver makes the pulse height suitable to the trigger input of the next pulse generator. The timing between gate and streak sweep is readily controlled within the gate option and temporaldisperser provided by the manufacturer.

Figure 2.2.30 shows a timing chart. Proper timing is required only between RF signal and streak trigger by adjusting the delay in DRIVE 500/312 circuit. If to select n-th bunch with respect to the first, it is also necessary to change the delay of MASK signal more than n × 2 nsec to get there.

Data collection

Streak images are analyzed with the Model C1018 analyzer which provides data in the form of light intensity vs time, either in a histo-

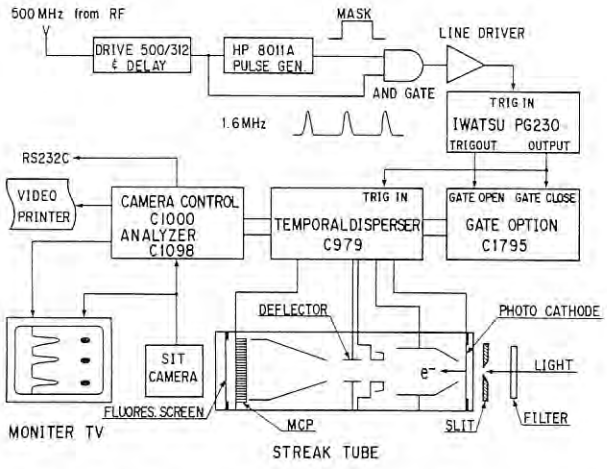

Fig. 2.2.29 Streak camera system composed of the trigger/gate circuits and the controller and analyzer.

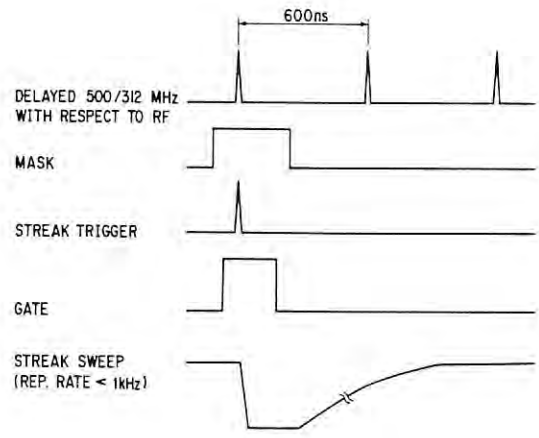

Fig. 2.2.30 Timing chart of the streak camera system.

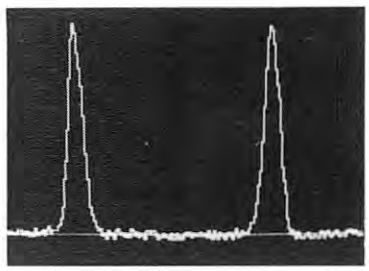

Fig. 2.2.31 Two bunches spaced by 2 ns taken with stable beam. The coordinate axes are for time vs. intensity in 256-channel, digital scale. FWHM ∿ 180 ps.

gram on CRT or in a set of 256 8-bit intensity signals corresponding to the channels on time axis. In this experiment, histogram data are collected in the form of video printer output and are analyzed with an off-line digitizer for obtaining bunch length and other information. All the histogram below were taken with single shot instead of multiple shot of the analyzer to eliminate the triggering jitters in the measurement of bunch length even though the photon statistics becomes poorer.

The bunch length were measured under various beam conditions. Figure 2.2.31 shows a histogram of two successive bunches with stable beam. Figure 2.2.32 gives a set of pictures taken in partial filling mode of the beam storing while RF phase modulation was off for the first picture and on for the second. Figure 2.2.33 is another set taken in single bunch mode without and with the modulation. One can

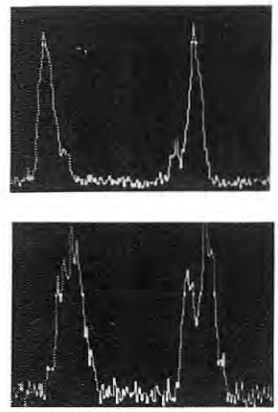

(a) V_{pp} = 0 mV

(b) V_{pp} = 150 mV

Fig. 2.2.32 Bunch structures taken with beam partially filling the storage ring. The f_s values indicate levels of the RF phase modulation.

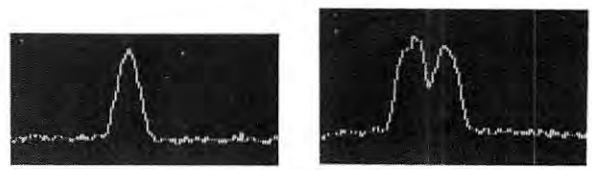

(a) V_{pp} = 0 mV (b) V_{pp} = 150 mV

Fig. 2.2.33 Bunch structures taken with single bunch beam.

clearly observe in these pictures that the bunch shape is widened or double-peaked when the phase modulation is turned on.

The results on bunch length are given in Section 2.2.1 of this issue, which prove that the measured bunch length agreed reasonably well with the calculated value.

Conclusions

The streak camera system has been useful to study the bunch structures of beam. The agreement between measured and calculated bunch lengths also demonstrates indirectly that the camera has a time resolution close to that given in the catalog . It is, however, necessary to make a calibration with an independent well-defined light source for more precise evaluation.

One perplexing problem now resides in the camera system. When two to three bunches are covered in a single frame, the peak height often varies from bunch to bunch as great as 50%. It is not yet clear whether this is due to either electronics problem or statistical reason or fluctuations of the beam itself. Further study is awaited on this problem.

The analyzer system will soon be connected through its RS232C port to a personal computer for more efficient data-taking.

References

1. Y. Yamazaki, H. Kobayakawa, Y. Kamiya and M. Kihara: KEK Report KEK-83-3, 1983 and KEK Report KEK-83-7, 1983.
2. Photon Factory Activity Report 1982/83, p.IV-37.
3. H. Kobayakawa, M. Izawa, Y. Kamiya, M. Kihara and Y. Yamazaki: Proc. 5th Symp. Accel. Sci. Tech., 1984, p.289.
4. Y. Yamazaki, M. Kihara and H. Kobayakawa: KEK Report KEK-83-17, 1983.
5. Y. Kamiya, M. Izawa, T. Katsura, M. Kihara, H. Kobayakawa and S. Shibata: Proc. 5th Symp. Accel. Sci. Tech., 1984, p.292.
6. Y. Baconnier and G. Brianti: CERN/SPS/80-2 (DI).
7. E. Keil and B. Zotter: CERN-ISR-TH/71-58, 1971.
   H. Hereward: CERN 71-15, 1971.
8. T. Katsura, Y. Kamiya and S. Shibata: Proc. 5th Symp. Accel. Sci. Tech., 1984, p.286.
9. Photon Factory Activity Report 1982/83, p.IV-25.
10. D.E.P. Mohl and P.L. Morton: PEP-68, 1973 PEP Summer Study (1974).
11. H. Kobayakawa, Y. Yamazaki and Y. Kamiya: KEK Report, KEK-83-8, 1983.

2.3 VACUUM

2.3.1 General Description

The improvement of the beam lifetime performance is a main objective in the electron storage ring dedicated to synchrotron radiation sources because a stable intensity of synchrotron radiation (SR) is necessary for carrying out optical experiments, and the lifetime above 10 hrs is usually required. It is well-known that the minimum pressure in a normal electron storage ring with a relatively large aperture of the vacuum chamber is aimed at the lower range of 10^{-9} Torr. However, in the case of the ring designed to have a large number of insertion devices[1] called wiggler or undulator with a low-emittance beam, the situation for the vacuum system is different. The low-emittance beam promises a high brightness of the radiation from the insertion devices as well as a long quantum lifetime even with a small aperture, which is desirable for them to operate with a narrow gap height. On the other hand, the lifetime associated with the scattering by residual gases is not made longer by reducing the emittance and depends strongly upon the width of the aperture. Thus, the pressure in such a special ring with a small aperture should be reduced to the lower range of 10^{-10} Torr being much lower than that in a conventional SR source.

Although the design of the PF ring is rather conventional compared to the latest proposals of new SR sources[2,3,4], it has 6 straight sections available for insertion devices, and at present two of them are occupied by the undulator[5] and the wiggler[6] (so-called wavelength shifter). In the case of the undulator, the vertical aperture is limited within 18 mm while the minimum vertical aperture of the normal ducts is 53 mm. Furthermore, the construction of a new insertion device with a gap height less than 10 mm is proposed. It is well-known that the beam lifetime depends upon the width of aperture and there are two kinds of the beam decay process related to the aperture limit. One originates in the single scattering by residual gases, the other in the synchrotron radiation where the stored electrons emit photons according to quantum mechanics[7]. Then, the lifetime determined from the latter process is called quantum lifetime which can be longer by reducing beam emittances. The quantum lifetime with respect to the vertical aperture limit is given by

$$\tau_q = \frac{\tau_y \exp(\xi_y)}{2\xi_y} \quad , \quad \xi_y = \frac{D_y^2}{2\varepsilon_y \beta_{yo}} \quad ,$$

where τ_y is the damping time of vertical betatron oscillation, Dy the width of the narrowest half aperture in the ring, ε_y the vertical emittance, and β_{yo} the value of vertical betatron function at the location of the narrowest aperture. The lifetime related to the pressure of the residual gases is given by[8]

Table 2.3.1
Beam parameters of the ring related to the lifetime.
The emittance coupling between horizontal and vertical directions is assumed to be 10%.

		Medium-emittance optic (currently used)	Low-emittance optics (in future)
Horizontal emittance	ε_x (m·rad)	4.9×10^{-7}	1.6×10^{-7}
Vertical emittance	ε_y (m·rad)	4.9×10^{-8}	1.6×10^{-8}
Horizontal damping time	τ_x (msec)	9.1	8.3
Vertical damping time	τ_y (msec)	7.8	7.8
Narrowest half aperture in the vertical direction	Dy (mm)	9	< 5
Vertical betatron function at the location of the narrowest aperture	β_{y0} (m/rad)	12.7	12.0
Mean value of vertical betatron function	$\langle\beta_y\rangle$ (m/rad)	7.0	9.2
Bucket height in a rest mass unit	γ_c	29	45
Beam energy in a rest mass unit	γ	4890	4890

$$\tau_R = 9.5\times10^{-28} \sum_i P_i(\text{Torr}) \{\frac{2\pi r_o^2 Z_i}{\gamma} + \frac{4\pi<\beta_y>\beta_{yo}}{D_y^2}(\frac{r_o Z_i}{\gamma})^2 + 4\alpha r_o^2 Z_i(Z_i+1)(\frac{4}{3}\log\frac{\gamma}{\gamma_c} - \frac{5}{6})\log(183 Z_i^{-\frac{1}{3}})\}^{-1} ,$$

where P_i is the partial pressure of the atom with an atomic number of Z_i, r_0 the classical electron radius in cm, α the fine structure constant, $<\beta_y>$ the mean value of the vertical betatron function, γ the electron energy in a rest mass unit, and γ_c the rf bucket height. If the Touschek lifetime was neglected, we obtain the total lifetime as

$$\tau_T = (\tau_q^{-1} + \tau_R^{-1})^{-1} .$$

The ring is operated now in the medium-emittance optics[9] with the horizontal and vertical emittances of $\varepsilon_x = 5 \times 10^{-7}$ m·rad and $\varepsilon_y = 5 \times 10^{-8}$ m·rad, respectively. However, the lower emittance operation will be possible in near future by the reinforcement of the power supplies for the quadrupole magnets. Table 2.3.1 shows the beam parameters related to the lifetime for both optics. The total lifetime, τ_T was obtained from the above equations by using the numerical values given in Table 2.3.1. As a result, Fig. 2.3.1 shows the dependence of τ_T for the medium-emittance optics currently used upon the atomic number, calculated on the assumption that the residual gases of 1×10^{-9} Torr were formed of simple substances of one species. Furthermore, assuming that the residual gases were composed of 100% CO, the dependences of τ_T at various pressures upon the width of half aperture, D_y are calculated in Fig. 2.3.2 where the full and broken curves represent the lifetimes derived from the medium and low-emittance optics, respectively. As shown in Fig. 2.3.2, the minimum value of D_y required to obtain the lifetime above 20 hrs at the pressure of 1×10^{-9} Torr is 9 mm, the same value for both optics, but if the pressure is reduced to 2×10^{-10} Torr, the attainable minimum value of D_y may be 5.5 mm for the medium-emittance optics or 3 mm for the low-emittance optics. The above results show that the aperture can be minimized by lowering the pressure and that if the system was kept at high pressures, the low-emittance property would have little effect on that purpose. Hence, the improvements with respect to the vacuum abilities in the PF ring become so important that the insertion devices with a narrow gap height may be operated well in the low-emittance optics. For that purpose, we adopted argon glow discharge cleaning (ArGDC) aimed at the reduction of photo-desorption[10] as well as increased the total pumping speed by introducing many Ti-sublimation pumps in September 1982.

In the present report, we describe the recent performances of the vacuum system and some problems encountered during its operation.

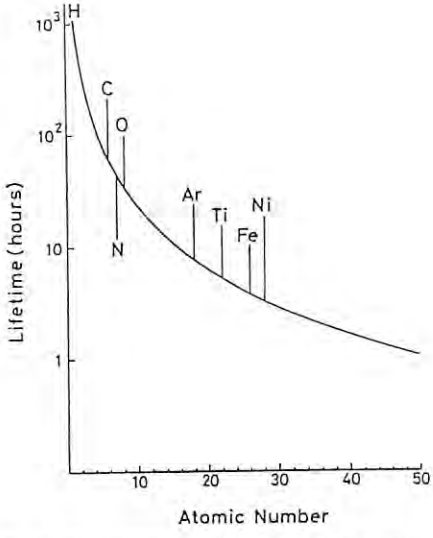

Fig. 2.3.1 Dependence of the lifetime. τ_T for the medium-emittance optics upon the atomic number. The calculation is made on the assumption that the residual gases of 1×10^{-9} Torr were formed of simple substances of one species.

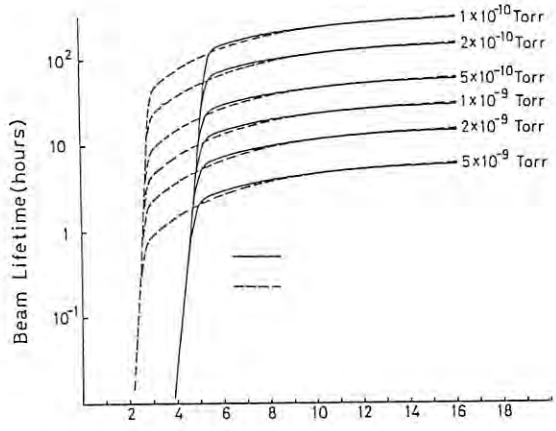

Fig. 2.3.2 Dependence of the lifetime. τ_T at various pressures upon the width of half aperture, Dy. The calculation is made on the assumption that the residual gases were composed of 100% CO. The full and broken curves represent lifetimes derived from the medium and low-emittance optics, respectively.

2.3.2 Vacuum System of the PF Ring

The total pumping speed of the vacuum system of the PF ring, which had been 1×10^4 ℓ/s prepared in the initial design of the system, was increased up to 3.6×10^4 ℓ/s by introducing many Ti-sublimation pumps in September 1982 just before ArGDC. Figure 2.3.3 shows the schematic illustration of the present vacuum system. The vacuum ducts forming the system with a circumference of 187 m are made of aluminum alloy (6063T) and 304 stainless steel[11]. As shown in Fig. 2.3.3, 55 pumping ports are distributed in the system and each of them, except for a few cases, is provided with a combination of a 128 ℓ/s sputter-ion pump and a Ti-sublimation pump. The typical effective pumping speed per port is estimated to be about 600 ℓ/s. Furthermore, 28 sets of distributed-ion pumps with a pumping speed higher than 150 ℓ/s per each are located in the bending sections, B01-B28. The rough pumping is carried out by 6 turbo-molecular pumps. At present, 9 gate valves (VAT 10-100H) with viton seals are used, but, due to the reason as described later, they will be exchanged for all-metal valves with rf shields in September 1985. The system for measuring the pressure consists of 48 BA gauges and 3 quadrupole mass analyzers. The data obtained by the BA gauges are monitored by CRT placed in the control room. Figure 2.3.4 shows the example of the CRT display. The abscissa represents the BA-gauge number as denoted in Fig. 2.3.3.

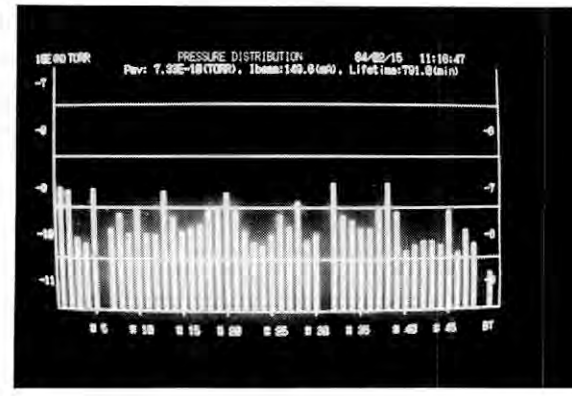

Fig. 2.3.4 Example of the CRT display giving the status of the vacuum system.

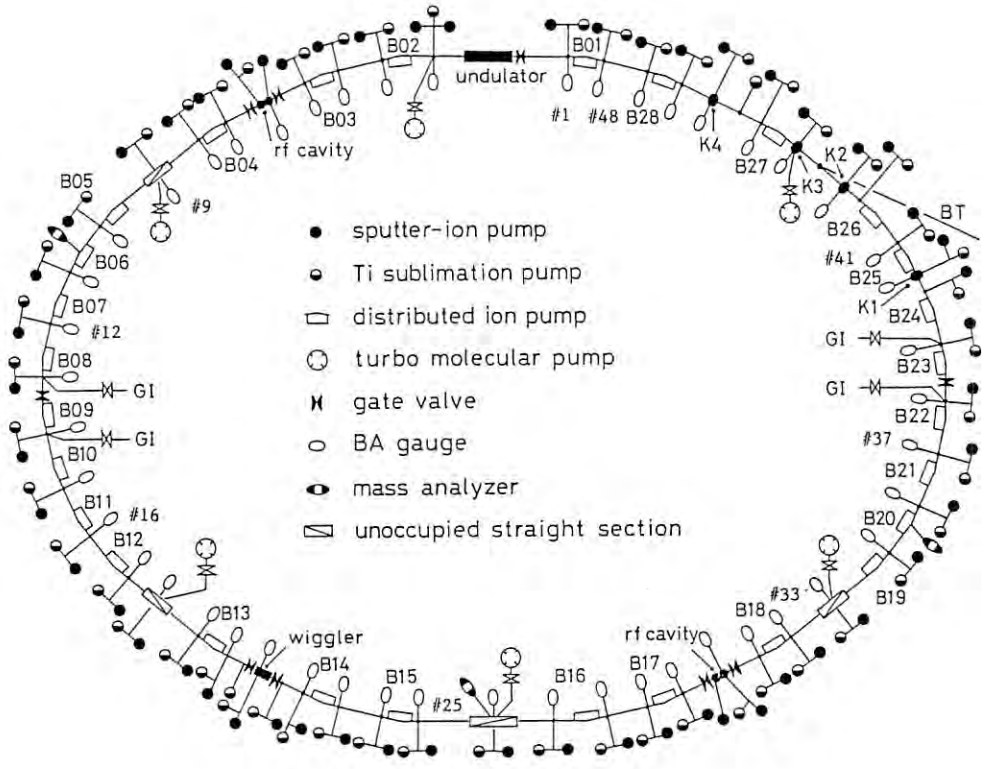

Fig. 2.3.3 Schematic illustration of the vacuum system.

2.3.3 Recent Performance of the Vacuum System

Figure 2.3.5 shows the dependences of the pressure, P_{100} averaged in the ring and the beam lifetime, τ_{100} for the beam current of 100 mA upon the amount of the time-integrated beam current from the beginning. Although P_{100} decreased gradually down to 1×10^{-7} Torr with τ_{100} = 0.5 hr before September 1982, it was found to be reduced rapidly by making the ArGDC as well as introducing many Ti-sublimation pumps (TSPs), and by an additional self-cleaning of 70 Ahrs, P_{100} and τ_{100} was obtained as 6×10^{-10} Torr and 700 mins, respectively. By the way, P_{100} obtained around 130 Ahrs seems to reach a plateau, but this is thought to originate in the drop of the total pumping speed because 40% of

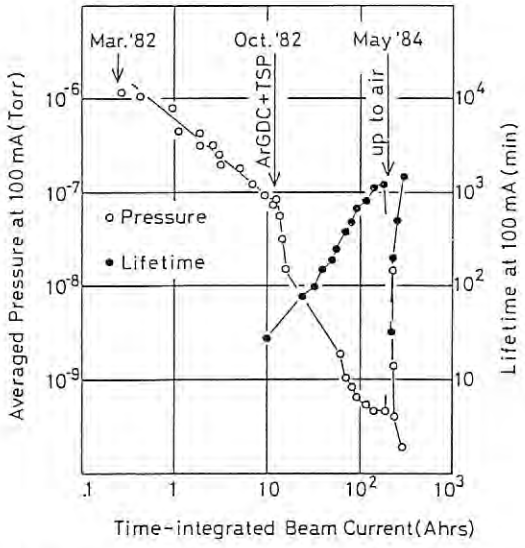

Fig. 2.3.5 Dependences of the pressure averaged in the ring and the beam lifetime at the beam current of 100 mA upon the amount of the time-integrated beam current from the beginning.

the TSPs had broken down due to the snapping of a filament.

In March 1984, the half of the vacuum system was filled with air by an accidental leak from one of the beam lines. The reason why the accident became so fatal is considered to be due to the scheduled electricity stopage which was made previously for 10 hrs with the pressure of the compressed air for driving the pneumatic valves being lowered as well as the operation of the interlock system for controlling the beam lines being stopped. In May 1984, the whole vacuum system of the ring was exposed to air for maintenance with all the broken TSPs being repaired. The system was evacuated again down to the base pressure of 2.5×10^{-11} Torr with a bakeout of 48 hrs but without further ArGDC. Although P_{100} went up to 2.5×10^{-8} Torr with τ_{100} = 30 mins in the first operation of the ring after the last evacuation, the vacuum system was completely restored with $P_{100} = 3 \times 10^{-10}$ Torr and τ_{100} = 1500 mins. The best operation of the ring, obtained recently, is shown in Fig. 2.3.6. The abscissa represents the time elapsed since the end of the beam-stacking. The ordinate represents the beam current by a full curve, the pressure by a chained curve, or the lifetime by a dotted curve.

From the results obtained so far, we concluded with the following. (1) The ArGDC in the PF ring as well as the increase of the pumping speed made the self-cleaning apparently more effective. (2) Even if the vacuum system, being cleaned with a low rate of the photo-desorption, would be filled with air, it can be restored to the original state by a little amount of self-cleaning without an additional ArGDC.

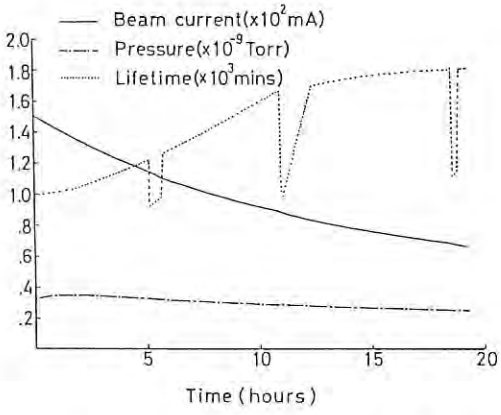

Fig. 2.3.6 The best operation of PF obtained recently. The abscissa represents the time elapsed since the end of the beam-stacking. The ordinate represents the beam current by a full curve, the pressure by a chained curve or the beam lifetime by a dotted curve.

2.3.4 Sudden Decay of the Beam Lifetime

We frequently observed a sudden decay of the beam lifetime during the storage of the beam in the PF ring[12]. In the worst case, the lifetime showed a conspicuous decrease from several hundred minutes to a few minutes. The typical example is shown in Fig. 2.3.7. The abscissa or ordinate represents the same as described for Fig. 2.3.6. As shown in Fig. 2.3.7, after 2 hours, the lifetime is found to fall suddenly from 1000 to 100 minutes, while the corresponding pressure did not increase but decreased gradually according to the decay of the beam current. The above phenomenon is thought to

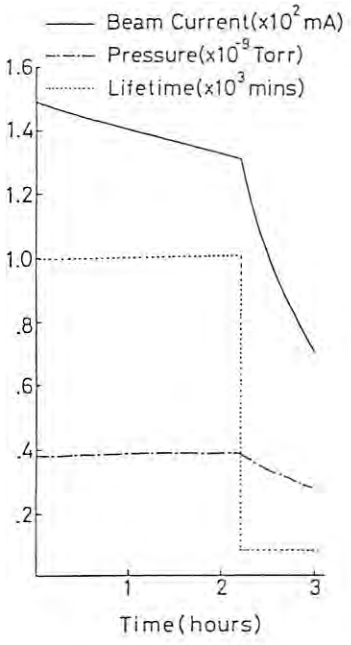

Fig. 2.3.7 Example of the sudden beam decay. The abscissa or ordinate represents the same as described for Fig. 2.3.6.

have no relation with the beam instabilities with respect to the rf operation etc. because no obvious change in the beam profiles was observed when the sudden beam decay occurred. Furthermore, we also obtained other results related to this phenomenon as described in the following; (1) The frequency of the sudden beam decay was made much lower by applying a negative voltage of 400 V to the stainless steel wire stretched in front of the DIP, which had been prepared primarily for ArGDC, as well as by stopping the operations of all the sets of DIP. (2) The sudden beam decay was initiated just after turning on one of the set of DIP during the storage of the beam. (3) The lifetime shortened was restored when the beam current increased in the range of 0.1 mA.

On the basis of the above results, at first we considered that the sudden beam decay might originate in the scattering by the Ar-ions trapped in the beam and the Ar atoms or ions might be emitted from the DIP. However, this consideration is unreasonable because the pressure averaged in the beam all around the PF ring was estimated to be too low to give such a short lifetime as described below. The emission of Ar from DIP, assumed to result in the sudden beam decay, is thought to occur in only one of the 28 bending sections since it is not natural that most of the sets of DIP installed in the ring may start emissions of Ar at the same time. If the electron beam in the PF ring is assumed to have a circular cross-section of 2 mm in diameter with the current of 100 mA, the density of electrons, averaged in the beam, is estimated to be 7×10^{8} electrons/cm^{3} so that the maximum pressure of Ar ions trapped in the beam existing within one bending section 2 m long is calculated as 2×10^{-8} Torr on the assumption of 100% neutralization. Therefore, the Ar-ion pressure averaged in the beam all around the ring of 187 m in a circumference is estimated to be 2×10^{-10} Torr, which gives a beam lifetime of 30 hrs from the calculations in Fig. 2.3.1.

Hence, we considered another origin. It is well-known that a shower of fine particles is generated in a spark discharge. The sudden beam decay is thought to be caused by the charged fine particles trapped in the beam, which may be generated in the accidental spark discharge occurring in the DIP and charged up by the irradiation of SR. For example, as shown in Fig. 2.3.8 where the process of the trapping of fine particles is illustrated, a fine particle of nickel with a globular shape of 2 μm in diameter

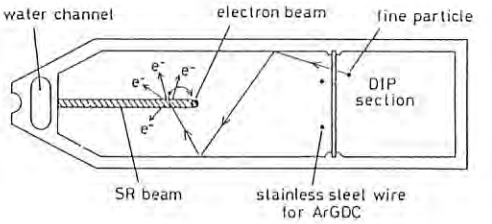

Fig. 2.3.8 Model of the trapping of charged fine particles in the beam.

is assumed to cross the SR beam emitted from the electron beam of 100 mA with an initial velocity around several ten m/sec so that photoelectrons with a number more than 1×10^{3} may be removed from the particle. Since the minimum electric charge required for the particle to be trapped in the beam against the gravity is estimated to be 7×10^{-20} Coulomb being less than the charge of an electron, the possibility of the trapping is very high. The number of Ni atoms contained in the particle is calculated to be 4×10^{11} atoms so that the equivalent Ni pressure averaged in the beam of 2 mm in diameter is estimated to be 2×10^{-8} Torr. Thus, from the calculations in Fig. 2.3.1 we obtained the corresponding lifetime of 14 mins, a reasonable value for explaining the sudden beam decay.

We have rarely observed the sudden beam decay in the recent operation of the PF ring because the operations of the DIP become so stable that the spark discharge may not occur frequently.

2.3.5 Outgassing from the Viton-Sealed Gate Valves

There are 312 buckets in the PF ring because the rf frequency is chosen as 500.1 MHz with the revolution frequency of 1.603 MHz. In the single-bunch operation, the pressures near the gate valves with viton seals showed notable increases while they did not change obviously during the multi-bunch operation where all the buckets were filled equally with electrons. Figure 2.3.9 shows the comparison between the beam current dependences of the pressure, averaged along the circumference of the ring, in the single-bunch and multi-bunch operations. As shown in Fig. 2.3.9, the pressure rise, considered to originate in the outgassing from the viton seals mounted in the gate valves, is found to be more conspicuous in the single-bunch operation. When all the gate valves were disassembled afterwards, we found that the nearest part of each viton seal to the stored beam degenerated with a mosaic shape. The origin of the outgassing is considered to be a heating-up of the viton seal by the wake field generated by bunched beams.

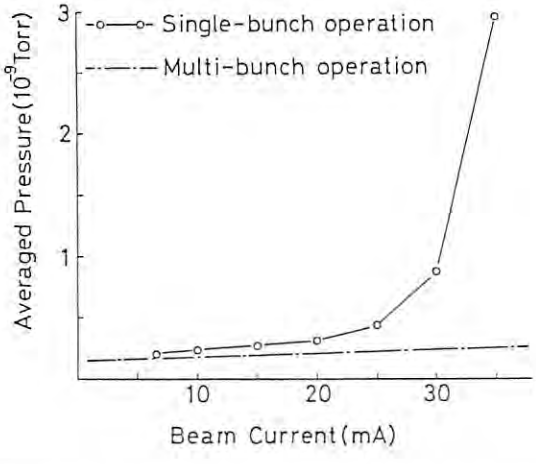

Fig. 2.3.9 Comparison between the beam current dependences of the pressure averaged along the circumference of the ring in the single-bunch and multi-bunch operations.

In the case of the multi-bunch operation, the Fourier components of the wake field show line-shaped spectra consisting of many higher harmonics with the fundamental frequency of 500.1 MHz so that no absorption of radiation might occur if the dielectric-loss spectra of viton did not overlap them. On the other hand, because the wake field generated in the single-bunch operation has quasi-continum spectra extending to several ten GHz, it may necessarily overlap the loss spectra with an eminent absorption.

All the viton-sealed gate valves being used in the PF ring will be exchanged for all-metal gate valves with shields against the wake fields so that the vacuum performances during single-bunch operations may be improved so much.

2.3.6 Vacuum Problems of RF Cavities

General description

During operation of the PF storage ring, vacuum pressures near the RF accelerating cavities[13] sometimes increase, and it causes the beam lifetime to shorten. After the routine beam accumulation of 150 mA, the pressures gradually increase, although it does not occur every time, and sometimes gets into the 10^{-7} Torr range at the beam current of approximately 120 mA. Hence the beam lifetime is shortest at this current, and gradually recovers as the stored current decreases. This phenomenon depends upon the bunch filling structure[14] around the ring, therefore, it probably relates to the wake fields induced by the bunched beam.

Although we have not yet found its cause, vacuum problems actually occurred on the RF cavities will be described in this report, especially on the flange supporting the tuning plunger. When the cavity is powered by 30 kW in each, temperature at the surface of the tuner flange rises to 90 °C. This can cause a degassing or a thermal fatigue at the welded part. In fact, after baking of the cavity, an air leak was found at the welded point. Problems of this part and a plan for improvement will be discussed.

Temperatures at several points of the tuner flanges and the beam ducts were measured correlatively with the values of the pressures and the beam intensities. It was found no correlation among them.

Leak at tuner flange

In April of 1984, baking of the entire vacuum chambers of ring was carried out because the vacuum of the ring had never recovered after the accident of the leak from a beam line. The accelerating cavities were also baked out. After completion of the baking, cavity pressures of 2×10^{-9} Torr were obtained.

A trouble of the vacuum occurred on a cavity during the conditioning with high RF power. The ionisation vacuum guage placed at upstream of the cavities showed the sudden increase of pressures up to the range of 10^{-6} Torr followed by the periodic change of pressures as shown in Fig. 2.3.10. The

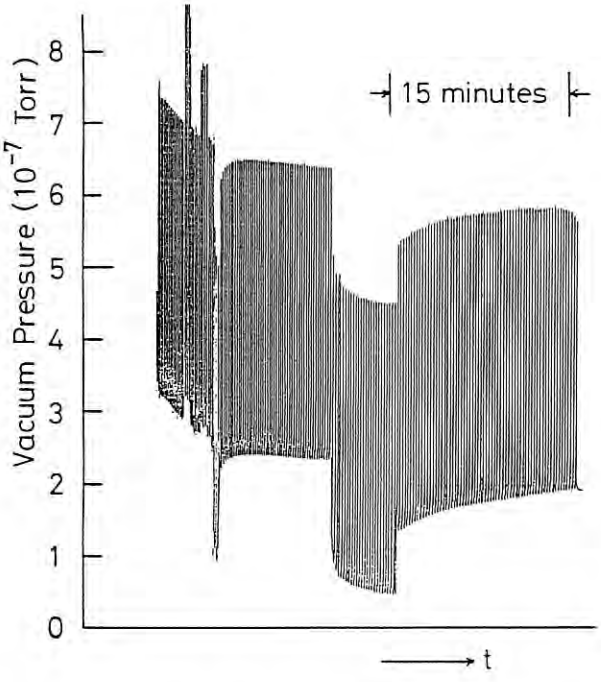

Fig. 2.3.10 The periodic change of the vacuum pressure near cavities recorded by the ionisation vacuum guage.

oscillating structure recorded in Fig. 2.3.10 has a period of about 8 sec in the beginning, which increases gradually up to 11 sec. The amplitude was almost constant unless the pumping speed of the evacuation system was changed. This phenomenon repeated intermittently as shown in Fig. 2.3.11.

A mass spectral measurement on the residual gases was made. The mass spectra were obtained on a ANELVA model AQA-100 MPX quadrupole mass-filter which was placed near the ionisation

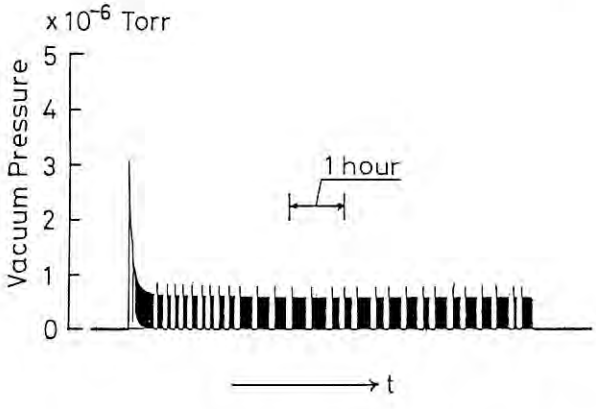

Fig. 2.3.11 The periodic change of the vacuum pressure recorded for several hours.

guage. It was found that the peaks at m/e of 14, 18, 28, 32 and 40 became high when the vacuum pressure increased. These peaks may be assigned to N, H_2O, N_2, O_2 and Ar, respectively. The result suggests that the increase of pressures is due to the leak of air.

In order to find out the location of the leak, a leak detection was made by use of a He leak detector (ANELVA model ASM 10). No leak of He was detected by the method of blowing He gas on the vacuum envelope. Then we tried to cover each part of the cavity with He bag. Finally it was found that He gas leaked into the vacuum chamber when the housing of a tuning plunger was covered by a He bag, and that the leak of He coincided with the increase of cavity pressures. Therefore it was concluded that the periodic change of pressures was due to the periodic leak of air and that the leak was located at the housing of a tuning plunger.

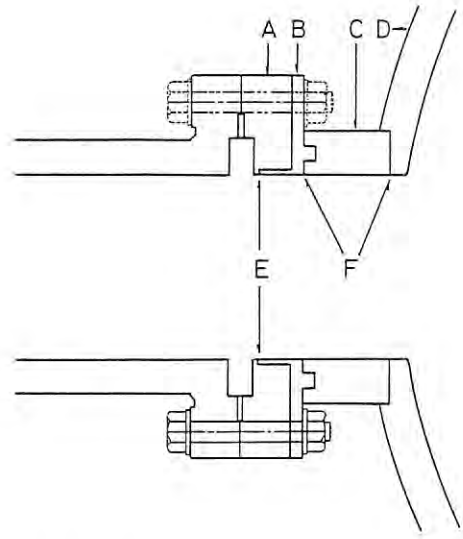

Fig. 2.3.12 Schematic drawing of the housing of the tuning plunger. A:vacuum flange,
B:transion piece, C:port, D:cavity body,
E:He-arc welded part,
F:silver-brazed parts.

Because we could never get rid of this leak, the cavity was exchanged for a spare. In order to probe the cause of the intermittent leak, the detailed investigation of this leak was made. Figure 2.3.12 shows the structure of the housing. The housing is composed of three pieces. A port made of copper, C in Fig. 2.3.12, is silver-brazed to the cavity body and a nickel-coated transition piece (stainless steel, B in Fig. 2.3.12) is also silver-brazed to the port. A stainless steel vacuum flange is

helium-arc welded to the transition piece. The leak detection indicated that the leak was located at the vacuum flange and its neighborhood. We found finally that oil-like liquid exuded on the surface of the vacuum side of the welded part between the vacuum flange and the transition piece as shown in Fig. 2.3.13.

Fig. 2.3.13 Photograph of the tuner flange. The oil-like liquid is seen at three points.

The reason for the periodic leak of air might be explained as follows: (1) The pin holes opened at the welded part during the conditioning of the cavity. (2) The welded part had the cracks filled with oil-like liquid. (3) Air penetrated in the liquid and a bubble formed. (4) When pressures of the bubble exceeded the surface tention of oil-like liquid, the bubble break and then the leak occurred.

The vacuum flange and its neighborhood mentioned above is heated by the RF field. The formation of the cracks or pin holes might be due to thermal fatigue. The housing of the tuning plunger has somewhat complicated structure so that it is difficult to detect or get rid of a leak. It is necessary to cool the tuner flange with water. Following improvements on this part are progressing: (1) The nickel-coated piece, B in Fig. 2.3.12, will be removed. (2) Inner side of the flange, A in Fig. 2.3.12, should be made of copper.

Deterioration of vacuum pressure near cavity

Another vacuum problem is the deterioration of the vacuum pressure near cavities which gives an important influence upon the beam lifetime. Figure 2.3.14 shows an example that the increase of the vacuum pressure near cavities causes the beam lifetime to shorten. The vacuum pressure, P in Fig. 2.3.14, increases abruptly up to the range of 10^{-7} Torr about one hour after the beam accumulation of 150 mA. The beam current, I in Fig. 2.3.14, decays rapidly with the increase of the vacuum pressure. The lifetime is shortest when the vacuum pressure reaches its maximum, and then, recovers as the vacuum pressure decreases. This phenomenon does not occur every time. The vacuum pressure near the cavities remains mostly 4×10^{-8} Torr or lower. In this case, the rapid decay as seen in Fig. 2.3.14 is not observed.

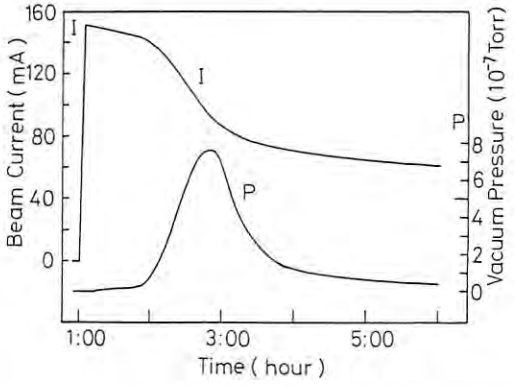

Fig. 2.3.14 An example of lifetime shortening due to the deterioration of the vacuum pressure near cavities.

The deterioration of the vacuum pressure depends upon the bunch filling structure around the ring. It occurs more frequently when the filling shape of RF buckets is more sharp. Therefore it probably relates to the wake fields induced by the bunched beam. The wake fields may heat some part of cavity and make degassing. The temperatures were measured at the several points of the tuner flanges and the beam ducts. It was found that there was no correlation between the vacuum pressure and the measured temperatures.

References

1. H. Winick et al.: Phys. Today 34 (1981) 50.
2. H. Winick et al.: IEEE Trans. Nucl. Sci. NS-30 (1983) 3097.
3. R.C. Sah: IEEE Trans. Nucl. Sci. NS-30 (1983) 3100.
4. European Synchrotron Radiation Facility: Supplement II. Machine (1979).
5. Photon Factory Activity Report 82/83 (1983) IV-48.
6. Photon Factory Activity Report 82/83 (1983) IV-46.

7. M. Sands: The Physics of Electron Storage Rings, an Introduction, SLAC-121 (1970).
8. S. Kamada: Proc. on Ultra High Vacuum Techniques for Photon Factory Project, KEK, Feb. (1979) 1 (in Japanese).
9. Photon Factory: Status of Storage Ring, Photon Factory Storage Ring Group: IEEE Trans. Nucl. Sci. NS-30 (1983) 3130.
10. H. Kitamura et al.: Proc. the 4th Symposium on Accelerator Science and Technology, November 24-26, 1982 at Institute for Physical and Chemical Research (RIKEN), Saitama, Japan, P.219.
11. M. Kobayashi et al.: Nucl. Instrum. & Methods 177 (1980) 111.
12. M. Kihara et al.: KEK Report, KEK-83-5 June (1983).
13. Photon Factory Activity Report 1982/83.
14. Y. Yamazaki, M. Kihara and H. Kobayakawa: KEK Report KEK 83-17, 1983.

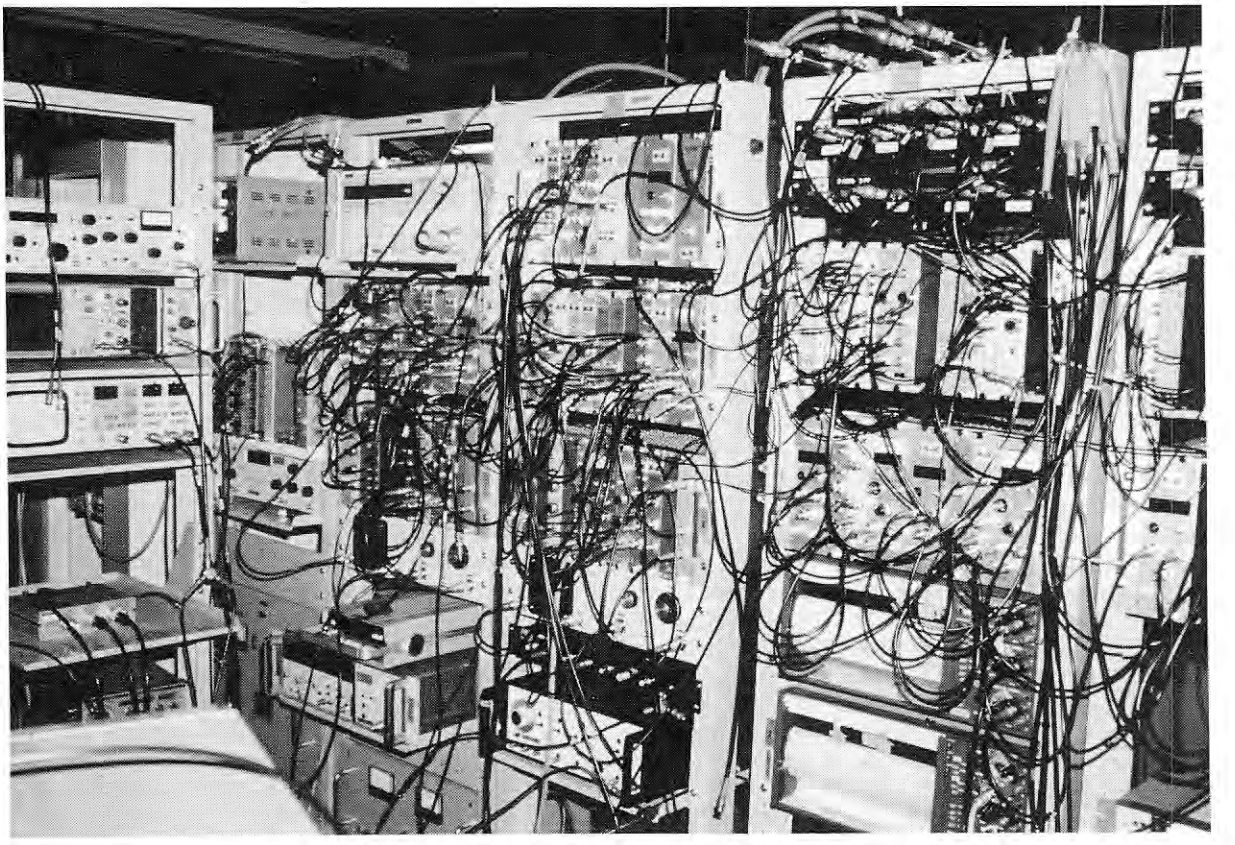

2.4 CONTROL

2.4.1 Control System by Computers Network

System overview

The layout of the control computer system is shown in Fig. 2.4.1. The control system consists of 7 control stations which are connected to each other through one exchange station, so each station can communicate with any other station. (Only exception is RF station, it cannot obtain access to this network because of its different operating system. The reason is explained later.)

Usually, each control station performs almost independently its own tasks, control/monitoring of the magnet system, the RF equipment, the vacuum system, the safety interlocks, operators console and beam monitoring system, etc. When a station needs to send/receive some data to/from other station, they can achieve it using program-to-program communication facility supported by the network system.

Both vacuum and beam monitoring stations leave a part of their work to micro-computer (PANAFACOM C-180, NEC PC9800) which sends/receives data to/from the host computer through RS-232C link.

The medium-size computer (FACOM M-200) with 6 MB of memory is also linked to the network through a front-end processor (FACOM U-400) to log and analyze operation data or do some simulation on orbit analysis. The computer is shared by TSS for batch users and experiment users.

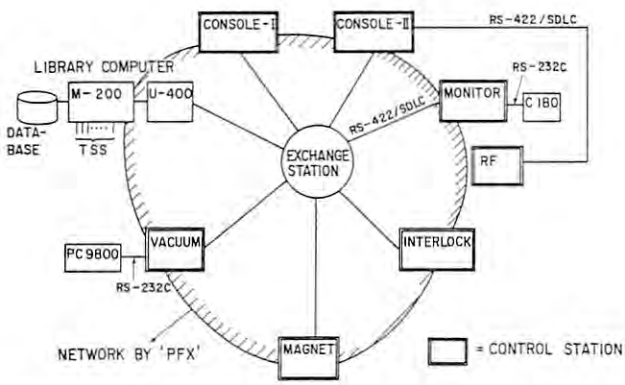

Fig. 2.4.1 Layout of the computer control system of Photon Factory storage ring.

Control station

Hardware configuration

A typical hardware configuration of the control station is shown in Fig. 2.4.2.

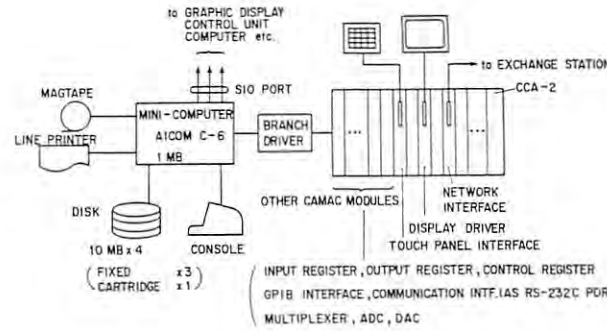

Fig. 2.4.2 Typical configuration of a control station.

Almost all objectives of controlling or monitoring are driven through CAMAC interfaced modules such as input/output register, control register, ADC, DAC and multiplexer, etc.. For some GPIB-interfaced devices such as digital multi-meter and coaxial relay etc. are also driven through CAMAC using GPIB-CAMAC conversion module.

The processing power is supplied by a 16-bit minicomputer (AICOM C-6) with 1 MB of memory. The CAMAC branch driver was specially developed for the computer. The computer has also serial I/O ports to drive some devices which have a I/O interface to the RS-232C link (graphic displays, microcomputers etc.). It is equipped with hard disks with capacity of 40 MB and a line printer. Furthermore, a magnetic tape unit is also installed to some stations for system maintenance. The local console is used only for system set-up or maintenance, so the operator usually interacts with touch panels or other console desk devices through CAMAC interfaces.

The communication with other control station is achieved by network interface modules of CAMAC as described in section 4 in detail.

Software structure

Figure 2.4.3 shows a schematic view of the memory assignment of the control station computer.

The multi-task real time operating system was developed and installed to perform both local data processing and network processing simultaneously.

An interactive language, 'PF-BASIC' (Photon Factory Basic) was specially prepared as a common language for the control program code. This has all features of standard BASIC with some extended functions and commands such as matrix calculation, virtual memory access, synchronized data communication with other computers and various interrupt handling (LAM of

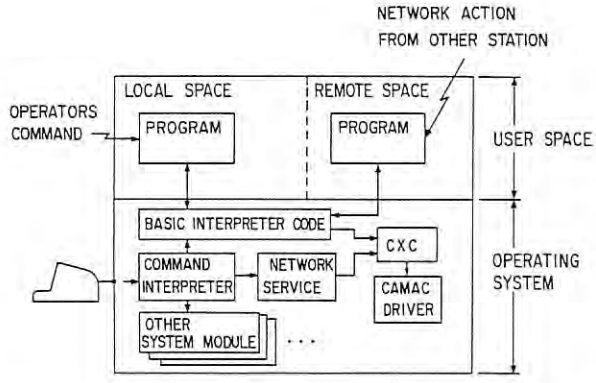

Fig. 2.4.3 A schematic view of memory assignment of a control station.

CAMAC, clock, network action) etc. The PF-BASIC interpreter code is made to re-entrant because it may be used by two or more programs at the same time.

A users space of main memory is divided into two areas, one for 'local space' and the other for 'remote space'. A boundary of two spaces is changeable and set at system boot-strapping. A single job is run in the local space by operators commands from the system console and one or more jobs are able to be executed in the remote space by an action from other computers through the network.

Two spaces are fully independent to each other, so there remains possibility that two or more programs access one CAMAC module at the same time. The system software module, 'CXC' (CAMAC exclusive controls) avoids this situation by keeping a management table of CAMAC, and all users program must access CAMAC only through CXC.

Some extended features like block transfer of memory, string functions and generalized treatment of some CAMAC modules (input/output register, multi-plexer, GPIB interface,...etc.) are provided in a form of BASIC-callable sub-routines for users convenience.

Network system

Hardware of Network

The intercommunication between computers is performed using network interface modules of CAMAC which are specially developed for the PF network system.

The interface consists of two modules. One is a fundamental module which processes CAMAC functions (as shown in Table 2.4.1) and controls interface unit. The other is a line control module which handles signals on a physical link. Various types of link, SDLC, RS-232C and parallel I/O etc., can be supported only by replacing the line control module without any change of other hardware/software environment. Two modules are connected by 60-wire flat cable.

Table 2.4.1

CAMAC functions of network interface module

F	A	Function	Q-Response
0	0	Read Received Data	Receive
1	0	Read Received Data Length	1
1	1	Read Status	1
1	15	Read Module ID Code	1
8	0	Test LAM	LAM
16	0	Write Transmitting Data	Transmit
17	0	Write Transmitting Data Length	1
17	1	Write Control Word	1
17	13	Write LAM Mask	1
22	14	Selective Clear of LAM	1

LAM source = Line error, Transmit error, Receive error, Transmit done, Receive done

The interface has two buffers of 2 kB each for both data to be transmitted and those received.

The possible errors of transmitted data are checked by means of CRC, check-sum and parity bit, so the interface requests re-transmission of data when it detects errors.

The PF network system uses SDLC protocol on RS-422 as a physical link, and the line speed can be chosen from 62.5 k $\sim$ 1 Mbps which is selectable by 4-bit DIP switch in the line control module.

Software of Network

The software of the network system has a three-layered structure as shown in Fig. 2.4.4.

The lower layer called 'DLC' (Data Link Control) manages a link between physical nodes.

The 'PC' (Path Control) is the middle layer and controls logical communication paths in order that PF Network allows multiple communications simultaneously on a single physical link.

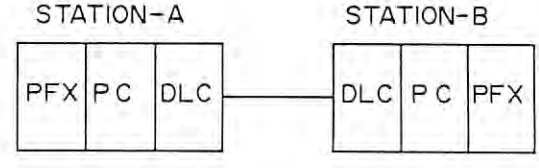

Fig. 2.4.4 Three-layered structure of the network software. DLC = Data Link Control, PC = Path Control, PFX = Photon Factory Executive.

The upper layer called 'PFX'(Photon Factory Executive) defines the protocol of the actual communication. Each layer is absolutely independent to its upper-side layer.

The message format is shown in Fig. 2.4.5. The message packet has three types of header corresponding to the software structure mentioned above. The 'DLC' header includes receiver/transmitter address, packet control word and transmitters terminal name. The 'PC' header contains informations on an identity of a communication and a message order number. The 'PFX' header keeps informations on length and content of text.

A text has variable size up to 2 kB and its content will be command, data, response or command completion code.

A fundamental features provided by PFX are as follows; file transfer, program-to-program data transfer and submitting program to other stations. These are supported by both operators command and BASIC statement. (A program-to-program data transfer is realized only by BASIC.)

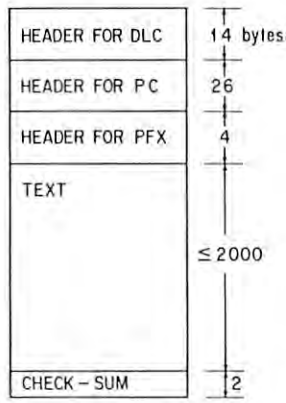

Fig. 2.4.5 Format of a message packet.

The exchange station simply distributes packets according to its physical node address, and all protocol processing of the networks must be done by each control station. This would be rather heavy load for a control computer sometimes. Furthermore, multi-task operating system, which is installed to realize the network, pays cost of large system overhead. For RF control station, this turned out to be an unendurable demerit because it lowers the speed of CAMAC accessing. So it uses ordinary single-task disk operating system which is unable to support the network by PFX. However, a data transfer from RF station to other control station is realized using the same network interface module and special protocol even in a restricted form.

Operation data aquisition

Continuous acquisition of data on the machine parameters is very useful for a trouble-shooting or a analysis of machine characteristics.

Operation data of each control station are gathered to the library computer through the network system. These data have a variety in their quantities, format and sampling rate. However, these must be treated in a unified way to provide easy and speedy access tools for database users.

To realize this request, we adopted 'multi-leveled file architecture' as shown in Fig. 2.4.6. (A part of this work is still in preparation.)

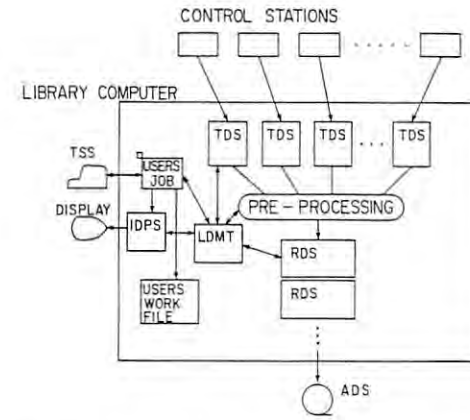

Fig. 2.4.6 Block diagram of the operation data acquisition. TDS = Temporary Dataset, RDS = Reserved Dataset, ADS = Archived Dataset, LDMT = Logged Data Management Table, IDPS = Interactive Data Processing Service.

Transferred data are added to 'temporary dataset (TDS)' group as one member of them. Every control station has its own TDS. The length and format of data are different for each control station, but each data should have a common heading which contains informations on time/date and beam current at the time when these data were taken. After pre-processing like deletion of unnecessary record, condensation and time-sorting, the data in TDS are stored to 'Reserved dataset (RDS)', so TDS is ready for next data. RDS is unique for a system and dumped to 'Archived dataset (ADS)' on a magnetic tape when it is full.

All these processes are performed by logged data processing utilities referencing a logged data management table (LDMT) which keeps all records on this procedure.

Users can search and access any data of a

certain period of time using time/date and beam current as indeces. They can save a copy of extracted data in their own work file or use interactive data processing service (IDPS) which makes time-dependence plot of any data or correlational plot of two or more quantities etc. from a TSS terminal.

2.4.2 Operation and Interlock System

System outline

The control system is organized by three-layer hierarchy consisting of INTERFACE, INTERLOCK and COMPUTER layers (Fig. 2.4.7). There are several tens of input and output signals from and to the machine components, radiation monitor, personal protection and interlocked doors.

The INTERFACE layer deals with all the signals converted from or to a standard form that can be processed by a programmable hard-wired interlock subsystem.

The INTERLOCK layer controls all the fundamental sequences of machine operation. It is constructed of NAND/NOR DTL gates.

The COMPUTER layer receives machine status signals via a CAMAC system for the operator's information and logging purposes.

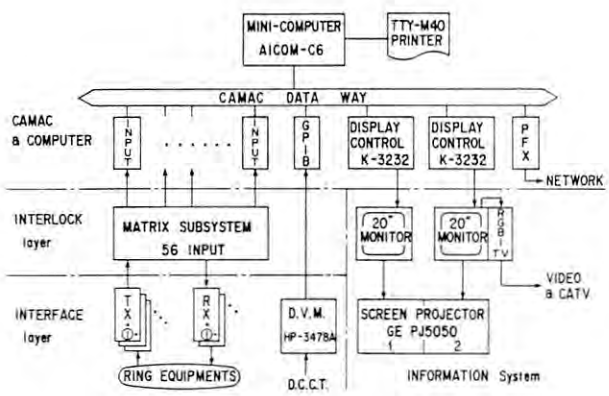

Fig. 2.4.7 Block diagram of Storage Ring operation control system.

Interface layer

The Storage Ring is composed of many components which transmit signals in various forms such as switch closures, analog levels, etc. The INTERFACE layer processes 56 signals to standard formats or conversely send back 7 control signals to the equipment with suitable signal level and formats.

Two types of modules, TRANSMITTER and RECEIVER were designed for constructing the INTERFACE layer. A TRANSMITTER module (TX) converts its input signal from the equipment to the standard signal and then transmits as the status to the interlock subsystem. Conversely, a RECEIVER module (RX) receives commands from the interlock subsystem and relays them to the destination components.

These modules have manual override key-switches on their front panels for maintenance or troubleshooting. The keys are normally unlocked and have no effect on the status or command. For maintenance or emergency recovery, one can stop sending status signals to the interlock subsystem or inhibit any command to the component by locking keys. With a locked key, the interface module goes into INHIBIT state which will be transmitted to the INTERLOCK layer as well as to the mini-computer, and displayed on the operator's console.

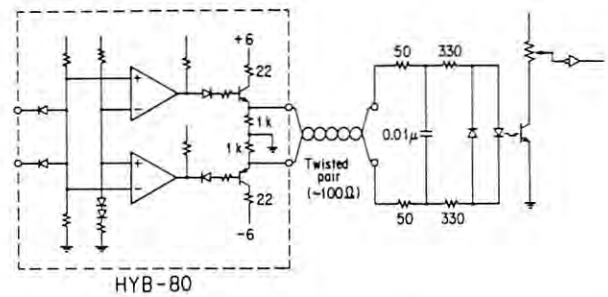

Fig. 2.4.8 A typical standard signal circuit.

The standard signal is specified to be balanced voltage output to a twisted pair and connected to an isolated load to prevent ground loop current. A logical "1" outputs 12 V to a twisted pair, and a logical "0" presents a high impedance state. Figure 2.4.8 shows a typical circuit made up of an optically isolated load and a HYB-80, which is a hybrid module developed by the Storage Ring Control Group. The same standard signal is used for a CAMAC in/out register.

INTERLOCK layer

The INTERLOCK layer is composed of matrix modules and connected to the Main Console Switch Panel (MCSP) for operator's command input (Fig. 2.4.9). All Storage Ring operation modes can be entered on operator's request via the MCSP only if safety conditions for the mode are satisfied. If any condition is not satisfied, this subsystem warns the operator with both MCSP display and audible alarm. The MAIN MATRIX module (PF410) encodes 8 different conditions from 64 status inputs by a pin programing matrix. The CHANNEL CONTROL module (PF412) concerns the light source channels. It permits channels to

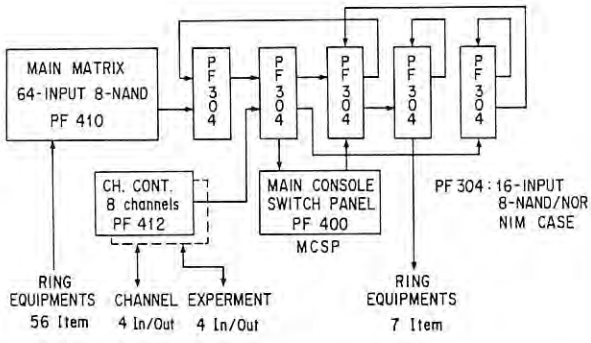

Fig. 2.4.9 Schematic drawing of the interlock subsystem. Main MATRIX and PF304 are built with pin programing matrices.

open, confirms if all channels are closed or detects unusual state of channels. The PF304 matrix module includes an 8 × 16 pin programing matrix, an 8 NAND/NOR change-over switch, two 8-input buffers and two 8-output buffers in a double widths NIM case. This matrix module is used as not only for normal NAND/NOR gates but also for FLIP-FLOPs by the aid of module interconnection. The safety condition for each operational mode is encoded from the status of components by the pin programing matrices, and the control signal is created with those module wiring. All the circuit time constants was chosen to be from a few micro-seconds to a few milli-seconds to filter out noise and relay chatter.

Figure 2.4.10 shows the diagram of operational modes and states. There are four modes: SHUTDOWN, LINAC ONLY, INJECTION and STORAGE. Each operational mode has one to three states and is represented graphically by a large circle. All permissible transitions are allowed by hard-wired logic and represented by arrows between states. Each transition labelled with a tag in the diagram is brought about by operator's action on the MCSP. In operation, the interlock subsystem waits until all conditions described below the tag of the chosen transition are satisfied, then it automatically controls the various components described below the horizontal bar.

The MCSP is shown in the lower half of Fig. 2.4.11. It indicates the present state with an LED light and informs abnormal condition in the same state with a blinking LED and audible alarm signal. The operator can tell which transition

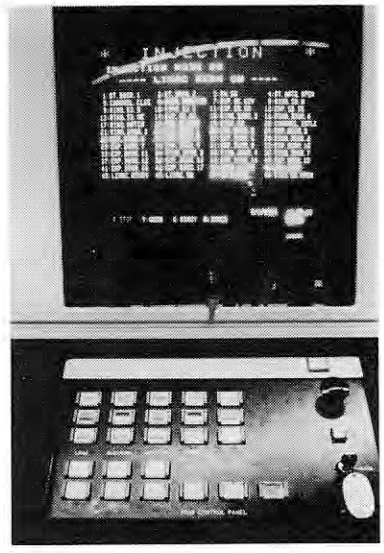

Fig. 2.4.11 20" color monitor and MCSP on the console desk.

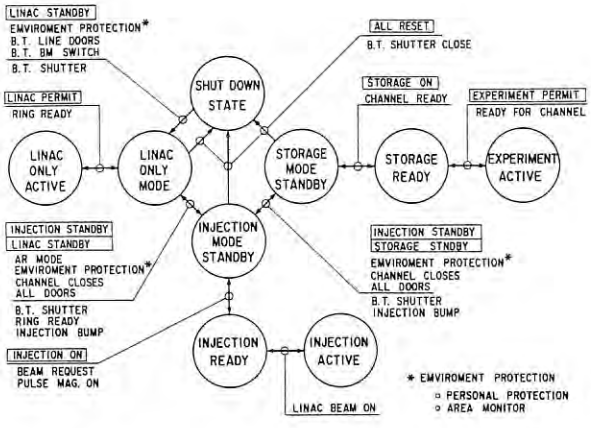

Fig. 2.4.10 Operation mode and state diagram. Refer to the main text for details.

between states is on by seeing both lighting LED of the starting state and a blinking LED of the ending state.

Computer and information system

The Storage Ring operation can be made safely within the two layers described above. However, it is necessary to install a computer to process status displaying, trouble hunting, information displaying and system logging.

The 16 bits mini-computer (AICOM-C6) consists of 1 Mb memory, 40 Mb storage disk, TTY model/40 printer, console terminal and CAMAC branch driver.

The surveillance program of about 2000 lines is written in PF-BASIC language, which is developed for the Storage Ring control on the computer.

There are two kinds of displaying media. Two 20" color monitors are installed in the console desk for displaying the ring status and information. There are two 1.92 m × 1.44 m large screen projectors on the wall of the control room (Fig. 2.4.12). They accept RGB signals or NTSC encoded signals and display the same contents as the monitors. They convenience the people working around the control room for they can be easily seen from any place.

Fig. 2.4.12 The Photon Factory Storage Ring control room.

Status Displaying

All conditions of the ring equipment connected into the INTERLOCK layer can be read at any time by the mini-computer via CAMAC modules. The surveillance program maps binary data to proper signal names such as OPEN/CLOSE, ACTIVE/NOT-READY and INHIBIT related to all components. The program prepares display frames for interlock safety conditions and logging summary. There are 11 different display frames: 10 for the states, and one for logging summary. When the operator triggers the MCSP, the program changes the display frame automatically. It takes a few tens of seconds in the worst case to change from one frame to the other mainly due to the overhead of the present operating system as well as the language itself.

Trouble Hunting

When any trouble should happen, the computer makes it easy to locate it and saves a lot time (It would be quite time-consuming work without any computer if one tries to do it by going directly to the INTERFACE layer). The program is always surveying all the status and comparing the current status with the previous one. When any changes found there, it will turn green letters into flashing red ones to inform where the trouble occurred.

Information Displaying

The information frame which is composed by the program contains beam current value, beam current vs. time in a graph form, beam lifetime, and status of the light source channels being used (Fig. 2.4.13). The frame starts at the latest injection from the LINAC, and it will be renewed at the start of the next injection.

The frame is also converted to composite video signals to be distributed to other places e.g. experimental area, LINAC control, CATV etc.

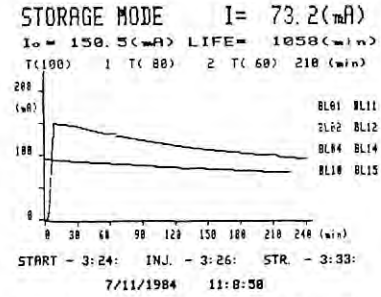

Fig. 2.4.13 A typical information frame.

System logging

System logging is also included in this program. The logged items are as follows:

1. Date and time of START or STOP of state.
2. Duration of state.
3. Duration of channel opening.
4. Integral beam intensity between injections.
5. Summary of the week's operation.

Figure 2.4.14 shows a sample printout of state transition and Fig. 2.4.15 shows a summary of week's operation.

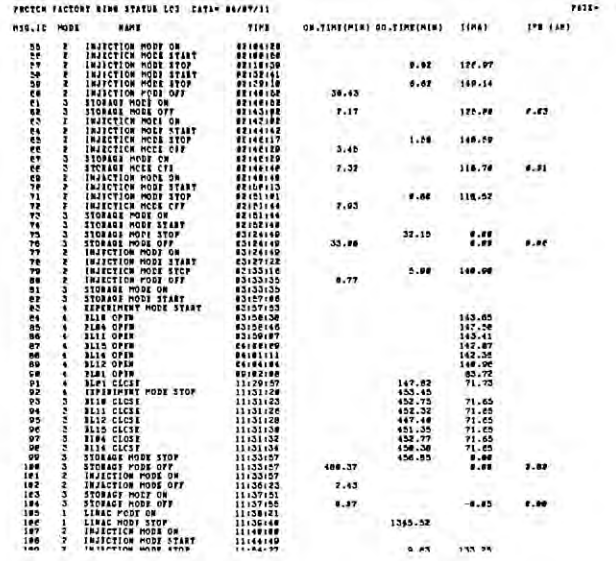

Fig. 2.4.14 A typical system logging printout.

```
      ************************************************
      *                                              *
      *   PHOTON FACTORY STORAGE RING WEEKLY REPORT  *
      *                                              *
      ************************************************

   OPERATIONS SUMMARY  FROM   07/10/1984   TO   07/14/1984
                              08:54:37         09:16:30

      ********************    PF    ********************

TOTAL OPERATION TIME:    5765.62 (MIN)     96.09 (HOUR)

MODE                    ON TIME                 GO TIME

LINAC            261.13 (MIN)    4.53% 1551.62 (MIN)   26.91%
INJECTION        770.75 (MIN)   13.37%  226.45 (MIN)    3.93%
STORAGE         4733.70 (MIN)   82.10% 4382.14 (MIN)   76.00%

(EXPERIMENT                             4094.07 (MIN)   71.01%)

      ********************   RING   ********************

 RING OPERATION TIME:    5504.48 (MIN)     91.74 (HOUR)

MODE                    ON TIME                 GO TIME

INJECTION        770.75 (MIN)   14.00%  226.45 (MIN)    4.11%
STORAGE         4733.70 (MIN)   86.00% 4382.14 (MIN)   79.61%

(EXPERIMENT                             4094.07 (MIN)   74.38%)

      ******************  CHANNEL  ******************

BL10            3876.95 (MIN)   94.72%
BL11            4071.75 (MIN)   99.45%
BL12            4021.03 (MIN)   98.22%
BL15            4043.60 (MIN)   98.77%
BL01            2657.82 (MIN)   64.92%
BL02               0.00 (MIN)    0.00%
BL04            4042.83 (MIN)   98.75%
BL14            2196.10 (MIN)   53.64%

      ******************   BEAM   ********************

THE NUMBER OF INJECTION =         34(TIMES)

TOTAL ACCUMLATE CURRENT =       9.58(AH)

MAXIMAM STORAGE CURRENT =     162.65(MA)
```

Fig. 2.4.15 A typical summary of the week's operation.

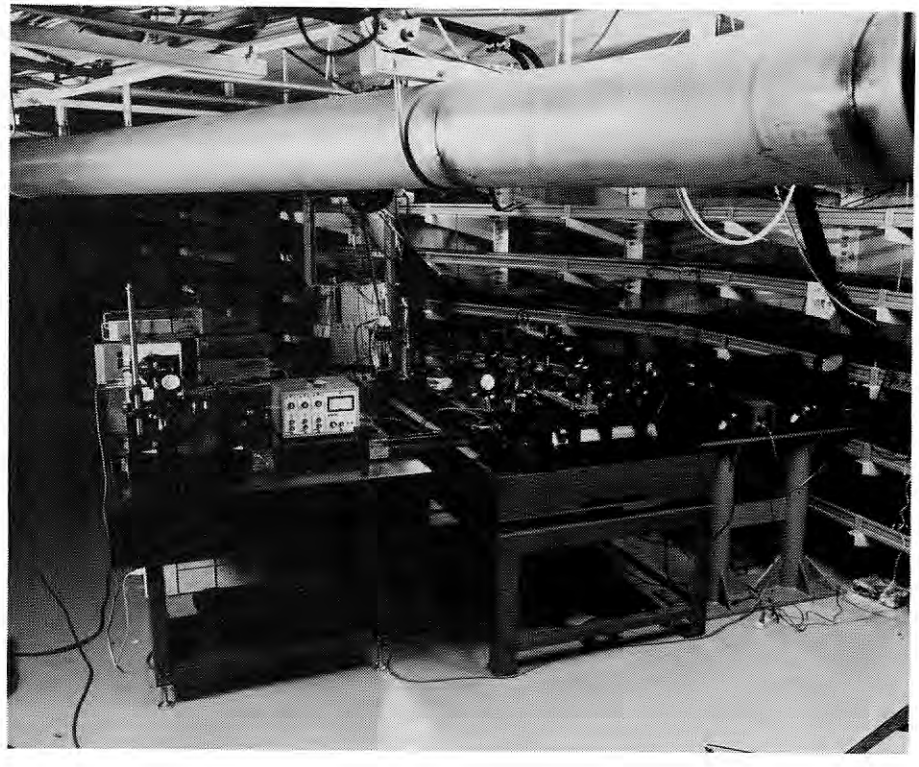

3. FACILITY DEVELOPMENT

3.1 SUPERCONDUCTING VERTICAL WIGGLER

3.1.1 Introduction

After the first operation of the superconducting vertical wiggler[1,2,3] with electron beams in February 1983, helium leak occurred at the welded part of coil case in the cryostat in May, so the wiggler was taken away from the storage ring and moved to the manufacturer for repair. It was reinstalled in the storage ring during the summer shutdown. From November the operation of the wiggler started again with electron beams. The main purpose of the operation in November and December was tuning-up of the wiggler itself, such as to decide the wiggler excitation pattern without closed orbit distortion, and to find the best operating tunes with respect to the beam lifetime. At the same time, experimental beam lines were tuned up using the wiggler radiation. Since February 1984, the wiggler has been operated in the user's time in parallel with other beam lines.

A wiggler magnet is one of the insertion devices which have been widely used in dedicated synchrotron radiation sources. Especially the wiggler magnet using superconductivity is capable of extending usable wavelength range to much shorter wavelengths. In the Photon Factory Storage Ring with the operating energy of 2.5 GeV, the characteristic wavelength is 3 Å for normal bending magnets, so that the intensity of radiation becomes very low at a wavelength less than 0.5 Å. Importance of intense hard X-rays from synchrotron radiation sources has been recognized for a long time, and a superconducting wiggler magnet has been intended to be installed in the Photon Factory from the beginning of the project.

One special feature to be noted here for the wiggler magnet of the Photon Factory is that the magnetic field is in the horizontal direction; that is, it is the vertical wiggler in which the electron orbit wiggles in the vertical plane. Radiation from the vertical wiggler is polarized in the vertical plane, while the radiation is horizontally polarized in usual horizontal wigglers. The vertical wiggler is beneficial for designing high precision X-ray spectrometers, and for the study of crystal growth. This implies, however, a somewhat difficult technical problem in designing the wiggler magnet. Generally speaking, the magnet gap should be as small as possible, so as to obtain high field strength. Since the beam size is quite small after a radiation damping time, the beam-stay-clear of 20 mm or more should be sufficient. In the injection time, however, excursion of injected beams are much larger than the beam size, and the aperture of 100 mm is required. In order to fulfill both requirements, the vertical wiggler is provided with a T-shaped vacuum duct, as seen in Fig. 3.1.1. Injected beams pass through the wider part of the chamber, and the magnet is moved down after the injection is finished. For this purpose, bellows of rather large size (265 cmϕ in reality) are needed on both ends. Since the space for bellows is limited in a given straight section, the stroke of vertical shift should be short. This requires that the superconducting coils should be as small as possible in the vertical direction, as can be seen in Fig. 3.1.1. It is clear that this requirement is contradictory to the magnetic requirement which claims that wider aperture is desirable for magnetic uniformity. Therefore, the final design was a compromise between two requirements.

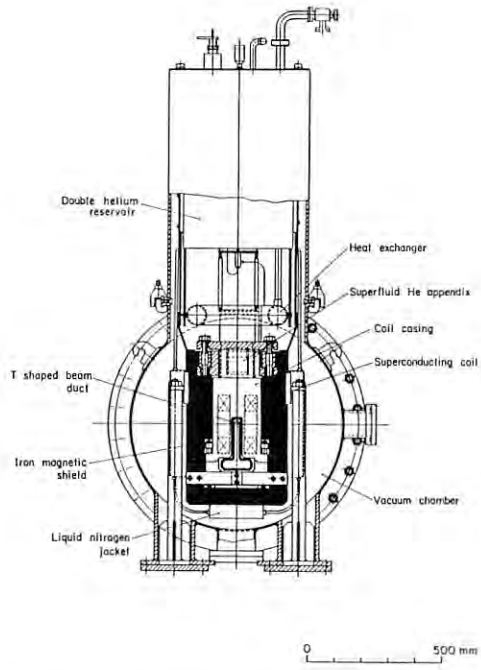

Fig. 3.1.1 Cross-sectional front view of the superconducting vertical wiggler.

This situation has given rise to a special operational problems in an actual operation of the storage ring. Especially, the regulation of the betatron frequencies must be stringent to obtain good beam quality. In this paper will be described the results of the study on the operating condition of the vertical wiggler, including the measurement of tune shifts, the resonance mapping, and the correction of tune shifts.

3.1.2 Orbit Correction

The vertical wiggler magnet of Photon Factory is a 3-pole superconducting magnet. The schematic drawing is shown in Fig. 3.1.2. There

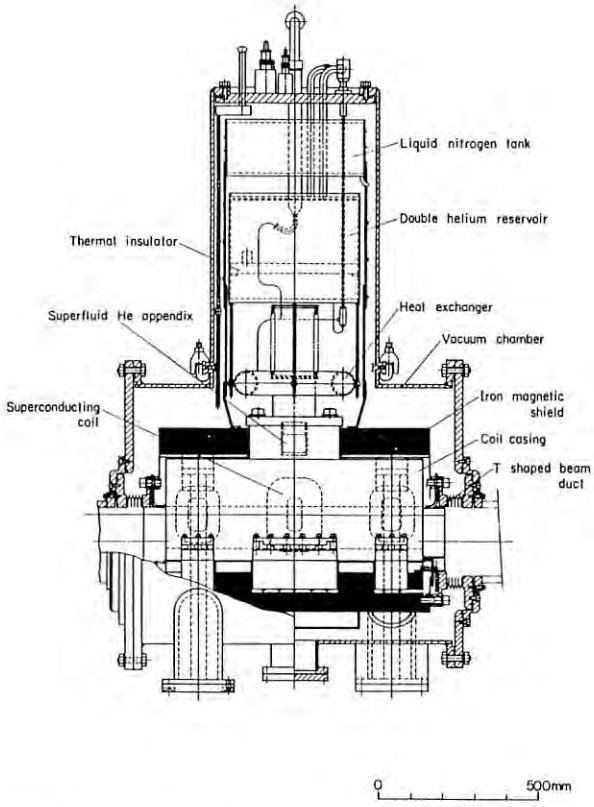

Fig. 3.1.2 Cross-sectional side view of the superconducting vertical wiggler.

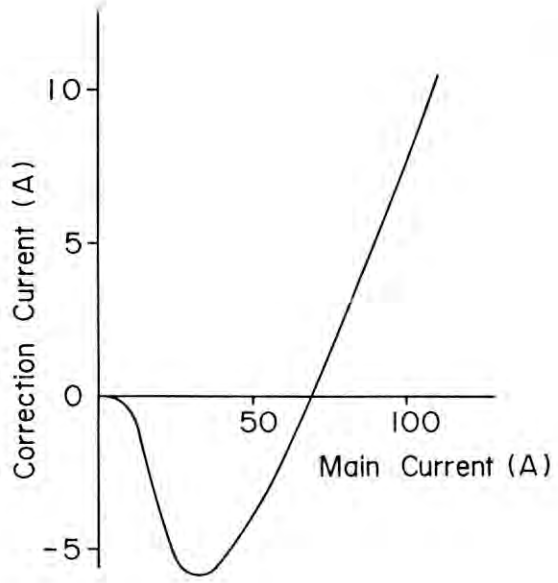

Fig. 3.1.3 Correction current as a function of the main magnet current.

are a central coil of nominal field strength of 6 Tesla and two outer coils of 3 Tesla. Three coils are connected in series and excited by a main power supply. Also, two auxiliary power supplies are connected to the outer coils.

The closed orbit during excitation is corrected by applying appropriate correction currents on two outer coils, so as to keep the position of electron orbit unchanged, which is observed by the beam profile monitor.

Figure 3.1.3 shows the correction current as a function of the main current. The correction current is a complex function of the main current especially at low fields because of the each iron pole and magnetic shield is in different magnetized state in the process of excitation.

In order to make the residual orbit distortion small enough not to disturb the experiments using photons, the correction currents have to be controlled with an accuracy of 0.01 ampere. Actually, the exciting currents are controlled by a pattern generator using a micro-computer, so as to ascertain the reproducibility of the excitation.

The reproducibility of the beam position have been confirmed by observations at several experimental stations and turned out to be satisfactory.

3.1.3 Tune Shifts and Their Correction

The wiggler magnet consists of three superconducting coils. The central coil of nominally 6 Tesla is a parallel edge coil of 174 cm in length. Two outer coils are parallel edge coils of 137 cm in length, and their nominal field strength is chosen to be 3 Tesla in order to reduce radiation loss as far as possible.

If the magnetic field in the wiggler magnet could be approximated by a set of rectangular magnets with uniform field strength, the betatron frequency would change only in the horizontal plane. In fact, however, the betatron frequencies vary vertically as well as horizontally, as seen in Fig. 3.1.4. This may be

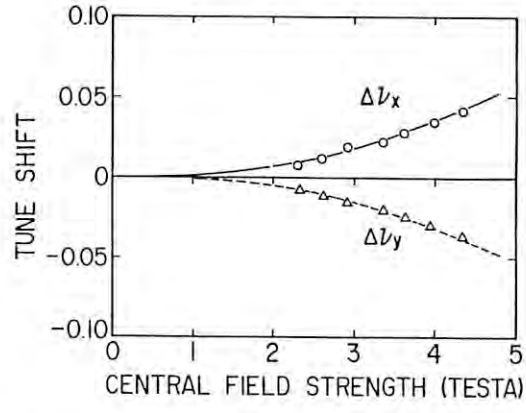

Fig. 3.1.4 Shifts of the betatron frequencies by the excitation of the wiggler.

due to the non-linearity in the magnetic field of the wiggler, as discussed later. The betatron frequencies must be kept constant in the course of excitation of the wiggler, because there are many dangerous resonances in the vicinity of the operating point. In the actual operation, currents of ring quadrupole magnets, QF and QD, which are located in the normal cells, are changed in accordance with the prescribed relations between correction currents and the excitation of the wiggler. Figure 3.1.5 shows the variations of the horizontal and vertical betatron frequencies after corrections are performed. Although corrections seem to be incomplete, a certain amount of tune variation at the low level of excitation gives rise to no problem, as will be described later, and the correction of tune shifts as shown in Fig. 3.1.5 is completely satisfactory in the actual operation.

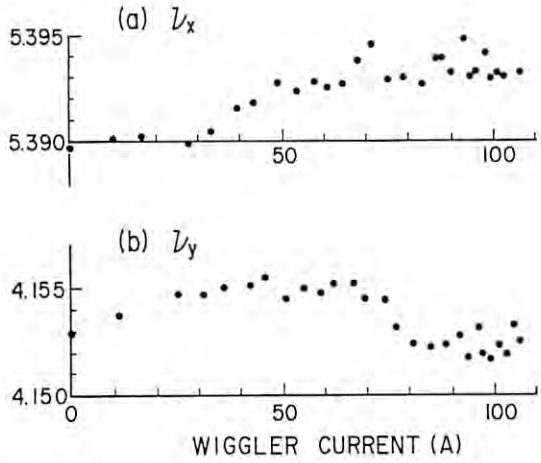

Fig. 3.1.5 Corrected betatron frequencies as functions of the exciting current of the wiggler.

3.1.4 Resonance Mapping Experiments

From experiences of running the storage ring with the wiggler magnet, we have observed that the lifetime of stored beams at the usual operating field of 4.5 Tesla is very critical to the betatron tunes. Also we have sometimes experienced undesirable beam loss during excitation. These phenomena could be understood by tune diagram survey, in which we have recognized that unstable lines or regions exist in the vicinity of the usual operating point. Figures 3.1.6(a) to 3.1.6(c) show mappings of resonance lines at wiggler excitations of 40 A (2.3 Tesla), 60 A (3 Tesla) and 106 A (4.5 Tesla). In these figures, solid lines represent resonance lines observed when the wiggler magnet does not work. The lifetime of stored beams is

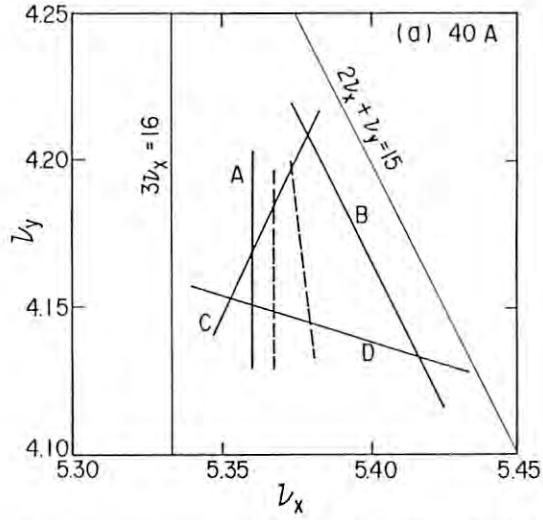

(a) the wiggler excitation 40 A (2.3 Tesla)

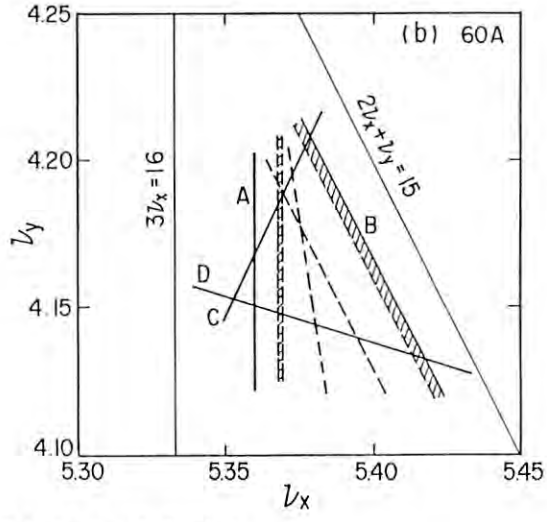

(b) 60 A (3 Tesla)

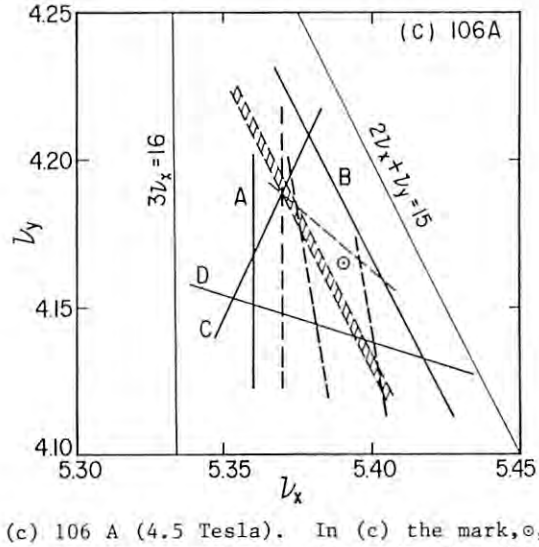

(c) 106 A (4.5 Tesla). In (c) the mark, ⊙, indicates the normal operating point in the recent operation of the Storage Ring.

Fig. 3.1.6 Results of resonance mapping.

shorter on these lines than in the area surrounded by them. Lines (A) and (B) could be identified clearly to be synchrobetatron resonances of the third order; (A) $3\nu_x - \nu_s = 16$ and (B) $2\nu_x + \nu_y + \nu_s = 15$. But the identification of resonance lines (C) and (D) is rather difficult, but it seems that the line (D) is $\nu_x + 3\nu_y + 5\nu_s = 18$.

When the excitation of the wiggler magnet is 2.3 Tesla, two new resonance lines appear, on which the beam lifetime becomes shorter, as seen in Fig. 3.1.6(a) by dashed lines. One of the lines seems to be the third satellite of $3\nu_x = 16$, while identification of another line is difficult. As seen in Fig. 3.1.6(b), there appears one more line at 3 Tesla, which corresponds to the second satellite of $2\nu_x + \nu_y = 15$. Also, the widths of stronger resonances become wider than at low level of excitation. As the wiggler excitation level increases, this trend is accelerated. At 4.5 Tesla, the stable operating area become narrower than before, since new resonance lines appear and old lines become broader. Results shown in Fig. 3.1.6(c) indicate that the betatron tune must be maintained within 0.005, in the vicinity of the normal operating point, at least in the high excitation levels.

3.1.5 Operation Status

By means of the tune correction, the beam lifetime became longer as in Fig. 3.1.7.

The wiggler magnet has operated at 4.5 Tesla usually, because the long lifetime enough for the user's run has not been achieved at the fields more than 5 Tesla.

The beam lifetime is also limited by vacuum pressure. The vacuum pressure in the down stream of the wiggler increase by one order of magnitude due to heating up of the vacuum chamber by wiggler radiation.

The pressure dependence of the lifetime can be seen clearly also in Fig. 3.1.7.

The reasons for the lifetime deterioration at the high stored current may be (a) increase in vacuum pressure, (b) increase in beam size, and (c) growth of the amplitude of the synchrotron oscillation. Although the vacuum pressure is an important factor to determine the beam lifetime, it is unlikely to explain the deterioration of the lifetime in this case solely by pressure increase. Since the physical aperture of the wiggler beam duct is small, an increase in the beam size may be dangerous to the beam lifetime. In the Photon Factory Storage Ring, the longitudinal coupled bunch oscillation exists above the current of about 40 mA. The coupled bunch oscillation is due to a higher order mode resonance of the cavity. The threshold current and the growth rate of the oscillation amplitude is dependent on the operating condition of the cavity; e.g. the temperature of each cavity. The horizontal beam size at 150 mA blows up by 20 % under the properly adjusted situation, but by more than 70 % when the adjustment is not complete. As a result, the beam lifetime becomes shorter; for example 200 minutes. In addition, considering that the number of synchrobetatron sidebands appear in the vicinity of the operating point, the amplitude growth of the synchrotron oscillation may be one of the causes to reduce the beam lifetime at high currents. Therefore, the beam loading

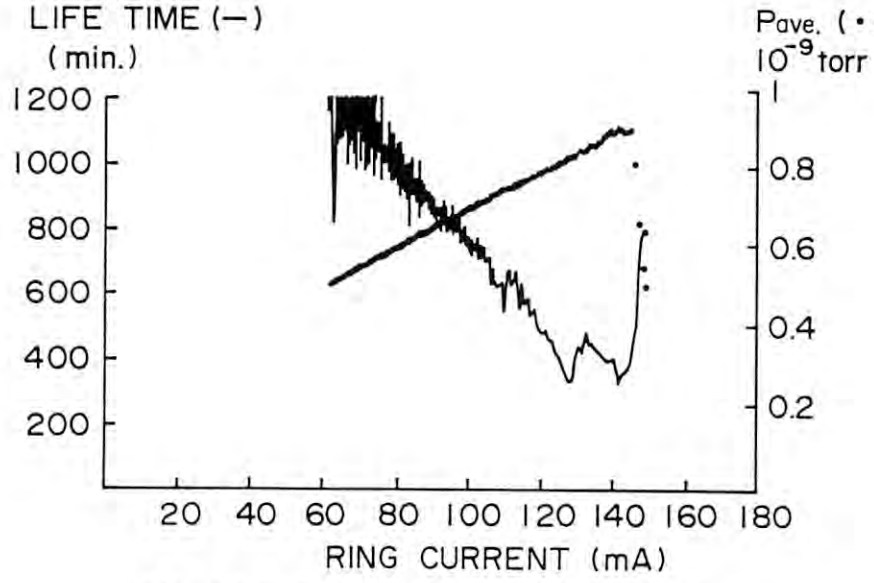

Fig. 3.1.7 Beam current dependence of the beam lifetime and the average vacuum pressure.

power and the cooling water temperature among four cavities have been adjusted carefully to suppress the longitudinal coupled bunch instability.

An effort to fined out much wider operating area has been continued. Figure 3.1.8 shows another example obtained at 4.5 Tesla. In this case, unstable points are distributed in a complex way, so that it was very difficult to draw distinct resonance lines from the results of lifetime mapping experiments, except for three lines indicated by solid lines in the figure. Resonances on the solid lines are strong, so that decay of stored beams is steep on these lines. It is clear that the resonance A is the first satellite of $3\nu_x = 16$, but identification of lines B and C is difficult. The resonance line C is weaker than A and B. A triangular shaped area is rather wide, compared to the former case. Therefore, it should be easy to operate the wiggler magnet in this region of tunes. But, this is in the unstable region with respect to the transverse coupled bunch instability, so that we can not store stable beams of more than 10 mA at these operating tunes, at this moment.

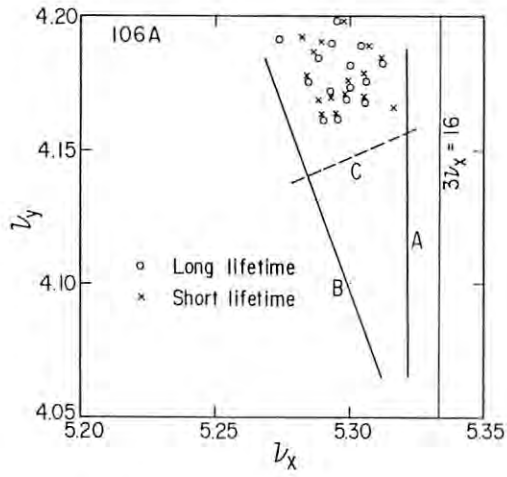

Fig. 3.1.8 Result of resonance mapping at another frequency region. The wiggler excitation is 106 A (4.5 Tesla).

3.1.6 Discussion

As remarked before, the betatron tune in the vertical plane should not change, if the vertical wiggler could be approximated by a set of rectangular magnets with uniform fields distribution. In the actual magnet, however, the magnetic field distribution is not uniform in the lateral direction.

The magnetic measurement, especially the measurement of the transverse distribution, is difficult in practice, because the physical aperture is only 30 mm. In addition, for the purpose of magnetic measurement, extra chamber must be put in the cold bore of the wiggler, so that available aperture becomes very small. Therefore, we only measured the distribution along the magnetic centerline, and we refer to the results of calculation using the computer for the transverse distribution. According the calculation, the transverse distribution can be fairly well approximated by a sum of dipole and sextupole fields. Results of the distributions of dipole and sextupole fields along the beam direction are shown in Fig. 3.1.9.

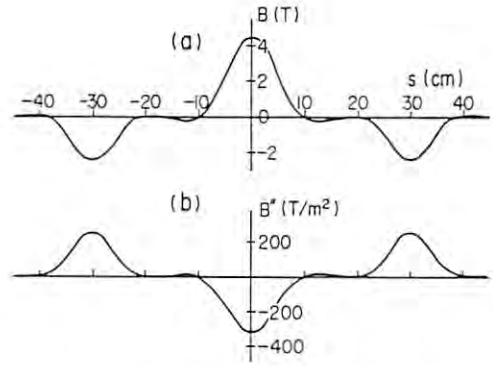

Fig. 3.1.9 Calculated field distribution in the wiggler. (a) dipole field, (b) sextupole field. s means the beam direction.

In the following, we will roughly estimate the betatron frequency shift due to the wiggler by using the calculated values of the magnetic field of the wiggler. For the betatron oscillation in the plane parallel to the direction of the magnetic field i.e. in the horizontal plane in this case, the tune shift can be considered to be originated by the non-normal entrance and exit to the magnet edge, and not to be affected by the non-linear fields in the first approximation. The tune shift due to edge focusing can be calculated easily and is turned out to be 0.04 at the excitation of 4.5 Tesla. Since the measured value is 0.05, agreement is very good.

For the tune shift in the vertical plane, which should be zero in ideal parallel-edged magnets, can be considered to be due to non-linear fields. Considering the orbit deviation is 10 mm in the wiggler, the estimated value of the tune shift is 0.028, which is in good agreement with the measured value of 0.04, again at 4.5 Tesla. Since the measured value is 0.05, agreement is quite good.

For the tune shift in the vertical plane,

which should be zero in ideal parallel-edged magnets, can be considered to be due to non-linear fields. Considering the orbit deviation is ±5 mm from the magnet centerline of the wiggler, the estimated value of the tune shift is 0.028 at 4.5 Tesla, which is in good agreement with the measured value of 0.04. Contributions from the central coil and the outer coils are additive, so that the position of the beam relative to the magnet centerline of the wiggler does not affect the tune shift in the first approximation. Instead, an amount of the orbit wiggler is primarily important to give the tune shift.

References

1. K. Huke, T. Yamakawa: Nucl. Inst. and Meth. 177 (1980) 253-257.
2. C. Lesmond: KEK Reports KEK80-17 March (1981).
3. T. Yamakawa, H. Kitamura, S. Sato, E. Takasaki, T. Shioya and C. Lesmond: Proc. of the 4th Symp. on Accel. Science and Tech. Nov. (1982) 315-316.
4. Y. Yamazaki, H. Kobayakawa, Y. Kamiya and M. Kihara: KEK 83-7.
5.
6. Y. Yamazaki, H. Kobayakawa, Y. Kamiya and M. Kihara: KEK 83-3.

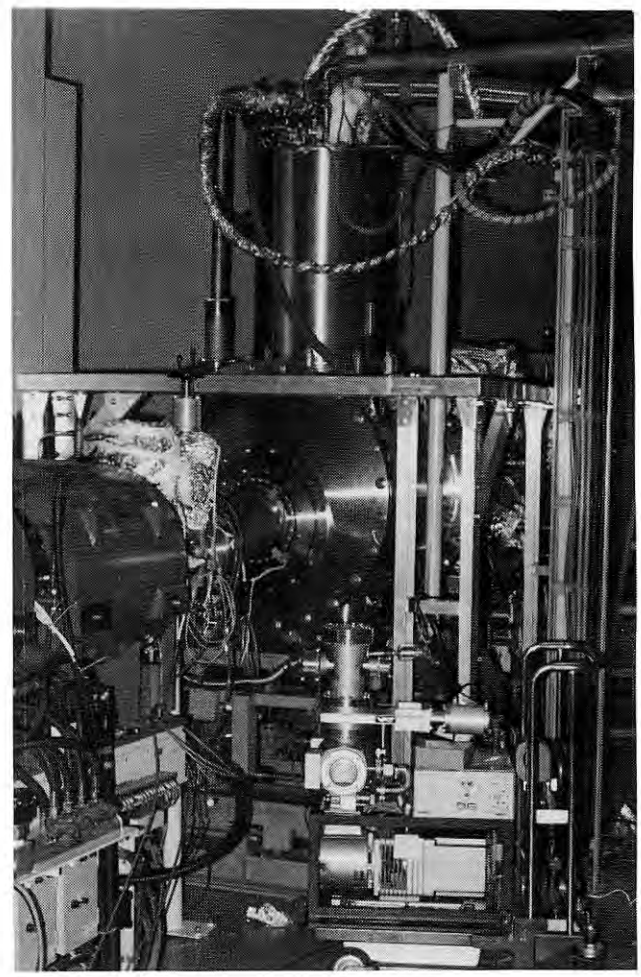

3.2 BEAM CHANNEL

With the opening of the wiggler beam channel for user experiments in February 1984, a total of eight beam channels are currently in operation. The development of two new beam lines are under way at present. The beam lines available to users as of July 1984 are summarized in Table 3.2.1. Some specific aspects related to beam channels are described.

Table 3.2.1

Beam lines being operational as of July 1984

Beam line	Source	Experimental spectral region
BL-1	normal bending magnet	VUV and soft X-ray
BL-2	permanent magnet undulator	soft X-ray
BL-4	normal bending magnet	X-ray
BL-10	"	"
BL-11	"	VUV and soft X-ray
BL-12	"	"
BL-14	superconducting vertical wiggler	hard X-ray
BL-15	normal bending magnet	X-ray

3.2.1 Wiggler beam line

The wiggler beam line (BL-14) accepts a 9 mrad vertical divergence of radiation emitted from a superconducting vertical wiggler, which is installed in the medium straight section between bending magnets B13 and B14. The wiggler radiation is split into three branch beams, and is used for structure analysis (BL-14A), precision X-ray optics (BL-14B) and X-ray topography (BL-14C).

The front end for BL-14 is shown in Fig. 3.2.1. It consists of a fast closing valve, a safety beam shutter, a water-cooled light absorber, beryllium windows and vacuum components. Unlike in the other beam lines, an acoustic delay line is not installed in BL-14 because of insufficient space in the alcove. Two 110 ℓ/s triode ion pumps and two titanium sublimation pumps are installed for the main pumping. A 170 ℓ/s turbo molecular pump is used for rough pumping during bakeout. A base pressure of 1×10^{-10} Torr has been achieved by baking at a temperature of 250°C for about 30 hours.

Beryllium windows[1] are attached at the downstream termination of the front end to provide hard X-ray components of synchrotron radiation (SR) to the experimental stations.

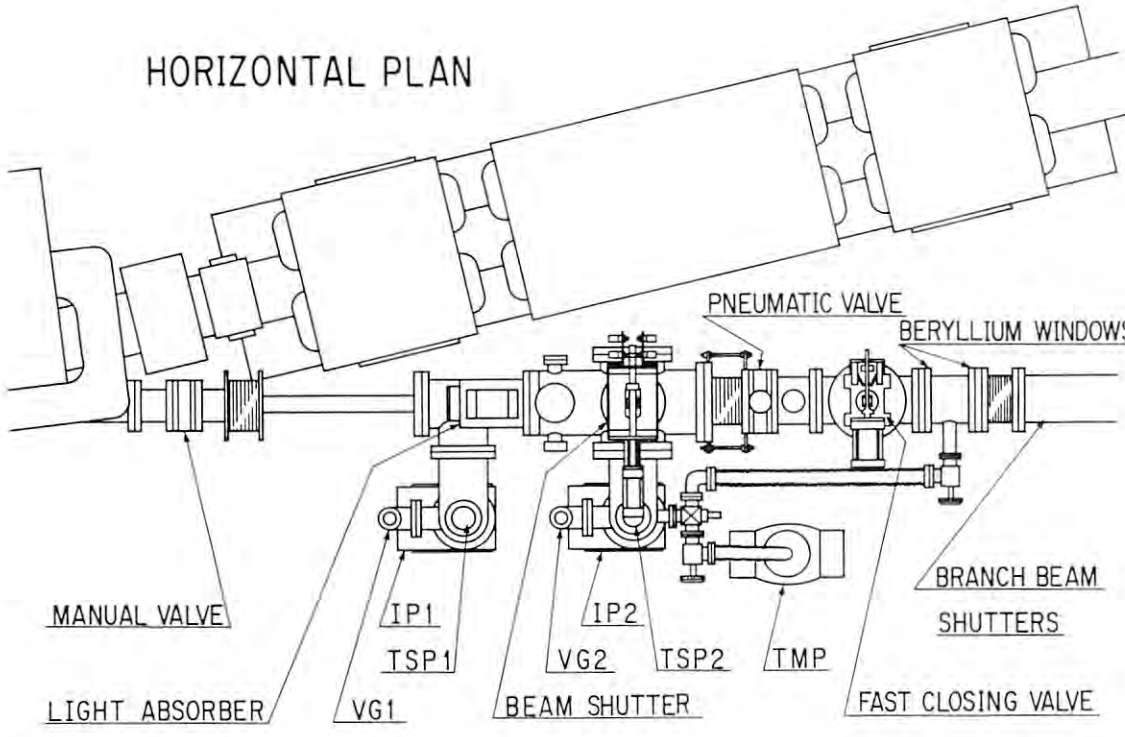

Fig. 3.2.1 Layout of the front end for the wiggler beam line (BL-14).

Figure 3.2.2 shows schematically the arrangement of the beryllium windows. This configuration was chosen on the basis of the calculations for the transmitted intensity of X-rays and for the

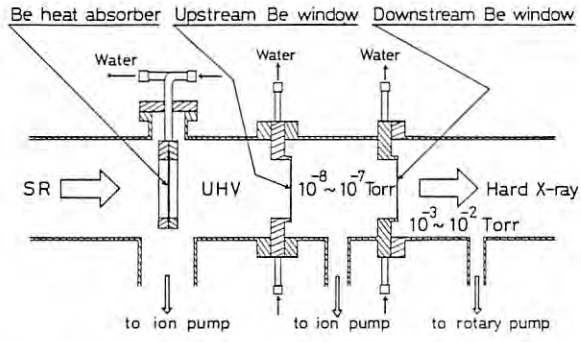

Fig. 3.2.2 Schematic of the Be window configuration for the wiggler line.

thermal and mechanical stress in the beryllium foils[2,3]. Each window is 0.3 mm in thickness, 98 mm in height and 18 mm in width. Joining a thin beryllium foil to a frame was done by electron beam braze-welding. The radiation power density is calculated to be as high as 200 watts per 1 mrad vertical divergence with the 6 T wiggler operating at an energy of 2.5 GeV with a nominal beam current of 500 mA. An upstream window faces a UHV environment and stands the heat load. A beryllium heat absorber with a thickness of 1 mm is installed in the UHV system to reduce the thermal load imposed on the upstream window. The middle section between two windows is pumped to $10^{-8} \sim 10^{-7}$ Torr with an 8 ℓ/s ion pump. Beam pipes from a downstream window to the experimental apparatus is evacuated to $10^{-3} \sim 10^{-2}$ Torr with rotary pumps to protect the beryllium foil from oxidization and to avoid absorption of X-rays by air. The downstream window is only exposed to the small thermal load because the heat absorber and upstream window absorb most of the VUV and soft X-ray components of SR. The beryllium windows with a total thickness of 1.6 mm mainly transmit X-rays shorter than 3 Å. The window frames and the heat absorber holder are water cooled to suppress the temperature rise in the beryllium foils.

3.2.2 Operation experience with SiC mirrors and Be windows[4,5]

In the VUV beam lines (BL-11 and BL-12), SR is divided among 3 or 4 branch beams and is then delivered to monochromators through beam deflection mirrors. Chemical vapor deposited (CVD) silicon carbide (SiC) was chosen as a mirror and mirror substrate material because of its high resistance to thermal distortion and to radiation damage and other desirable qualities.

Figure 3.2.3 shows the optical arrangement of the branch line to a grasshopper monochromator on BL-11. A Pt-coated flat SiC mirror has been used as a horizontal beam deflector M_0. The

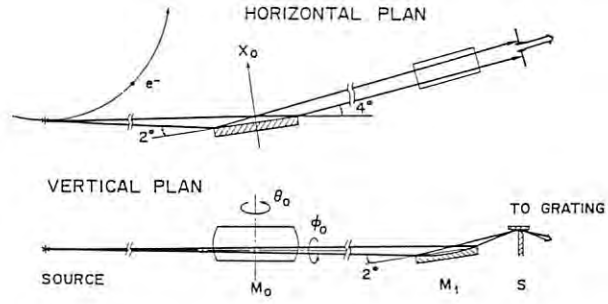

Fig. 3.2.3 Optical arrangement of the grasshopper branch line on BL-11.

grazing incidence angle of 2° requires a mirror as long as 40 cm to receive 1.3 mrad horizontal divergence radiation. Since the mirror chamber is located inside the shielding hutch and is distant from the experimental station, the adjustments for θ_0, ϕ_0 and χ_0 motions of the mirror is achieved with stepping motors remotely controlled from the experimental station. The remote control system has proved to be useful in the event of vertical or horizontal electron-beam orbit displacements in the ring.

A photograph of the mirror M_0, which has been used for a year, is shown in Fig. 3.2.4. The mirror shows visible evidence for carbon contamination under intense SR exposure, though the mirror chamber has been kept at pressures of

Fig. 3.2.4 Pt-coated flat SiC mirror having been used on the grasshopper line. It has a size of 40 × 17 × 4 cm^3.

$10^{-9} \sim 10^{-8}$ Torr. The two stripes were produced as a result of reusing the mirror with both sides interchanged. Renewal of the reflecting surface resulted in an increase in the beam intensity incident on the monochromator especially in the vicinity of carbon K edge at 284 eV.

In the X-ray beam lines (BL-4, BL-10 and BL-15) from bending magnets, vacuum-tight beryllium windows to separate X-ray experimental areas from the ring vacuum have already been used for a year or more. As described for the wiggler line in section 3.2.1, a double window type was chosen to provide protection even in the event of window failures. Figure 3.2.5 shows a photograph of the window assemblies, which have been used on BL-4. The downstream beryllium foils, which have faced the experimental beam lines at pressures of $10^{-3} \sim 10^{-2}$ Torr, are found to be slightly oxidized after one year use in the intense SR beam. The upstream windows, on the other hand, show no appreciable evidence for oxidization or radiation damage.

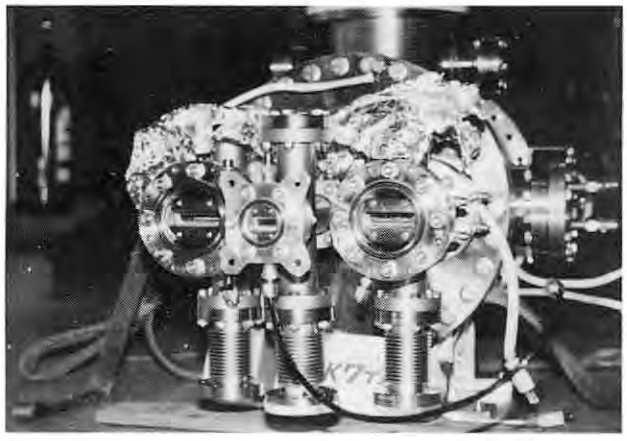

Fig. 3.2.5 Be window assemblies having been used on BL-4. The downstream windows are seen.

3.2.3 Measurement of the SR height at BL-10

It was sometimes reported that the SR beam in BL-10 changed in height, depending on the operating conditions in the storage ring, and that part of the X-ray beam was too low to pass through the beryllium windows. The SR beam height at the beryllium windows on BL-10 was measured as a function of the magnitude of a local orbit bump produced at the location of the bending magnet B10. The scheme for the measurement is shown in Fig. 3.2.6. A fluorescent screen was placed just downstream of the beryllium windows on BL-10A and BL-10B. The screen

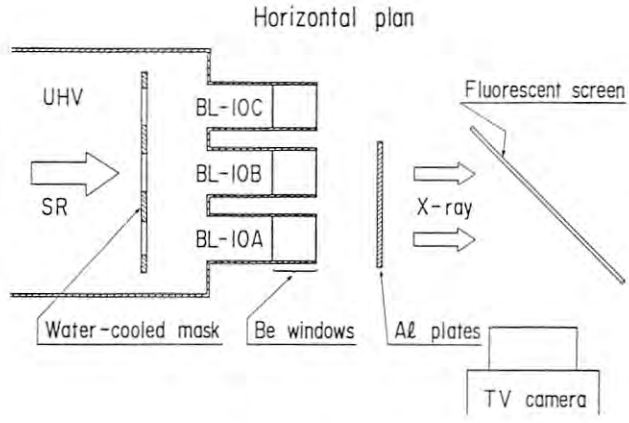

Fig. 3.2.6 Arrangement for the X-ray height measurement made on BL-10. The Be windows are located about 10 m away from the source.

had horizontal scale marks graduated in 2 mm increments. The central mark was adjusted to the center line of quadrupole magnets, the level of the orbital plane. Aluminum plates 3.8 mm in total thickness were put between the screen and the beryllium windows to reduce X-ray intensities transmitted through the windows. The storage ring was operated at 2.5 GeV and 16 mA. The position of the X-rays striking the screen was monitored with a TV camera while changing the magnitude of the corrective bump. The result of the measurement is shown in Fig. 3.2.7. The SR beam was found to be lower than the level of the orbital plane by 4 mm without any orbit bump. The beam coincided in height with the electron orbit when a vertical orbit

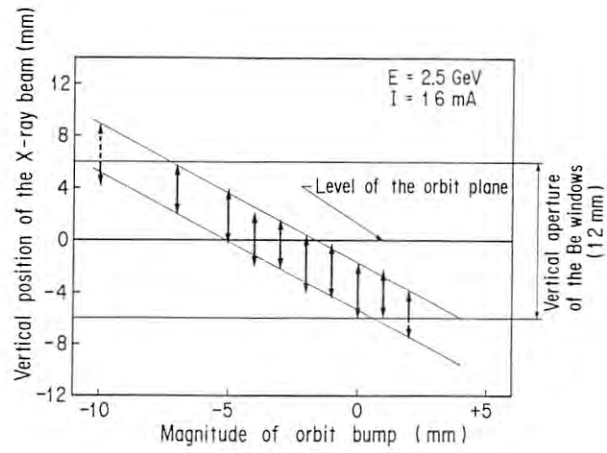

Fig. 3.2.7 SR beam height at the Be windows on BL-10A with a local orbit bump produced in the ring at the location of the bending magnet B10. Segments with arrows indicate the vertical width of the X-ray beam.

bump of - 3 mm was generated. It should be noted that an increase in the bump resulted in a decrease in the beam height. This is because the major effect of the bump on the SR beam was to change the vertical gradient of the beam. The storage ring has been operated with reference to the result of this measurement.

3.2.4 New beam channels

Two new beam lines (BL-7 and BL-8) are being developed as a joint effort between the Photon Factory and outside groupes. Both beam lines are bending magnet lines.

The project for BL-7 is a collaboration between Research Center for Spectrochemistry, The University of Tokyo and the Photon Factory. The design of the front end has been finished and beam line components are presently in fablication. BL-7 will be used for angle-resolved photoelectron spectroscopy, photo-stimulated desorption and X-ray experiments.

BL-8 is affiliated with Hitachi, Ltd. Responsibility for the design and construction of the line rests with Hitachi, with the co-operation of the Photon Factory. Currently beam line components of the front end have been completed and will be installed during the shut-down weeks for the ring in this coming autumn run. BL-8 is intended for use in EXAFS, soft X-ray spectroscopy, lithography, tomography and so on.

Both BL-7 and BL-8 have been designed to satisfy the basic specifications required for the beam lines currently operational. Their front ends contain a fast closing valve, an acoustic delay line, a safety beam shutter and a water-cooled light absorber. These protective devices are to be sequentially operated with a control system[6], which will be presented in the next section.

3.2.5 Beam Line Control System

There are twenty four possible beam line ports at the 2.5 GeV electron storage ring. At present, nine beam lines are installed along lines tangent to the electron storage ring. They feed synchrotron light to the hall where many experiments, including X-ray lithography, microscopy and crystal structure analysis are carried out, simultaneously.

There are many components installed on the beam line, for example; five open-close units, two vacuum monitors, four ion pump controllers, and safety interlock systems such as cooling-water, vacuum protection, and compressed-air interlocks.

A beam line with such components must be controlled independently of adjacent beam lines by the outlying node in charge of that beam line. This is especially important for synchrotron radiation experiments which may vary greatly in their needs. In addition, all the beam lines are distributed over the 180-meter-round storage ring.

The distributed control system, an application of computer network with a star topology, currently implemented to control all the beam lines at the Photon Factory[6] is described. This computer network is designed to accommodate various beam line features; i.e., by only modifying lower level software and/or hardware modules on an outlying node to adapt to different features of the beam line, systematic control at the central node is carried out with almost the same control process for each beam line.

Requirements for the control system

The beam line control system must satisfy the following requirements:

1) The system must automatically collect information on the status of all beam lines.
2) The system must generate an alarm when it finds an incorrect state.
3) The system must display the current operational status of beam lines on color CRT's.
4) The system must manipulate valve/shutter units on request signals from beam line users, as well as from the system console at the central node.
5) When one beam line goes down due to an accidental failure, the system must carry out error diagnosis for fast recovery.

The distributed control system is designed based on the above requirements. Figure 3.2.8 shows the configuration of the system, where the outlying nodes and the central node are connected via optical fiber links in a star topology.

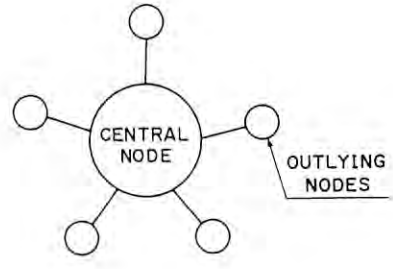

Fig. 3.2.8 Star topology.

Outlying node

The outlying node only controls a set of components attached to the beam line, in accordance with a preprogrammed process, as well as commands received from the central node, and request signals from beam line users.

This node is a Zilog Z-80A based microcomputer system with parallel input/output interfaces and dual serial communication ports. These outlying nodes are physically distributed over the storage ring. Each outlying node communicates with the central node approximately 200 meters away.

As shown in Fig. 3.2.9 the architecture of an outlying node falls into three layers: a physical layer of physical devices, a network layer, and a control layer of software modules written in ASSEMBLER. The fabrication of both the physical layer and a half part of the network layer have been completed, but the control layer still under construction.

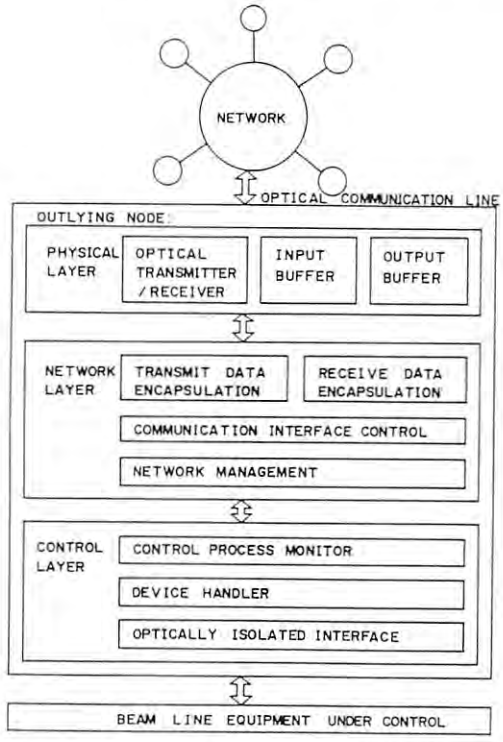

Fig. 3.2.9 Functional diagrams of an outlying node: There are three levels of layers.

The control process monitor's basic functions include:

1) Open or close a beam line on request from either the central node at the operation room, or synchrotron radiation users at the experimental hall.
2) Obtain and check status of valves/shutters on the beam line.
3) Get vacuum data from up to five points, so as to monitor the ultra high vacuum condition.
4) Get information on the safety interlocks of the beam line, as mentioned in the introduction.
5) Communicate with the network.
6) Get commands from the central node and execute them.
7) Transmit information on the current status of the beam line to the central node.
8) Diagnose an error when it occurs in the beam line and send the results to the central node.

Under normal conditions, the outlying node controls all components of the beam lines without central control intervention. When its control process monitor directly receives a Beam-Line-Open-Request (BLREQ) signal from the beam line users, the monitor in turn checks whether the status of the beam line satisfies desired conditions or not. If all conditions are met, the monitor then sequentially opens all the valves/shutters on the beam line. After completion of each opening, the monitor transmits the current status information to the central node via the network. When any one of the valves/shutters fails to open, the monitor closes all the valves/shutters, and invokes an error diagnosis process after sending error messages to the central node.

Figure 3.2.10 depicts the hardware architecture of an outlying node. To attain minimum cost and complexity, it consists of two printed circuit boards with microcomputer logic and a valve/shutter interface. A Zilog Z-80A CPU, parallel input/output interface and GPIB interface logic are implemented on the microcomputer logic board.

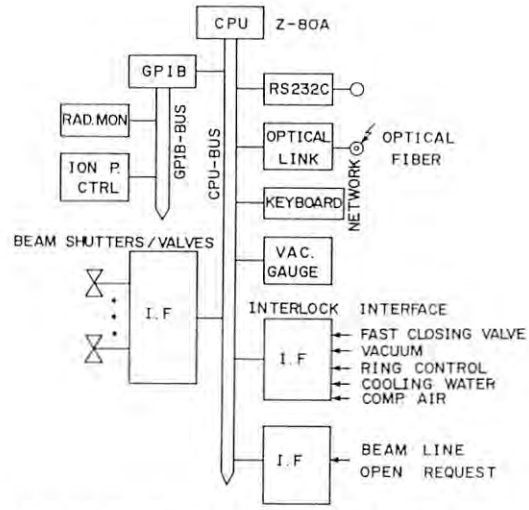

Fig. 3.2.10 Hardware architecture of outlying node by which complete control of a beam line is executed.

Central node

The central node consists of a DEC (Degital Equipment Corporation) LSI-11/23 microcomputer running RT-11 Operating System for control and monitoring beam lines, two microcomputer systems NEC PC-9800's with Intel 8086 for color graphic display, and a network controller with expandable communication ports for network management. The layout of the central node is illustrated in Fig. 3.2.11.

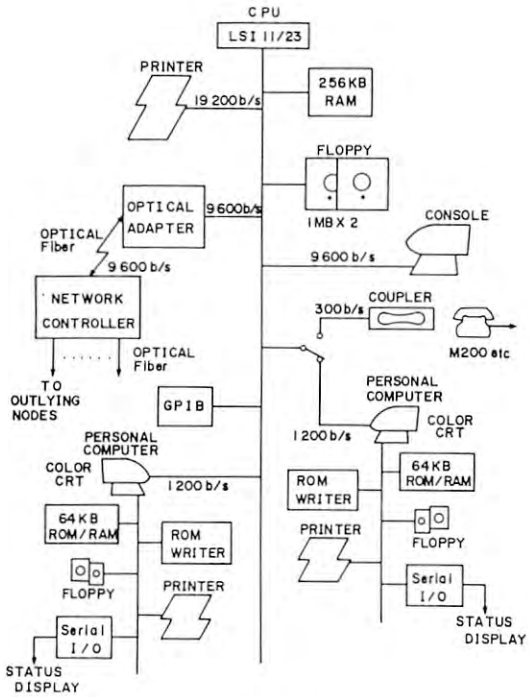

Fig. 3.2.11 Block diagram of the central node.

The central node carries out the process in accordance with the requirements 2) through 6).

The major part of the software programming (approximately 80%) for the central node is implemented in FORTRAN. The rest is written in ASSEMBLER, for reasons of time and memory space optimization. The whole software is fabricated in a number of modules so as to allow ease and flexibility in making changes. The software modules for the network access and operator-command analysis have been completed except for the system management.

Control information on the status of all beam lines is monitored at the central node via the network every minutes. This provides an advantage for detecting a temporary malfunction in the control system by checking whether one item of the status information is lost or not.

The current operational status of the beam lines is transmitted to a graphics microcomputer at the operation room. The PC-9800 microcomputers provide support for the graphics displays which have a resolution of 640 × 400 pixels with 8 color depth for graphic display and 80 × 25 color characters for alphanumeric display on a 14 inch CRT as shown in Fig. 3.2.12. The operators can select from several frames to obtain either an overview, or detailed report on specific areas of the status of the particular beam line. The software programming for color display is almost written in BASIC running on 8 MHz clock, and has been completed.

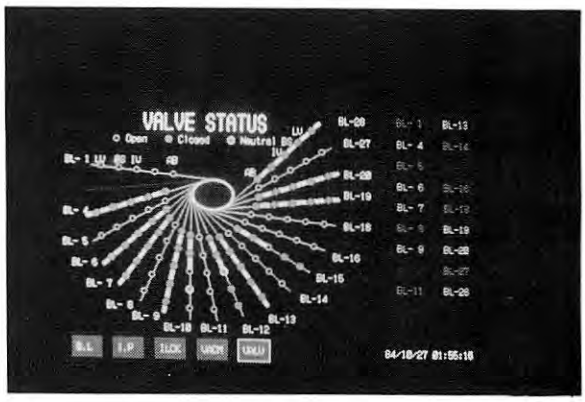

a)

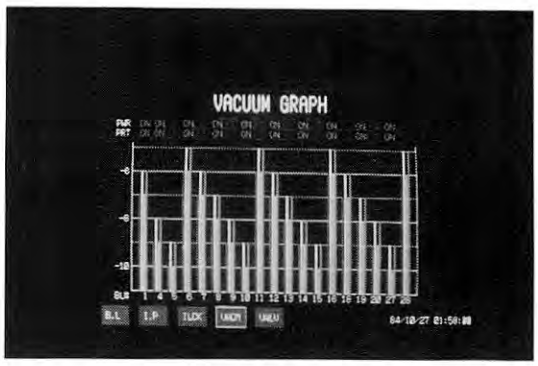

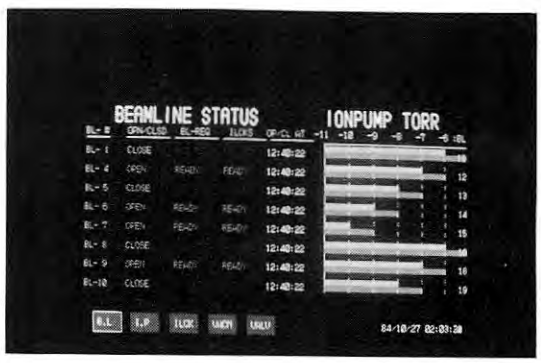

b)

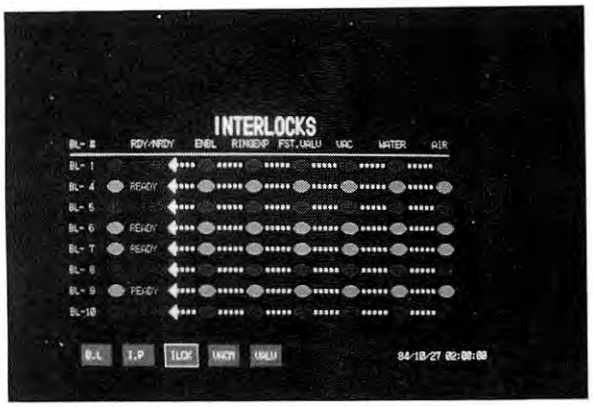

c)

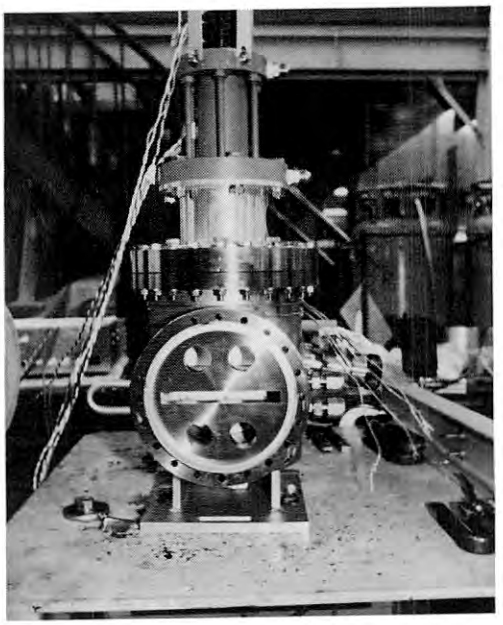

Fig. 3.2.12 Graphics display for a) valve status of all beam lines, b) vacuum and BL-REQ status, and c) interlocks (Ring, Fast-closing-valve, water, vacuum and air-pressure).

References

1) S. Sato, T. Koide, Y. Morioka, T. Ishii, H. Sugawara and I. Nagakura: Nucl. Instr. and Meth. 208 (1983) 31.
2) I. Nagakura: KEK Report KEK-81-17, 1982.
3) I. Nagakura: Private Communication.
4) T. Koide, S. Sato and N. Kanaya: Proc. 5th Symposium on Accelerator Science and Technology (KEK, 1984) p.175.
5) T. Koide, S. Sato, H. Fukutani, H. Noda, S. Suzuki, T. Hanyu, T. Miyahara, S. Nakai, I. Nagakura, A. Kakizaki, H. Maezawa, T. Ohta and T. Ishii: to be submitted to Nucl. Instr. and Meth.
6) N. Kanaya: IEEE Trans. on Nuclear Science, NS-31 (1984) 957.

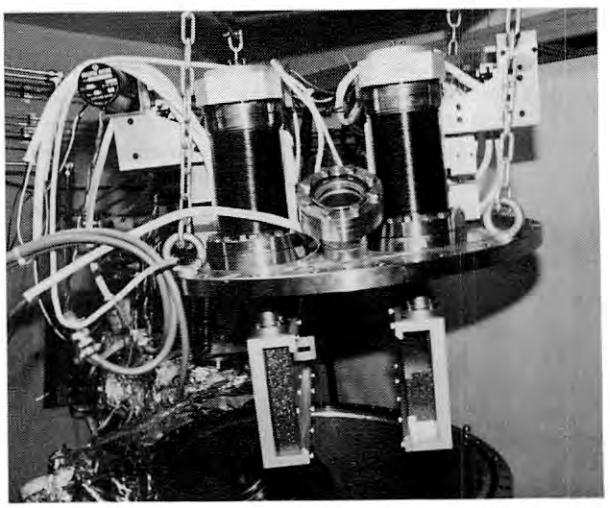

3.3 SINGLE-BUNCH OPERATION

Preparations for the SR experiments are progressing to use the single-bunch beam. In several traials of the single bunch operation, injection took place at every 1 second and charging rate was typically 0.1 mA/sec. At present, the Linac produces a train of many bunches spread over 1.5 ns. This pulse train is synchronized to the revolution frequency which is derived from the RF acceleration frequency f_{RF} divided by the harmonic number 312 and hence the bunch interval is 0.624 μs. The maximum stored current is 25 mA, which is limited by vacuum problem. The Viton gaskets are damaged by the bunch induced field in the gate valves. Vacuum pressure in the beam chamber gets worse at the location of the valves installed when the beam current exceeds 20 mA.

The metal gate valves with RF shield will be installed instead of the present gate valves in summer 1985.

Figure 3.3.1 shows a single bunch signal obtained from a pick-up electrode of the beam position monitor. This signal is shaped from originally bipolar pulse. Bunch length at the low beam current was observed as 200 ps (FWHM) by the streak camera. Number of electrons in the neighboring RF buckets seems quite few in this measurement as seen in Fig. 3.3.2.

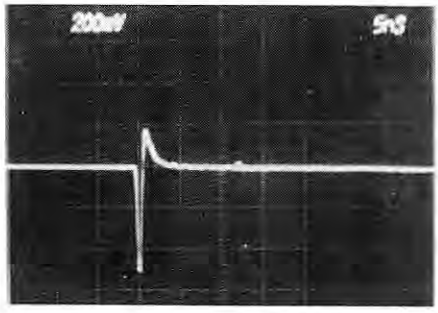

Fig. 3.3.1 Signal of the single bunch observed with a pick-up electrode of the beam position monitor.

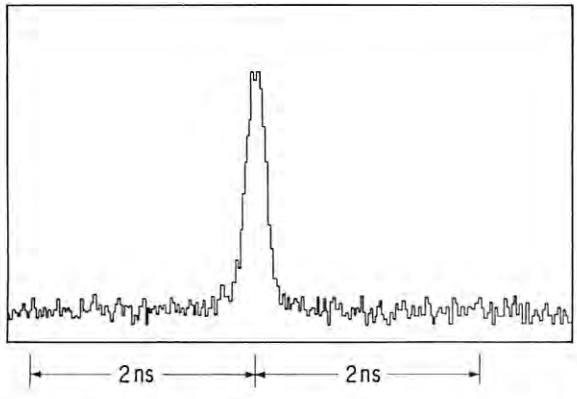

Fig. 3.3.2 Bunch length observed with the streak camera. Next RF buckets are 2 ns apart.

With negative chromaticities, we observed the head-tail instability caused by the low-Q impedances of the beam chambers. Here the chromaticities are defined as $\xi_{x,y} = \Delta\nu_{x,y}/(\Delta E/E)$ and can be changed by exciting the sextupole magnets. Without excitation of the sextupole magnets, the stored current was limited to 1 mA. Where the measured chromaticities ξ_x and ξ_y were -5.4 and -5.0, respectively.

One can cure the instability by correcting the chromaticities to zero or slightly positive; it means changing the phase relation of the betatron oscillation between head and tail of the bunch.

Threshold currents were measured by varing the chromaticities and results and shown in Fig. 3.3.3, where (a) is a ξ_y-dependence putting ξ_x = 0 and (b) is a ξ_x-dependence at ξ_y = 0. As seen from Fig. 3.3.3, the threshold of the vertical instability is approximately three times lower than the horizontal one. This can be interpreted by the difference of the impedances arising from the cross sectional shape of the beam pipe.

Dotted curve in the figure is a calculated one assuming the impedance $Z(\omega)$ as

$$Z(\omega) = \begin{cases} Z_o\omega/\omega_c & |\omega| \leq \omega_c \\ Z_o(\omega/\omega_c)^{-0.5} & |\omega| > \omega_c \end{cases}$$

Where, ω_c is assumed to be $2\pi \times 1.4$ GHz and Z_o is 2 kΩ. Simple calculation of the head-tail mode m = 0 cannot explain the experimental threshold currents except the order of magnitude.

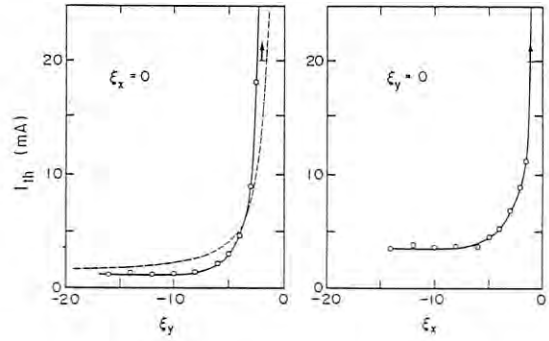

Fig. 3.3.3 Thresholds of the head-tail instability; (a) ξ_y-dependence at ξ_x = 0, (b) ξ_x-dependence at ξ_y = 0. Calculated values are illustrated with a dotted curve.

4. FUTURE IMPROVEMENTS

Realignment of quadrupole magnets: The construction of a large building for TRISTAN was finished, but it gave a mis-alignment of Q-magnets and, inevitably, gave a closed orbit distortion of order of 4 mm. This distortion was corrected by using steering magnets, however, it will become difficult to give the correct light axis to every beam channel when the number of channels will increase. Accordingly, the realignment of Q-magnets must be done when the ground is settled stably.

Improvement of cooling system for vacuum chamber: At the operation of beam currents higher than 200 mA, leaks sometimes occurres in flanges heated up by the irradiation of SR. Therefore the maximum current during the service running of the ring is limited under 150 mA. In order to increase the stored current, about fifty copper or aluminum blocks will be inserted into the vacuum chamber for absorbing SR power during summer shutdown in 1985. This improvement can accommodate the vacuum chamber to 3 GeV operation in which the SR power is twice that of present 2.5 GeV operation.

All metal gate valve: The present gate valves have Viton gaskets. In the single bunch operation, strong wake fields heat Viton gaskets and give a high vacuum pressure, which limits the stored current less than 20 mA. So these valves will be changed by all metal gate valves with RF shields.

Water cooling system for cavities: Coupled bunch instabilities are very sensitive to the temperature of cavities. A new water cooling system will finely control the temperature of each cavity independently.

Higher order mode damper: To cure coupled bunch instabilities, higher order mode dampers will be inserted into each cavity. Now, two damping antennas were built, and the test with RF power of 60 kW is progressing.

Octupole magnet: For instabilities, the origin of which is not know, octupole magnets are useful to make Landau damping.

V. INSTRUMATATION DIVISION

The construction and adjustment of the apparatuses which had been planned as the first stage project of the instrumatation devision was almost completed in July, 1984. Most of the apparatuses are now open to general use. The description is presented below which mainly covers the beam lines or related apparatuses newly build or greatly improved after the publication of the former report (Activity Report 82/83). The short summary is also given which describes the main features of the existing beam lines, monochromator and the operating apparatuses.

The number of visiting users and the experimental programs has increased so rapidly that the present report includes about 50 % more users' short reports than the former report. Among those not a few scientists coming from commercial companies has made considerable contributions.

Drastic increase in financial support by the Government or possibly by commercial companies is strongly required for the facility to match users' increasing activities.

Beam lines and Optics

During the period from October 1983 to September 1984, the vertical wiggler beam line became operational. Commissioning of a new type of double crystal monochromator and a focusing mirror has successfully been made on BL-14A. BL-14B has been operated as a white X-ray station. In the summer of 1984, a double crystal monochromator has been installed on this beam line. This monochromator was designed in such a way that switching from monochromatic X-ray mode to white X-ray mode can be made easily. For BL-14C, a double crystal monochromator of essentially the same design as those for BL-14A and BL-14B has been ordered.

Efforts have also been made to install monochromators on the existing white X-ray branch lines stretching from the bending magnets. A new type of double crystal monochromator has been constructed and installed on BL-4C. Test operation of this monochromator started July, 1984. A conventional double crystal monochromator to be installed on BL-4B is being designed.

Beam Line 2

After the completion of the undulator beam line, BL-2, we encountered a serious problem on its operation; a background level of γ-ray was too high to make the beam line open to potential users of the undulator radiation (UR). The γ-ray observed was the bremsstrahlung due to collisions of the beam electrons with the residual gas atoms in the storage ring. It was strong because the axis of the γ-ray perfectly coincides with that of the UR and its divergence is as small as that of the UR. The problem of the existence of strong γ-ray background is thought to be inevitable, since the electrons in the undulator pass through a long straight section of the ring, which is 5 m long for the PF-undulator.

As a solution for this problem, we have modified the beam line so as to deflect the UR by a mirror, by which the axis of the UR can be separated from that of the γ-ray. A layout of this newly reconstructed beam line is schematically given in Fig. 5.1. The mirror is made of platinum coated silicon carbide and the glancing angle is 2°. As a result, we now have two branch beam lines; one is the deflected branch and the other is the direct branch. The direct branch can be opened by lifting the mirror away from the undulator axis. Time sharing will be employed to utilize the two branches.

The deflected branch is served mainly for utilizing the first order harmonic of the UR, which can be tuned to cover the soft x-ray region from 400 eV to about 900 eV. To escape from a direct irradiation of the γ-ray in the direct branch, we adopted a combination of a simple channel-cut double reflection crystal monochromator made of beryl, InSb etc. with a 50 cm long lead pipe, the idea of which is shown schematically in Fig. 5.2. Consequently, only the higher order harmonics over 1 KeV region are available at present in the direct branch.

With other improvements made on this beam line, that is, the completion of the vacuum interlock system and the remote adjustment control system of pinhole diaphragms and the deflection mirror, the undulator radiation beam line is now become ready to be open to many potential users.

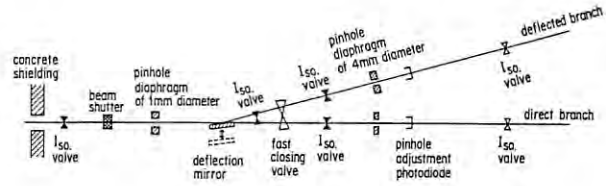

Fig. 5.1 A layout of the newly reconstructed undulator radiation beam line, BL-2.

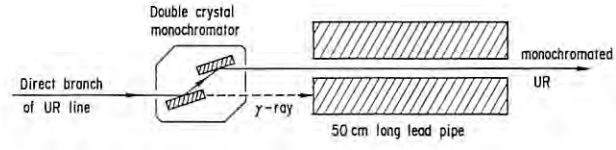

Fig. 5.2 Schematic drawing of the idea for the γ-ray shielding in direct branch of the undulator radiation beam line, BL-2.

Beam Line 4C

The double crystal monochromator installed on this branch beam line is designed to give a constant beam height(25 mm above the incident beam) of the reflected beam for Bragg angles through 5° to 70°. This angle range corresponds to an energy range from 2.1 KeV to 22.6 KeV if the lattice spacing of silicon (111) is simply assumed. The mechanism of the monochromator is schematically shown in Fig. 5.3. Two crystals are mounted on a circular table and rotate together for changing the incident angle of the X-ray beam. The first crystal, which is mounted on a water cooled copper block, sits on X- and Y-translation stages. The second crystal is located just on the rotating axis of the table. The translation of the first crystal is controlled by two mechanical cams as a function of the rotation angle. The shapes of two translation guides are figured in such a way that the X-ray beam is successively reflected by two crystals with constant beam height deviation. If the translation mechanism is precise enough, the parallelism between the first and the second crystals is always kept. The second crystal holder is designed to hold and bend a diamond shaped crystal to realize sagittal focusing of the beam. The monochromator chamber and the beam transport is evacuated to a low vacuum which is separated by two serial berylium windows from ultra high vacuum of the storage ring.

Test operation of this monochromator was made in July 1984 using two flat crystals of Si(111). We found that the successively reflected beam was always observed on a phospher screen in a vacuum for Bragg angle from 5° to 68° with a slight intensity modulation without any feedback to the first crystal. Furthermore, we were able to keep the intensity of the successively reflected beam higher than 90% of the peak of the rocking curve with a computerized feedback system. Beam height deviation was checked at a sample position which is approximately 7 m from the monochromator for an angle range from 6° to 30°. The beam height gradually changed by ∿0.3 mm in the angle range from 6° to 16°. This came from the inaccurate figure of the Y-translation guide which control the translation of the first crystal in the direction normal to the crystal surface. This problem will be solved by refiguring the surface of the translation guide.

A diamond shaped crystal with many fine slots is now prepared. Test of this crystal for sagittal focusing will be made soon.

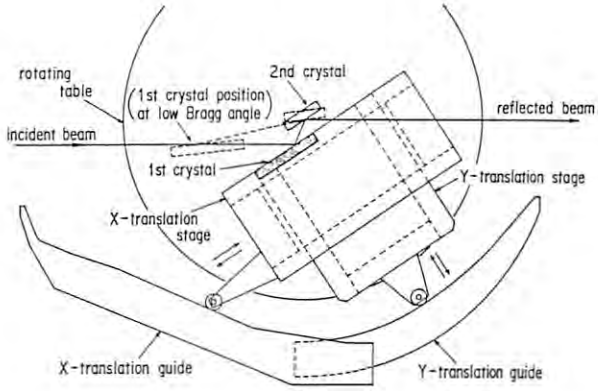

Fig. 5.3 Mechanism of the monochromator.

Beam Line 14A

The commissioning of the optics has successfully been made on this branch beam line. A vertically divergent beam from the vertical wiggler is accepted by a double crystal monochromator followed by a bent cylindrical mirror. Preliminary EXAFS measurements at high energies and crystal structural studies using a horizontal-type four circle diffractometer have been initiated.

The top view of the double crystal monochromator is shown in Fig. 5.4.

Two flat crystals of Si(111) or (331) are used. The first crystal is mounted on a water-cooled crystal holder and can be rotated around an axis θ_1. The second crystal is mounted on a goniometer (θ_2 rotation) which can be translated along a 1.7 m long translation stage. The separation between the incident beam and doubly reflected beam is designed to be 45 cm in order to keep space enough for installing a four-circle diffractometer downstream of this branch line. The three motions of the two crystals are synchronously controlled so that the position and direction of the reflected beam is always kept constant. We found that the beam position is kept constant through energy range from 5 KeV to 20 KeV with Si(111) crystals and from 13 KeV to 48 KeV with Si(331) crystals.

The beam condensing mirror is placed 15.5 m from the source. It consists of two 50 cm long cylindrically polished mirrors coated with platinum. The two mirrors are clumped to a 1 m long H-shaped steel beam, and this H-shaped beam is bent to give a uniform bending of the mirrors. The glancing angle of the X-ray beam was set at 5 mrad, which results in an available energy range of the X-ray beam to be 5 KeV to 20 KeV. We observed a beam spot of 1.2 mm(H) × 0.5 mm(V) at the position 31 m from the source. This enhanced the intensity at the sample position by a factor of 15. The mirror can easily be removed from the beam path for the experiments which need X-ray energies higher than 20 KeV.

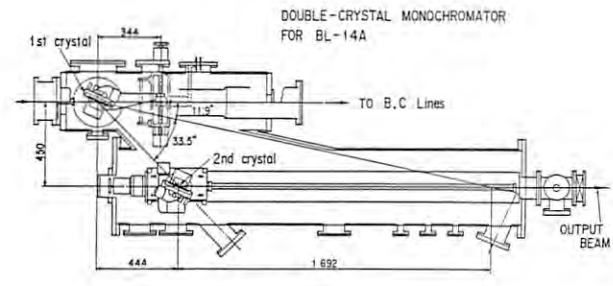

Fig. 5.4 Top view of double crystal monochromator.

NTT(Nippon Telegraph and Telephone) Beam line

Beam Line 1

BL-1 is designed for analyses of materials and studies of lithography and several photo-chemical reactions using soft X-ray and VUV beams. The BL-1 consists of a front end, a beam splitting section and three branch lines, 1A, 1B and 1C.

The design and construction of BL-1 were carried out by the Electrical Communication Laboratories division, N.T.T. in cooperation with KEK-PF. The layout of three branch beam lines is shown schematically in Fig. 5.5.

BL-1A BL-1A is designed to perform measurements of photoemmision and SEXAFS for surface structure analysis. The components of this beam line for obtaining a focused monochromatic beam in the soft X-ray and VUV region includes an ultrahigh vacuum scanning monochromator using gratings and crystals (Grating/Crystal Monochromator : GCM), a collimating off-axis paraboloidal mirror in front of the monochromator and a focusing off-axis paraboloidal mirror in the rear of the monochromator. The front mirror of 17 m focal distance located 17 m downstream from the source deflects the direct beam of 4 mrad horizontal × 1 mrad vertical acceptance upward by 2°. The rear mirror of 10 m focal distance located 25 m downstream deflects the monochromatic beam downward by 2° and focuses it at the 35 m point from the source. Figure 5.6 shows views of Grating/crystal Monochromator and the scanning mechanism in the chamber. This monochromator will be installed between the above two mirrors after completing the computer control system.

BL-1B BL-1B is a branch line for the study of X-ray lithography. Synchrotron radiation wavelength is selected by SiC plane mirror and X-ray filter (e.g. Be foil), and then 0.7 - 1.2 nm wavelengths are used. The branch line can be moved mechanically so that the mirror horizontally deflect the beam by 2 - 4°. The beam acceptance is 1.2 mrad^{h} × 4 mrad^{v}. At the end of BL-1B, an exposure apparatus is installed, which enables experiments on pattern replication using synchrotron radiation. The vacuum in this chamber is separated from that of the branch line by a 10 μm thick Be foil. The apparatus is located 30 m downstream from the source point.

BL-1C BL-1C is a VUV line designed for the investigation of several photo-chemical reactions. The beam is deflected by 8° using a toroidal mirror with a horizontal acceptance of 2 mrad. This beam line is designed to allow a large difference of vacuum pressure between upper and lower streams by a vacuum differential pumping. The gas pressure in the experimental chamber can be increased up to about 0.1 Torr.

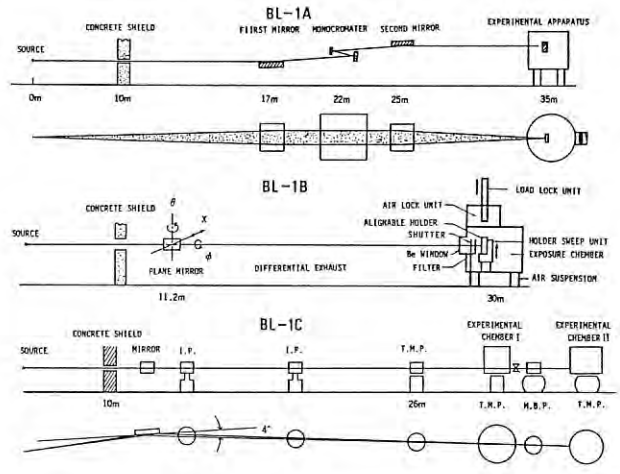

Fig. 5.5 Layout of three branch beam lines.

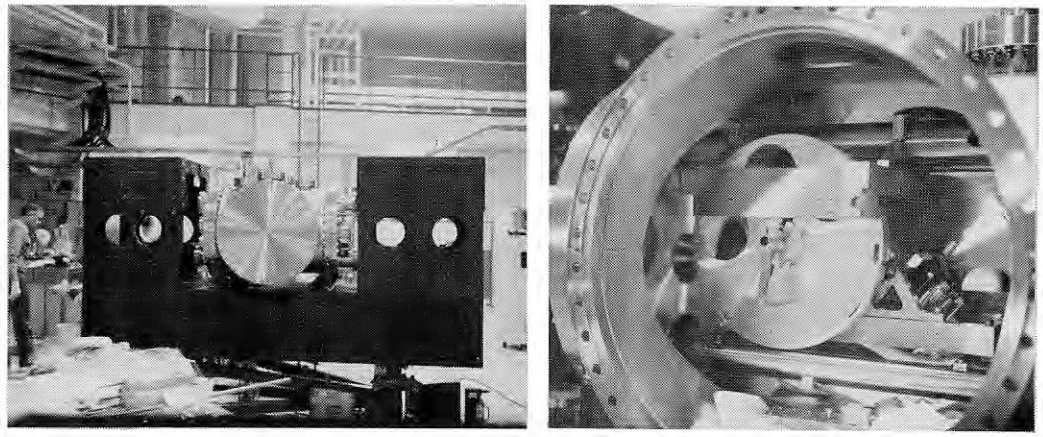

Fig. 5.6 Views of grating/crystal monochromator and the scanning mechanisms in the chamber.

Summary of X-ray Beam Lines and Optics

Beam Line	Horizontal Acceptance Angle (mrad)	Typical Beam Spot Size (H mm × V mm)	Photon Flux at Sample Position	Monochromator (Crystal)	Energy resolution ($\Delta E/E$)	Energy range (KeV)	Mirror	Line Vacuum (Gas)
4A	6	50 × 5		none	white radiation	4 - 35	none	Vacuum
4B	4.5	50 × 5		none	white radiation	4 - 35	none	Vacuum
4C	4	50 × 5		double crystal Si (111) (sagittal focusing being prepared)	$\sim 2 \times 10^{-4}$	4 - 20	none	Vacuum
10A	1	10 × 3	1×10^{9} at 10 KeV with flat Si (111)	Silicon (111) Germanium (111) Pyrolytic graphite (002) Curved Si (111) (α 8°)	5×10^{-3} $\sim 5 \times 10^{-4}$	6.5 ∿ 25	none	Helium
10B	2	8 × 1	3×10^{8} at 10 KeV with Si (311)	Channel-cut Si (311) Double Si (111) Double Si (220)	1×10^{-4}	6 ∿ 30 3.5 ∿ 15 5.5 ∿ 25	none	Vacuum
10C	4	6 × 1.5	$\sim 10^{10}$ at ∿ 8 KeV	double crystal Si (111) fixed beam position	$2 \sim 10^{-4}$	4 ∿ 10	bent cylinder	Helium
14A	1.28	5 × 38		Double Si (111) Double Si (331) Double Si (551)	2×10^{-4}	5.1 ∿ 19.1 12.9 ∿ 48 21.1 ∿ 78.6	Bent Cylinder for Vertical Focusing, Pt-coated fused quartz	Vacuum (line) He(mono-chromator)
14B	2.2	5 × 30		Double Si (111) Double Si (220) Double Si (311)	2×10^{-4}	5.2 ∿ 57	Saggital focusing	Vacuum
14C	1.3	10 × 40		Double Si (111)	2×10^{-4}	5.5 ∿ 43	none	Vacuum
15A	2	2.6 × 1.3	1×10^{10} at 8.3 KeV	Curved Si (111) (α=7.8°)	$\sim 10^{-2}$	5.6 ∿ 12.4	Cylinder, fused quartz	Vacuum and He
15B	0.14	5 × 5	3×10^{4} at 10.5 KeV	Channel cut fixed exit channel cut Double crystal	7×10^{-4} 7×10^{-4} 1.5×10^{-3}	10.0 - 34.0 3.5 - 16.0	none	Vacuum
15C	2	60 × 6	White			4 ∿ 35	none	Vacuum

Summary of VUV/Soft X-ray beam lines and optics

BRANCH BEAM LINES	Monochromator	Grating (Crystal)	Groove density (ℓ/mm)	Blaze (A)	Resolution	Wavelength range (A)	PRE - MIRRORS Type	Radius of curvature (mm)	Angle of incidence	Material	Coating Material	Dimensions (mm)	Horizontal & Vertical acceptance (mrad)	REFOCUSING MIRRORS Type	Radius of curvature (mm)	Angle of incidence	Material	Coating Material	Dimensions (mm)	Beam Size (mm)
B1-A	Grating/Crystal Monochromator	Au-coated original InSb(111) Si(111)	2400		E/ΔE ∿ 2000	2 ∿ 2000	Parabol-oidal		89°	Fused Quartz			$4.0^{h}\times1.0^{v}$	Parabol-oidal		89°	Fuzed Quartz			
B1-B	Filtered white						Plane		88° ∿ 89°	SiC			$1.2^{h}\times4.0^{v}$						19 mmϕ	
B1-C	Filtered white						Toroidal		86°	Fused Quartz	Pt		$2.0^{h}\times4.0^{v}$						$2^{h}\times10^{v}$	
B2-A	White/2m grazing incidence (85°)	Hitachi Au-coated replica	2400	30	Δλ=0.02 A for 10μ-10μ slits	30 ∿ 200	Plane	———	88°	SiC	Pt	$120^{\ell}\times60^{w}\times15^{t}$	———							
B2-B	Channel-cut double crystal	Beryl(10$\bar{1}$0) InSb(111)	2d=15.9 A 2d=7.4806 A	———		8 ∿ 16 3 ∿ 8	———	———	———	———	———	———	———							
B11-A (2GH)	Grasshopper Mark VII 2m grazing incidence Fixed incidence angle of 88°	Hitachi Au-coated replica (pyrex)	2400 1200	16.6 33.3	Δλ=0.02 A Δλ=0.04 A for 10μ-10μ slits	10 ∿ 145 10 ∿ 290	Spherical Spherical	360000 28000	88° 88°	Fused Quartz Fused Quartz	Pt Au	$400^{\ell}\times170^{w}\times40^{t}$ 300^{ℓ}	$1.3^{h}\times0.4^{v}$	Benting Cylinder	R∿3000	89°	Pyrex	Pt	$220^{\ell}\times24^{w}\times6^{t}$	$8^{h}\times0.3^{v}$
B11-B (DXM)	Jumbo Jr. Double crystal monochromator	Ge(111) InSb(111) Beryl(10$\bar{1}$0)	2d=6.53 A 2d=7.4806 A 2d=15.9 A		ΔE=1eV at 2KeV ΔE=0.8eV at 2KeV ΔE=0.6eV at 1KeV	2.7 ∿ 6.2 3 ∿ 7 8 ∿ 16	Bending Cylinder	ρ=300 R∿950000	89°	Fused Quartz	Pt	$580^{\ell}\times140^{w}\times30^{t}$	$4.0^{h}\times0.6^{v}$							$8^{h}\times1^{v}$
B11-C (SSN)	1m Seya-Namioka Constant deviation of 70°	B & L Au-coated replica	2400 1200	694 1300	λ/Δλ=2000 ∿ 3000	400 ∿ 1700 400 ∿ 3500	Plane Concave	——— 5600	77.5° 42.5°	SiC Fused Quartz	none Pt	$250^{\ell}\times100^{w}\times40^{t}$ $100^{\ell}\times100^{\ell}\times20^{t}$	$4.8^{h}\times3.0^{v}$	Toroidal	ρ=2000 R=125	72.5°	Pyrex	Au	$90^{\ell}\times50^{w}\times10^{t}$	∿1ϕ
B11-D (CDM)	2m-grazing incidence constant deviation monochromator α + β = 154°	B & L Au-coated replica	2400 1200 600	32 116 460	λ/Δλ ∿ 1700 for 25μ-25μ slits	80 ∿ 150 120 ∿ 300 240 ∿ 600	Cylindrical Plane Concave	ρ=750 ——— 4000	86° 86° 86°	SiC Fused Quartz BK-7	Pt Au Au	$400^{\ell}\times60^{w}\times40^{t}$ $50^{\ell}\times40^{w}\times10^{t}$ $50^{\ell}\times40^{w}\times10^{t}$	$2.0^{h}\times2.0^{v}$	Toroidal	ρ=400 R=3100	77°	BK-7	Au	$60^{\ell}\times40^{w}\times10^{t}$	$0.5^{h}\times0.5^{v}$
B12-A (GSN)	1m Seya-Namioka Constant deviation of 70°	B & L Au-coated replica	2400 1200	508 536	Δλ=0.4 A at 500 A for 100μ-100μ slits	350 ∿ 1000 350 ∿ 2000	Plane Concave	——— 6250	80° 45°	SiC Fused Quartz	none Pt	$250^{\ell}\times200^{w}\times40^{t}$ $100^{\ell}\times20^{t}$	$2.4^{h}\times1.5^{v}$	Plane Toroidal Plane	——— ρ=340 R=2000 ———	80° 70° 80°	Pyrex Pyrex Pyrex	Pt Pt Pt	$40^{\ell}\times40^{w}\times10^{t}$ $40^{\ell}\times40^{w}\times10^{t}$ $40^{\ell}\times40^{w}\times10^{t}$	∿1ϕ
B12-B (6VOPE)	6.65m normal incidence off-plane Eagle mounting	B & L Au-coated replica	1200 1200	1500 5500	Δλ=0.003 A at 500 A for 11th order	400 ∿ 2500	Plane Concave* Concave*	——— 4321 2188.5	80° 35° 45°	SiC Pyrex Pyrex	none Pt Pt	$280^{\ell}\times100^{w}\times40^{t}$ $110^{\ell}\times20^{t}$ $110^{\ell}\times20^{t}$	$5.0^{h}\times3.6^{v}$							
B12-C (10GIM)	10m grazing incidence Fixed incidence angle of 89°	Hitachi Au-coated replica (pyrex)	2400 1200	9.5 10.9	Δλ=0.002 A Δλ-0.004 A for 5μ-5μ slits	6 ∿ 25 6 ∿ 50	Plane Concave Concave	——— 8903 7527	86.85°∿ 88.83° 89° 89°	SiC Pyrex Pyrex	Pt Pt Pt	$120^{\ell}\times60^{w}\times15^{t}$ $90^{\ell}\times15^{t}$ $90^{\ell}\times15^{t}$	$0.14^{h}\times0.4^{v}$							

Apparatuses

Weissenberg camera for macromolecular crystallography

This Weissenberg camera has been designed and constructed for recording many reflections with high resolution on a film with high signal-to-background ratio from a crystal with large unit cell dimensions (N. Sakabe, J. Appl. Cryst. (1983) 16 542-547). Multi-layer-line screens are used to suppress the increment of background with the enlargement of the oscillation range. Because the camera does not have the apparatus for the alignment of a crystal axis with it, it is necessary to align a crystal axis by other method whenever the screen is used.

The camera is not fixed to any definite hutch, it can be used on BL-4B or BL-15A2.

A horizontal view of the goniometer is shown in Fig. 5.7, and the specification of three film cassettes are summarized in Table 1. The film cassette #3 can be used for the measurement of the polarization of a beam with a powder sample at a special condition.

The maximum span for the translation of the film cassette is 50 mm. Two stepping motors are used for the translation of the film cassette and for the rotation of the specimen respectively. The speeds of the translation and the rotation are controlled independently so that one can change the coupling constant between the speeds of the two motors by selection of preferred speeds of the two motors.

The multi-layer-line screens are effective for the separation of diffracted beam from background. When using an X-ray with a definite wavelength, it is necessary to change the positions of the slits for different crystals since the width between two adjacent layers is different in each crystal; it is necessary to provide a new screen according to the spacing of the crystal rotation axis. For the multi-layer-line screens designed, the central position Xn of the nth-layer-line slit from the central position of the equator and its width dn, Xn can be evaluated from the relation

$$Xn = \frac{rs}{\{(a/n\lambda)^2-1\}^{1/2}},$$

where rs is the radius of the screen, λ is the wavelength and a is the spacing of the crystal rotation axis. dn is estimated as the summation of five terms which are related to the diffracted beam size on the screen ℓs, the thickness of the screen t, the error of the alignment ϕ, the change of the spacing of the crystal rotation axis $\Delta a/a$, and the band pass $\Delta\lambda/\lambda$, and is given by

$$d_o = \ell s + 4rs \tan\phi \sin\theta \max + \varepsilon$$

for n = 0 and

$$dn = \ell s + \frac{t}{(A^2-1)^{1/2}} + 4\, rs \tan\phi \sin\theta \max + \left[\frac{A}{(A^2-1)^{1/2}}\right]^3 \frac{1}{A}\, rs \left(\frac{\Delta a}{a} + \frac{\Delta\lambda}{\lambda}\right) + \varepsilon$$

for n = 0, where θ max is θ at the maximum resolution and A is equal to $a/n\lambda$. An example of multi-layer-line screens is shown in Fig. 5.8.

Table 1 Specification of Film Cassette

Film cassette	Radius	Effective width	Range for recording 2θ max	2θ min
1	286.5 mm	280 mm	162°	-41°
2	143.5	200	170	-170
3	86.0	150	170	-170

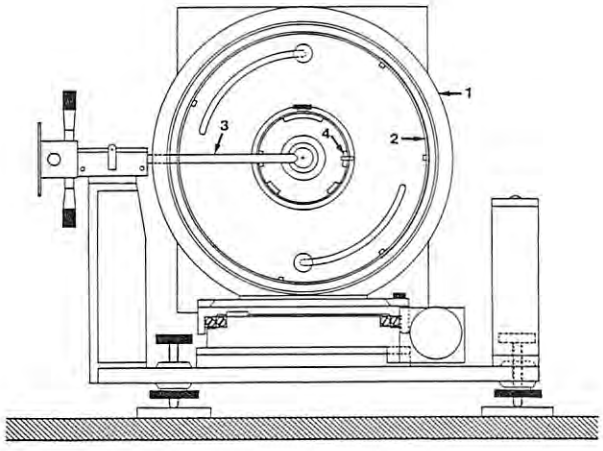

Fig. 5.7 Side view of the Weissenberg goniometer
1. film cassete; 2. multi-layer-line screen; 3. colimator; 4. beam stopper.

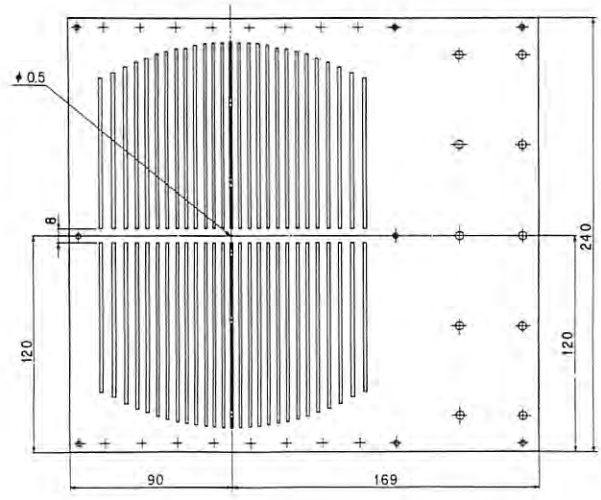

Fig. 5.8 Example of a multi-layer-line screen.

A DIFFRACTOMETER FOR GASEOUS SAMPLES

A diffractometer for gaseous sample was constructed. This diffractometer allows charge density studies of free molecules or atoms and structural studies of gas phase molecules. The diffractometer is essentially an $\omega - 2\theta$ horizontal-type two-circle diffractometer on which a $\chi - \phi$ circle can be mounted in order to use this whole set as a four-circle system, as shown in Fig. 5.9. It was designed both for energy-dispersive measurements with white X-rays and for angle-dispersive measurements with monochromatized X-rays. Scattered photons from gas sample are accumulated by a pure-Ge SSD linked to a multichannel pulse height analyzer. The diffractometer and detector systems are controlled by a micro-computer system (FDPS30A). Two types of gas sample cells have been prepared; A: A cylindrical cell made of stainless steel with the inner diameter of 60 mm. This cell is designed for pressure tight experiments (usable maximum pressure is 10 kg/cm^2 in absolute pressure); B: A cylindrical cell made of brass which has a glass-made boiling system. This cell is designed for experiments on liquid samples at room temperature. Its inner diameter is also 60 mm. The whole cell system are wrapped by a heating wire and can be warmed up to roughly 200 °C. The schematic drawings of these cells are shown in Figures 5.10 and 5.11.

Some experimental results obtained by using this diffractometer are reported elsewhere in this volume.

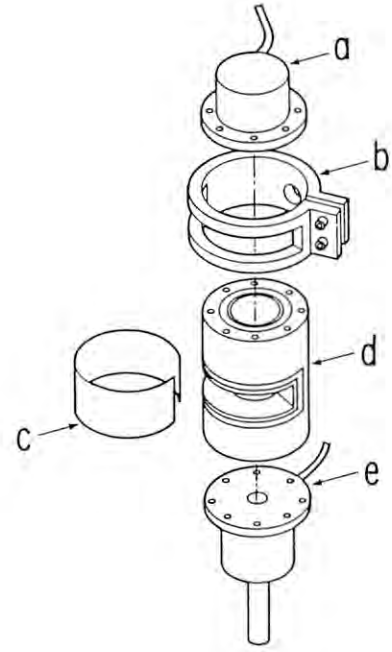

Fig. 5.10 An exploded diagram of a sample cell (A)
a: gas inlet
b: clamp for a kapton window
c: kapton window
d: scattering chamber
e: gas outlet

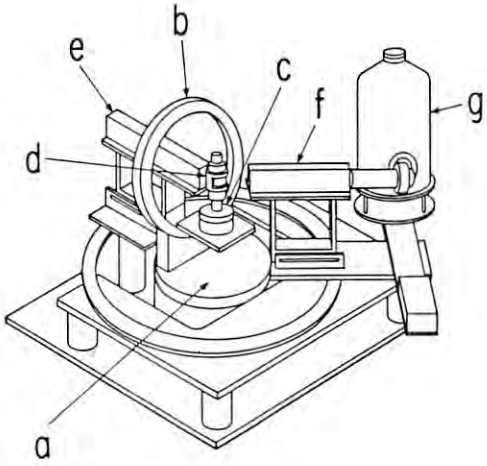

Fig. 5.9 A schematic drawing of the diffractometer
a: $\omega - 2\theta$ two-circle goniometer
b,c: $\chi - \phi$ circle
d: sample cell
e: collimator
f: analyzer collimator
g: SSD

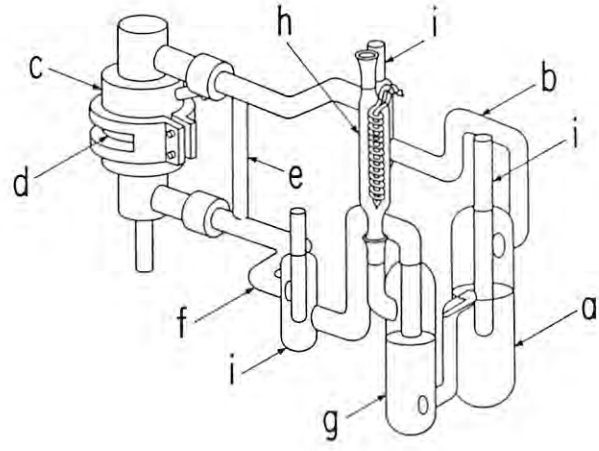

Fig. 5.11 Schematic drawing of a sample cell (B) and a flow-system.
(a) boiler;
(b) upper chimney;
(c) sample cell;
(d) window for scattered X-rays;
(e) stem;
(f) lower chimney;
(g) reservoir of the sample;
(h) condenser;
(i) thermometer port.

Apparatus for SEXAFS Experiments

Figures 5.12, 5.13, and 5.14 illustrate an experimental system designed to perform surface EXAFS (SEXAFS) on well-characterized solid surfaces. Although the system is not complete and further design and construction of components is continuing, enough of the system is now operating that beamline tests and preparations for the initial experiments have begun.

In figure 5.12, the overall system is illustrated. It basically consists of an ultra-high vacuum (UHV) chamber, shown in the center of the figure, and supporting electronics and an auxiliary pumping station. The entire system is mobile, and can be installed at a number of PF beamlines in less than 4 hours, altogether. The main vacuum chamber is supported on the beamline using a kinematic baseplate system, which permits precise alignment to be performed quickly and easily.

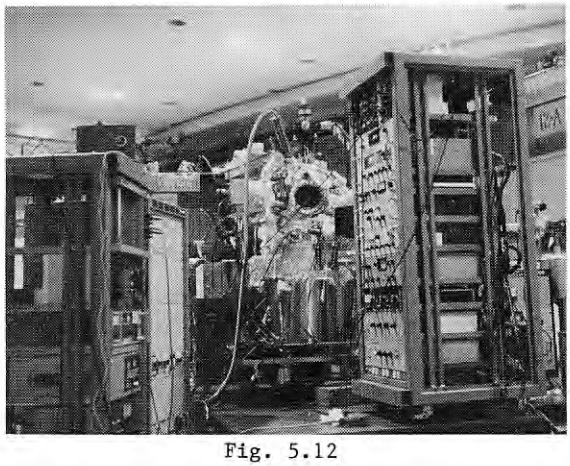

Fig. 5.12

Since well-characterized surfaces are crucial for obtaining meaningful results from a SEXAFS experiment, tools for surface cleaning, preparation, and characterization are included in the system, i.e, a 5 keV ion gun, pure gases (CO, H_2, O_2, Ar and H_2S), a quadrupole residual gas analyzer, (RGA) low energy electron diffraction (LEED) optics, heating-cooling sample manipulator, and a double-pass cylindrical-mirror electron analyzer (CMA) with 5 keV electron gun and twin anode (Mg and Al) X-ray source for performing Auger electron spectroscopy (AES) and X-ray photo electron spectroscopy (XPS). In addition to these, an evaporator system, a sample cleaver, and a sample transfer system may be added in the future.

The SEXAFS experiments can be performed using a variety of detection schemes, Auger electron yield, total or partial electron yield, and through photon stimulated ion desorption (PSD), to name a few. At present, the CMA can be used for Auger yield detection while a combination time-of-flight PSD/electron yield detector is now being designed.

Figures 5.13 and 5.14 illustrate the inside of the UHV chamber. Basically, the chamber is organized as a 2 level system. The upper level includes equipment which will utilize synchrotron radiation (SR) photons, while the lower level holds other non-photon-utilizing devices. The samples are mounted at a radius of 50 mm from the main vertical centerline of the chamber. The sample manipulator rotation about this centerline positions the samples at one of several analysis stations, located both on the upper and lower levels around the chamber. In figure 5.13, a Ni(110) single crystal (NI), mounted on the sample manipulator, appears in the center of the figure. As shown, the sample is between the upper and lower analysis levels. The LEED optics can be seen in the backround.

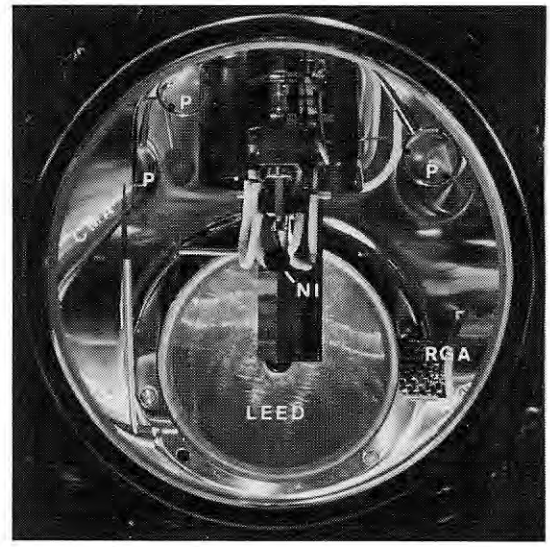

Fig. 5.13

Fig. 5.14

The LEED optics and a station including the RGA and ion gun are located on the lower level. The tip of the RGA can be seen in the lower right of figure 5.13. The upper level includes two analyses stations utilizing SR photons. One station comprises the CMA, the 5keV electron gun, and the twin anode X-ray source. This

station is seen in the upper left of figure 5.13 and in figure 5.14, where the electron gun (E^-) and X-ray source (X) are also visible. The other station will house the PSD/electron yield detector. The port for SR photons (Hv) is indicated in figure C and the small phosphor screens used for alignment (P) and the CMA shutter (S) are also indicated.

The sample manipulator was completed in late June, 1984 and beam tests of the system components made in the July run. Sulfur was diffused out of the bulk of the Ni(110) crystal by heating, and the CMA used to take photoelectron spectra of several Ni and S core levels and to record test SEXAFS spectra, using Auger yield, of the S K edge. Preparations for SEXAFS experiments on well-characterized ordered S overlayers on Ni (110) are now under way.

Apparatus for ARPES experiments for solid state

This apparatus is mainly used for angle--resolved photoelectron spectroscopy for solid state, and has some equipments for sample preparation and characterization besides two different types of electron energy analyzers. This is only for a constant deviation monochromator (CDM) installed at BL-11D considering the weight and the incident beam height, but it is easy to remove and attach riding on a rail. Figures 5.15 and 5.16 show outside views of the apparatus. This consists of a sample preparation chamber, an analysis chamber, a sample transfer system and so on.

In general, samples are treated in the sample preparation chamber which is equipped with a sample bank, a single wedge type of cleaving system and a 2 KW evaporation system with a thickness monitor. The sample bank is able to store five samples mounted on special holders. It seems easy to prepare evaporation films of various alloys, since there is enough room for another two evaporation guns in the chamber. The rest several free ports are available for user's devices.

The sample transfer system transfers a sample at the sample bank to a manipulator with a heating and cooling attachment in the analysis chamber. Further, this system may be used instead of the manipulator, because it has a temperature control system (-170∿900°C) and various precision mechanisms of sample translation, rotation and tilt.

The prepared sample mounted on the manipulator is estimated in the analysis chamber using characterization techniques such as Auger electron spectroscopy (AES), low energy electron diffraction (LEED) and secondary ion mass spectroscopy (SIMS). Therefore, the chamber is a two level system and it has a 5 KV sputter ion gun, a quadrupole mass filter and a 4-grids LEED optics at the upper level and a double-pass cylindrical mirror analyzer (DCMA) at the lower level. Both LEED optics and DCMA are not obstructive of another measurement for their attached translator. Photoemission measurements are performed at the lower level mainly using a 150° hemispherical analyzer mounted on a two axis rotational mechanism, which is able to rotate 23°∿300° (horizontal) and 0°∿ 90° (vertical). The angle resolution and energy resolution of this analyzer are approximately ±1° and 100, respectively, with a slit 1 mm in diameter. The remaining magnetic field at the center of the chamber is reduced to 10 mG using magnetic shields.

Each chamber is evacuated by a 400 l/s noble ion pump and a titanium getter pump with a separation gate valve and achieves a base pressure of 5×10^{-11} Torr. The apparatus also has a rough-pumping system including a 150 l/s turbo molecular pump, an auxiliary rotary pump and an independent rotary pump. Sample gases are introduced into the analysis chamber, the sample preparation chamber or the sputter ion gun from one of four gas tanks or 20 l gas reservior with a purifier through a variable leak valve. All the operations of the system including the monochromator are controlled by a microcomputer (NEC PO-8801) with GP-IB interface.

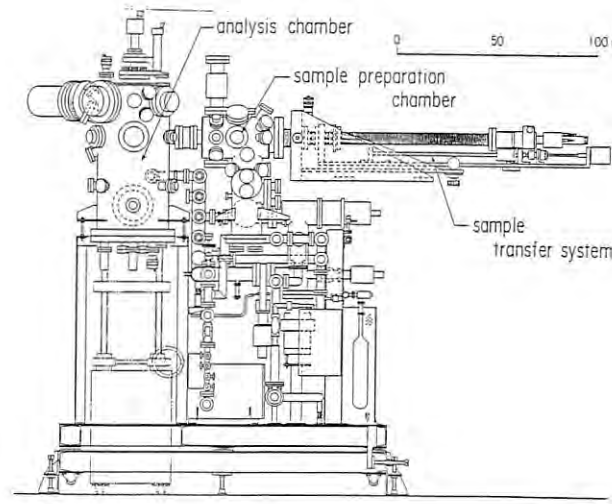

Fig. 5.15

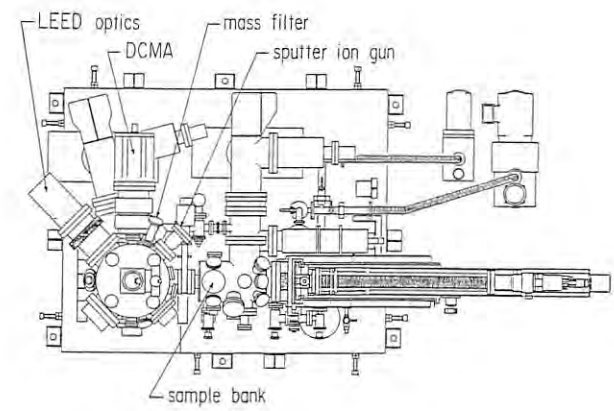

Fig. 5.16

List of Apparatuses

Format
Name of apparatus
1. General characteristics
2. Accessories
3. Other features
4. Typical Experiment
5. Station used
6. Pages in "Activity Report 82/83" describing the details

(a) Multi-purpose chamber for gas phase experiments
1. ultimate pressure 1×10^{-7} Torr.
Equipped with two turn tables notatable the incident light.
2. double-ion chamber.
3.
4. The measurements of absolute photoabsorption cross sections of C_3H_6 and C_4H_8 isomers.
5. BL-12A
6. V-40

(b) Time-of flight spectrometer for photoion measurements
1. Ultimate pressure 5×10^{-8} Torr.
Electrostatic lenses satisfying the conditions of single-field space focusing for threshold electrons and double-field space focusing for ions.
2. Furnace to evaporate alkali-and alkaliearth-metals.
3.
4. The measurements of single-and double-photoionization cross sections of Ca and Sr.
5. BL-12A
6. V-40

(c) Heat-pipe chamber for photoabsorption measurements of free-metal atoms
1. Ultimate pressure 1×10^{-7} Torr.
The pressure difference between vapor colum and differential pumping stage is $\sim 10^7$.
2. Buffer gas inlet system.
3. Heated up to about 1000°C.
4. The measurements of photoabsorption cross sections for 3d electrons of Xe, Cs, and Ba.
5. BL-11A.
6. V-41.

(d) Gas phase angle resolved photoelectron spectrometer
1. Ultimate pressure 5×10^{-8} Torr.
Equipped with a conventional hemispherical electrostatic analyzer and with a position-sensitive parallel-plate electrostatic analyzer.
2. Sample-gas inlet system.
3. A sample gas is confined in a gas cell.
4. The measurements of absolute intensity and polarization of synchrotron radiation from the undulator.
5. BL-2, BL-12A.
6. V-42.

(e) VUV and Soft X-ray Reflectometer
1. Equipped with a goniometer, insuring accurate incidence angle (30 sec)
Up to 89.4° incidence angle
Ease of optical alignment
Ease of sample exchange
High vacuum (2×10^{-9} Torr)
2.
3. Equipped with ports for vacuum evaporation.
4. Optical constants of mirror materials.
Surface roughness.
5. BL-11A
6. V-41. VI-78.

(f) UHV experimental chamber for absorption measurements I.
1. Ultra-high vacuum (1×10^{-10} Torr)
Equipped with an electron-beam gun for evaporation of samples. Equipped with a quartz oscillator capable of being cooled to LNT.
2. Sample holder with an adjustable linear motion, capable of being cooled to LNT.
3. Designed mainly for very reactive metal samples.
4. Absorption measurement of alkali metals, alkali metal alloys, and rare earth metals.
5. BL-11C, BL-11D.
6. VI-82.

(g) UHV experimental chamber for absorption measurements II.
1. High vacuum (1×10^{-9} Torr)
Mounts up to 5 samples.
2. Gas cell (160 mm in length)
Vacuum evaporater
Electron multiplier (R595).
3. 190 mm I.D.
4. Core level absorption in alkali halides and transition metal compounds.
M4,5 giant resonance absorption in Z = 49-57 elements.
Photoefficiency of photocathodes.
Lithography for resist polymer.
5. BL-11A, BL-12C.
6. V-40, VI-73, VI-74, VI-76, VI-77, VI-79.

(h) Vacuum chamber for performance testing of grating monochromator
1. Equipped a 160 mm length gas cell with 10 mm diameter propylene windows.
2. A sample-gas inlet system.
3.
4.
5. BL-11A, BL-12C.
6. V-40.

(i) Focusing Weissenberg camera with multi-layer-linescreens
1. Useful for high resolution macromolecular crystallography.
High signal-noise ratio.
Equipped with multi-layer-line screens.
2. Cooling unit by N_2 gas.
3. Wide range of ψ-axis rotation.
Wide 2θ range.
4. X-ray structure determination of macromolecular crystal (insulin, actin-DNise I complex, Plasminostreptin etc.)
5. BL-4B, BL-4A,
6. VI-5.

(j) X-ray Diffractometer for gasses.
1. Equipped with horizontal ω-2θ two-circle goniometer.
   X-ϕ circle motion available.
2. Gas cell with boiling system.
   Incident beam monitor with scintillation counter.
3. Uses white beam for energy-dispersive method.
   Uses monochromatic beam for angle-dispersive method.
4. Angle-dispersive X-ray diffraction study of carbon dioxide.
5. BL-15C, 14C.
6.

(k) X-ray diffractometer for liquids and melts.
1. Collects intensity-data for radial distribution analysis for non-crystalline materials such as gases, liquids, melts and glasses.
2. θ -2θ goniometer with monochromator and analyzer.
   Single-crystal monochromator with quartz and β-alumina.
   Double crystal monochromator with Si(111).
   Keramax furnace
3.
4. Energy-dispersive study of gas and liquid.
   Angle-dispersive study of liquids, melts and powder crystals.
5. BL-4B.
6. V-24.

(l) Multi anvil high pressure X-ray system.
1. Maximum pressure 13 GPa.
   Maximum temperature 1700°C.
   Sample volume (typical) 2 mmϕ × 3 mmℓ.
   Uses white X-ray.
2. Two axis goniometer
   Handy type SSD.
3. Best quality in the world for this research field.
4. Compressibility of Au at room and high temperatures.
   Time resolved observation of B1-B2 transition of BaS.
5. BL-4C.
6.

(m) EXAFS Spectrometer
1. Dedicated to X-ray absorption spectroscopy.
   High-resolution.
   High-quality beam.
2. Control system with microcomputer (SORD M-223).
   Closed cycle refrigerator.
   Reaction chamber for catalyst.
3.
4. EXAFS of catalysts
5. BL10B.
6. V-8.

(n) Small angle X-ray scattering equipment for solutions (SAXES)
1. Dedicated to small-angle scattering for solutions, synthetic polymers.
2. Stopped flow apparatus.
   Temperature jump apparatus.
   Flash light for specimen.
3. Uses monochromatic beam from the optics installed at BL-10C.
4. Measurements for Bovine Serum Albumin, Lysozyme, Tobacco Mosaic Virus, Purple Membrane etc.
5. BL-10C.
6. V-29.

(o) Ultra-high vacuum X-ray diffractometer
1. Ultra-high vacuum with cryo-pumping system.
   Equipped with X-ray diffractometer and LEED optics.
2. Super precision goniometer using elastic torsion mechanism.
   Microcomputer control system.
   NaI scintillation counter system and SSD.
3.
4. Study on Si(7×7) structure.
5. BL-10C, BL-14B.
6. V-34.

(p) Vertical-type four-circle diffractometer.
1. Used for crystallographic studies and scattering experiments.
   Large X-circle (280 mmϕ).
2. Control system with MELCOM 70/30.
   High-temperature furnace.
   X-rays film cassette.
3.
4. Study on anomalous scattering effect.
5. BL-10A.
6. V-27.

(q) Horizontal-type four circle diffractometer.
1. Specially built, but having a conventional diffractometer configuration.
   Fully computer-controlled for rapid, tunable and precise diffraction data collection.
2. Computer-controlled alignment carriage with 5 stepping motor driven axes, on which the diffractometer is mounted.
   Huber Precession/Rotation camera.
   MELCOM 70/60 minicomputer with OPTRONICS film scanner.
3. Mechanical control interfaced through IEEE-488 bus.
   CAMAC and NIM measuring system.
4. Crystal structure analysis of antibiotics, biotic metabolitos, proteins etc.
5. BL-14A.
6. V-30.

(r) Three-axes X-ray Diffractometer.
1. Equipped with three precision goniometers (Huber 410, 420, and 440).
2. Scintillation counter.
   SSD with MCA.
   Asymmetry cut plane monochrometer.
3. Having precision of 0.36 arc sec per pulse.
4. Phase-contrast microscopy.
   Development of application to medical diagnosis.
5. BL-14C2, BL-15B1.
6. V-32, V1-97, V1-98.

(s) Time-Resolved X-ray measurement system with 1D-PSD.
1. Time resolution up to 1 msec.
   Either 256ch. × 191 frames, 512 ch. × 95 frames, or 1024 ch. × 47 frames.
   Fast data acquisition up to 1 MHz.

2. LSI 11/23 computer.
   CAMAC modules (Time to Digital Converter, Histogramming Memory etc.).
3. Uses monochromatic X-ray (λ=1.5A).
4. Measurements on frog skeletal muscle, purple membrance, Ribosome, etc.
5. BL-15A1, BL-10C.
6. V-35.

(t) X-ray irradiation equipment
1. Assembly of a circular table (Huber 410) with a channel-cut monochromator, slits and irradiation chamber.
2. Ionization chamber for X-ray monitoring.
3. Controls suitable biological atmosphere for samples.
   Wide beam acceptance (4 mmV × 30 mmH).
4. Biological effects of inner shell ionization on bromine-incorporated cells.
5. BL-4C, 15-B1.
6. V1-30, V1-32, V1-33.

(u) High-speed X-ray topography Camera.
1. Equipped with two X-ray TV cameras.
   Maximum load of 30 kg on sample goniometer.
   Facilitates simulataneous observation of two different Laue spots.
2. Microcomputer system (AIDACS-3000).
   Image processor TF4110.
   Work shutter for variable exposure time (0.1∿9.9sec).
3. 1 arc sec accuracy of θ-rotation.
   Ample space around the specimen position.
4. Melting process of GaAs.
   Magnetization process of Fe-3% Si, etc.
5. BL-15B, BL-14C.
6. V-31.

(v) Precision X-ray optics.
1. Goniometer assembly dedicated to precision diffraction study such as double-, triple-, and more than triple-crystal diffractometry and topography.
2. Microcomputer control system.
   NaI scintillation detector system.
   SSD and MCA.
   Ionization chamber for monitoring.
   Room temperature controller.
   Experimental table with air springs
3. 1 arc sec accuracy for full rotation.
   0.1 arc sec accuracy within 6° using tangential bar system.
   Employs super-precision rotation mechanizm with elastic torsion and PZT.
4. Detection of polarization rotation under magnetic diffraction condition.
   Structure analysis of epitaxial layer/substrate interfaces with standing wave method.
5. BL-15C.
6. V-33.

PHOTON FACTORY ACTIVITY REPORT 1983/84

PHOTON FACTORY
ACTIVITY REPORT
1983/84

NATIONAL LABORATORY FOR HIGH ENERGY PHYSICS, KEK